Theses and Dissertations

5-8-2015

Facile Method for Large Scale Alignment of One Dimensional Nanoparticles and Its Biomedical Application

Sheng Feng
University of South Carolina - Columbia

Follow this and additional works at: https://scholarcommons.sc.edu/etd

Part of the Organic Chemistry Commons

Facile Method for Large Scale Alignment of One Dimensional
Nanoparticles And Its Biomedical Application

by

Sheng Feng

Bachelor of Science
Henan Normal University, 2007

Master of Science
Beijing Normal University, 2010

_____

Submitted in Partial Fulfillment of the Requirements

For the Degree of Doctor of Philosophy in

Chemistry

College of Arts and Sciences

University of South Carolina

2015

Accepted by:

Qian Wang, Major Professor

John H. Dawson, Committee Member

Caryn E. Outten, Committee Member

Hexin Chen, Committee Member

Lacy Ford, Vice Provost and Dean of Graduate Studies

DEDICATION

This dissertation is dedicated to my lovely supportive wife, Yuhui, my cute smart

daughter, Alice, and my parents who always treat me as their priority.

ACKNOWLEDGEMENTS

I sincerely acknowledge the following individual. I could never finish this dissertation without all the helps and efforts they have offered.

First of all, I am deeply grateful to my mentor, Dr. Qian Wang. I have learned so much from him. His diligent work driven by his curiosity towards the unknown intrigues me to pursue the career of science. He is also such an excellent teacher that he always uses analogies from daily life to explain academic phenomena. Besides this, he is also my teacher about social interaction. He has set an example for not only my scientific career, but also personal life.

Secondly, I would like to express my acknowledgement to the following professors, colleagues, and former lab members who have given me so many helps and mentorship: Associate Professor Hexin Chen, Associate Professor Caryn E. Outten, Professor John H. Dawson, Associate Professor Chuanbing Tang, Assistant Professor Hui Wang, Associate Professor Ming Xian, Associate Professor Xinfeng Liu, Associate Professor John J. Lavigne, Dr. Xingjie Zan, Dr. Gary Horvath, Dr. Xinrui Duan, Dr. Elisabeth Balizan, Dr. Jittima Amie Luckanagul, Dr. Nikki Sitasuwan, Dr. Dan Manesco, Nick Mank, and Lin Lu.

Lastly, I want to thank my family: my wife and my parents for their love and unconditional support, my mother in law for her taking care of her granddaughter in her parents' absence, my little Alice for your support with your laughter and love.

ABSTRACT

Topographical cues can profoundly affect cellular behaviors. This thesis investigate how to utilize the topographical cues generated by two techniques, flow assembly and electrospinning, to regulate cellular behaviors.

First of all, a facile and robust method to align one-dimensional (1D) nanoparticles (NPs) in large scale has been developed. Using flow assembly, representative rod-like nanoparticles, including tobacco mosaic virus (TMV), gold nanorods and bacteriophage M13, have been aligned inside capillaries by controlling flow rate and substrate surface properties. The properties of 1D NPs, such as stiffness and aspect ratio, play a critical role in the alignment. Furthermore, these hierarchically organized structures can be used to support cell growth, where cell orientation and morphology are controlled. When C2C12 myoblasts were cultured on surfaces coated with aligned TMV, we found that nanoscale topographic features were critical to guide the cell orientation and myogenic differentiation. This method can be used in the fabrication of complex assemblies with 1D NPs and has wide applications in tissue engineering, sensing, electronics and optical fields.

Furthermore, we combined this flow assembly method with genetically modified TMV mutants with reported cell adhesion sequences (i.e. RGD1, RGD7, PSHRN3, P15, and DEGA) to generate biomimetic substrates with specific cell adhesion motifs and precisely controlled structural organization for guiding cell behaviors by providing desired biochemical and physical cues. We found that TMV mutants significantly promote neurite

outgrowth and the resultant aligned TMV mutants substrates were able to dictate directional neurite outgrowth of N2a cells. Hence, the plant virus-based materials provide tremendous promise for neural tissue engineering in the future.

In addition, we generated the electrospun polycaprolactone (PCL) microfibers for three dimensional (3D) culture of breast cancer cell lines, MCF-7. We found that cancer stem cells (CSCs), a small group of tumor-initiating cells within tumors as the main contributors of tumor growth, metastasis, and recurrence, have significantly increased the proportion in the whole population. The expression of stem cell markers, including OCT3/4 and SOX2, and breast CSC-specific markers, SOX4 and CD49f, was significantly upregulated, and the mammosphere-forming capability in cells cultured in 3D PCL scaffolds increased. The fibrous scaffolds also induced the elongation of MCF-7 cells and extended cell proliferation. The increase of CSC properties after culturing in 3D scaffolds was further confirmed in the other two luminal-type mammary cell lines, T47D and SK-BR-3, and a basal-type cell line, MDA-MB-231. Moreover, we observed the upregulation of epithelial to mesenchymal transition and increased invasive capability in cells cultured in 3D PCL scaffolds. These data suggests that the increase of CSC proportion in 3D culture system may account for the enhanced malignancy. Therefore, our 3D PCL scaffolds can potentially be used for CSCs enrichment and anti-cancer drug screening.

Finally, by electrospinning of polycaprolactone solutions containing N-(benzoylthio)benzamide (NSHD1), a H_2S donor, we fabricated fibrous scaffolds with hydrogen sulfide (H_2S) releasing capability (H_2S-fibers). The resultant microfibers are capable of releasing H_2S upon immersion in aqueous solution containing biological thiols under physiological conditions. The H_2S release peaks of H_2S-fibers appeared at 2~4 hours,

vi

while the peak of donor alone showed at 45 minutes. H_2S release half-lives of H_2S-fibers were 10-20 times longer than that of donor alone. Furthermore, H_2S-fibers can protect cells from H_2O_2 induced oxidative damage by significantly decreasing the production of intracellular reactive oxygen species (ROS). Given that H_2S has a broad range of physiological functions, H_2S-fibers hold great potential for various biomedical applications.

In summary, the emerging area of nanotechnology have been applied for biomedical application as well as the fundamental study of the interaction between cell behaviors and surrounding nanomaterials. Here, we have generated a robust and facile method that can align various 1D NPs in a large quantity. The resulting substrates in capillaries can be used to guide the directionality of cell growth. Meanwhile, we investigated the effects of electrospun microfibers on breast cancer stem cells and fabricated H_2S releasing fibers, which could be used in tissue engineering.

TABLE OF CONTENTS

LIST OF TABLES

LIST OF FIGURES

xiii

CHAPTER 1

FACILE METHOD FOR LARGE SCALE ALIGNMENT OF ONE DIMENSIONAL NANOPARTICLES AND CONTROL OVER MYOTUBES ORIENTATION

Portions of this chapter appear in the following manuscript: facile method for large scale alignment of one dimensional nanoparticles and control over myotubes orientation.[1]

1.1 INTRODUCTION

One-dimensional (1D) nanoparticles (NPs), such as nanorods, and nanotubes, have become attractive building blocks for modern materials with wide applications in tissue engineering,[2] medicine,[3] electronics,[4] and optical devices.[5] Due to their unique anisotropic shapes and shape related properties of 1D NPs, the orientation and alignment of 1D NPs is crucial for final material properties.[6-7] For example, it has been shown that both electrical and thermal conductivity of carbon nanotubes increases along the alignment direction; and the enhancement was strongly dependent on the degree of alignment.[8-9] Therefore, controlling 1D NPs orientation is an important topic during the development of 1D NPs materials.

A variety of methods have been proposed for integrating organized 1D NPs into devices. One group of methods is based on the interaction between 1D NPs and supporting substrates, where the orientation of 1D NPs is directed by surface chemical functionalities,[10] micropatterns fabricated by lithography,[11] or the capillary force at a contact line during a drying process.[12] Another strategy to direct the orientation of 1D NPs

1

is to employ an external force. This external force can be a contact shear force,[13-15] electric field,[16] fluid flow,[4, 17-18] or surface pressure.[19] For example, using shear force generated by fluid flow, Lieber and coworkers have demonstrated that indium phosphide, gallium phosphide, and silicon nanowires were aligned by flowing nanowire suspensions through polydimethylsiloxane templated microchannels.[17] Inspired by the simple physics behind this fluid flow method, we seek to expand it beyond the original microchannel setup, and develop a cost-effective, time-saving, high-throughput and generally applied method to control 1D NPs orientation in large scale.

Many cells or tissues with the aligned organization *in vivo* include neural cells[20] corneal tissue,[21] vascular tissue,[22] musculoskeletal tissue[23] and myocardial tissue.[24] Directing cell orientation and differentiation is critical for tissue engineering in term of mimicking the real tissue, in most of which the cell are directed by orientated extracellular matrix (ECM) proteins.[25,26] Taking advantage of 1D NPs to direct cell growth and differentiation has been demonstrated by Werner, where aligned 1D collagen fiber enhanced myotube organization and length, and modulated the growth and fate of mesenchymal stem cells.[27] In our previously studies, aligned bacteriophage M13 thin film was utilized to guide cell oriented along the M13 aligned direction through directing the secreted ECM protein.[27,28] In addition, the confined spaces, perpendicularly to the capillary, provided by tobacco mosaic virus (TMV) patterned rings were used to direct the perpendicular orientation of smooth muscle cells to the capillary, which is believed to have great potential to develop a vascular grafting.[28]

In this study, a facile and robust method to align one-dimensional (1D) nanoparticles (NPs) in large scale has been developed. Using flow assembly, representative

rod-like nanoparticles, including TMV, gold nanorods and bacteriophage M13, have been aligned inside glass tubes by controlling flow rate and substrate surface properties (Figure 1.1a). TMV has the shape of a hollow cylinder (18 nm in diameter, 300 nm in length, and 4 nm cavity), consists of 2,130 identical subunits that assemble helically around single strand RNA (Figure 1.1b and 1.1c) and can be modified chemically and genetically.[30,31] The uniformly ordered nanostructure and well-defined geometry of TMV provides a unique building block for nanomaterial development and biomedical applications.[29-40] Therefore, TMV was chosen to optimize the experimental setup and assembly conditions. When C2C12 myoblasts were cultured on surfaces coated with aligned TMV, we found that nanoscale topographic features were critical to guide the cell orientation and myogenic differentiation. This method can be used to fabricate complex structures with 1D nanoparticles and will have wide applications in tissue engineering, sensing, electronics and optical fields.

1.2 RESULTS AND DISCUSSION

1.2.1 Setup of the Flow Assembly for the Alignment of 1D NPs

The setup of the experiment is schematically illustrated in Figure 1.1a, which is consisted of a glass capillary tube (inner diameter ~0.16 cm, length ~15 cm), a solution feeder tube (plastic tubing with inner diameter ~0.15 cm) and high pressure gas cylinder with a valve to control gas and subsequent fluid flow rate. One end of the plastic feeder tube is connected to the glass capillary tube, and the other end is left open for filling 1D NPs solution, and subsequent connection to a high pressure cylinder. All connection areas are sealed to avoid the leaking of solution or gas. In this case, the NP solution is driven through the glass capillary by the high pressure gas once the cylinder valve is open.

3
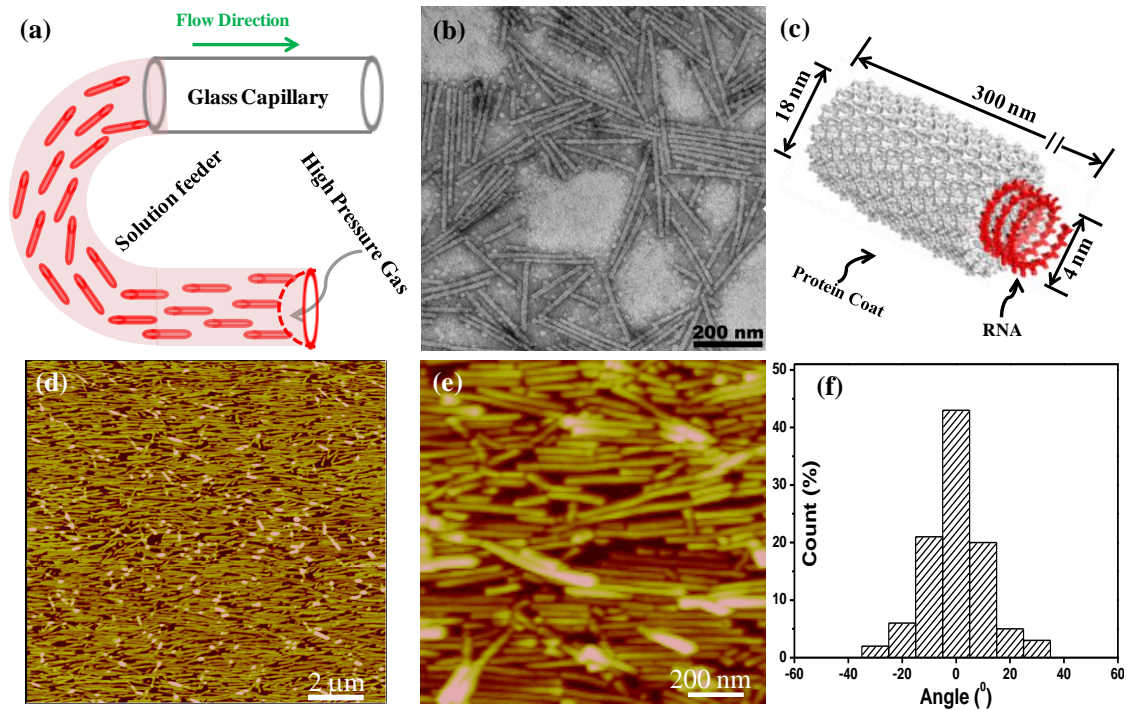
Figure 1.1. Schematic illustration of flow assembly. (a) Schematic illustration of experimental setup. One end of feeder tube is connected to the capillary while the other end is kept open for filling of 1D NPs solutions and subsequent high pressure gas. 1D NPs solution is only filled into the plastic tube, keeping the glass capillary tube empty. Then the solution in the feeding tube is driven through the capillary tube by the high pressure gas. After the NPs solution flows through the capillary tube, the capillary is dried by a continuing gas flow. The arrow "→" indicates flow direction. (b) Transmission election microscopy (TEM) image and (c) structure illustration of TMV. (d) AFM image of aligned TMV on the inner surface of a capillary tube after the flow assembly, prepared with a TMV concentration of 0.05 mg mL^{-1} and a flow rate of 200cm s^{-1}. (e) Magnified image of (d). (f) A histogram of TMV angular spread distribution with respect to flow direction.[1]

Before the fluid flow, the capillaries were immersed in chitosan solution (1 mg mL^{-1} in 0.1% acetic acid at pH 6.5) for 20 mins, and then dried by the N$_2$ flow. In a typical experiment, 10 mL TMV (0.05 mg mL^{-1}) was filled into a plastic feeder tube and driven through a capillary by a fluid flow rate of 200 cm s^{-1}, then dried completely with air flow. TMV particles were distributed evenly with 96% surface coverage and an overall alignment along the long axis of the capillary, as shown under AFM (Figure 1.1d and 1.1e). More importantly, such alignment was observed on over 20 random positions in the inner

www.manaraa.com

surface of the glass tube, indicating a uniform coverage over the whole capillary tube. The orientation of TMV was further quantitatively assessed by analyzing angles of more than 200 nanorods with respect to flow direction. The angular spread distribution histogram of TMV is shown in Figure 1.1f. Over 84% TMV nanorods were aligned within $\pm 10°$, and the rest were distributed between $\pm 10-30°$. In addition, with this method, we also generated the aligned TMV in the polycaprolactone (PCL) tubes (Figure 1.2), which is a widely used material for tissue engineering. The coverage of TMV is lower in PCL tubes than glass capillary tubes at the same prepared conditions, likely due to the difference of the surface chemistry between PCL tubes and glass capillary tubes, which will be further discussed in the next section.

1.2.2 Effects of Surface Properties on the TMV Alignment

In order to understand the origin of the aligned structure and key factors on controlling the alignment, various control experiments were carried out. All samples and their corresponding preparing conditions were listed in Table 1.1. All samples were prepared under same TMV concentration (0.02 mg mL^{-1}) and flow rate (200 cm s^{-1}). After the samples were ready, at least 20 AFM images were taken for each sample from the random position of capillary tubes. Based on the AFM images, TMV angular spread distribution histograms were obtained by analyzing the angles of more than 200 particles with respect to the flow direction, then the histograms were simulated by Gaussian equation. The alignment degrees of 1D NPs were also evaluated by the half-height peak width (HPW), *i.e.* the peak width at the half-height of peak. The smaller the HPW number is, the better alignment the sample has.[17] The surface coverage was used to estimate the coating efficacy of this method. The results are listed in Table 1.1. In the Control 1, the

5

experiment was performed under the described condition, but no fluid flow was applied. Only randomly distributed TMV (Figure 1.3a) with 44% surface coverage was observed. The value of HPW is 176°, which is very close to the totally random distribution of 180°. This result indicates that such aligned TMV nanorods structure was generated by the shearing force from the solution flow.
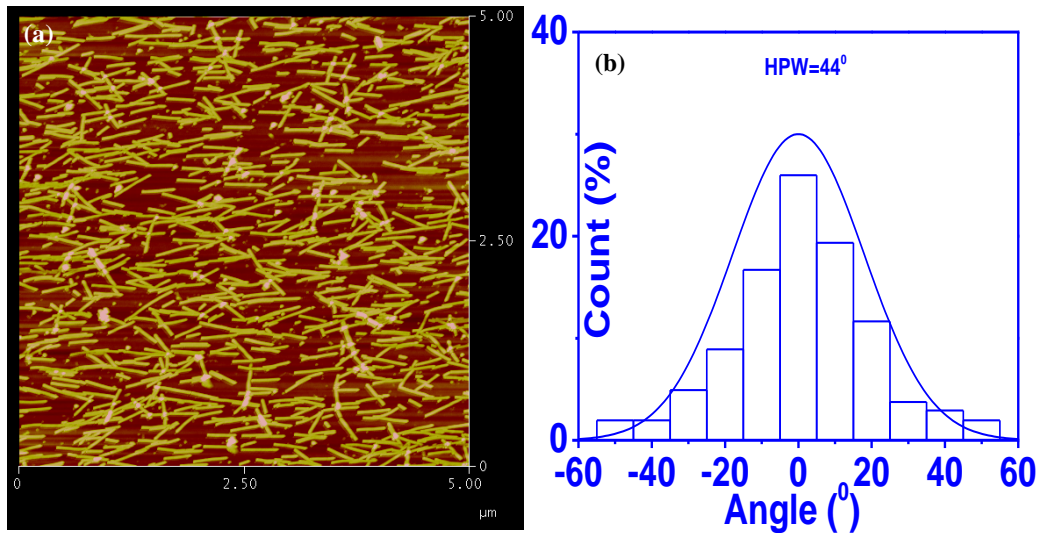
Figure 1.2. AFM image of aligned TMV on the inner surface of commercial PCL tube after flow assembly, prepared with a TMV concentration of 0.02 mg mL^{-1} and flow rate at 200cm s^{-1}. In brief, PCL tube with inner diameter ~1.8 mm was purchased from Cole-Parmer Company and was cut into 10 cm in length. Before fluid flow, the tube was treated by immersing in 2 mg mL^{-1} polyallyamine hydrochloride (PAH) solution (pH = 11.0) overnight for aminolysis, and then washed by copious hydrogen chloride solution (pH = 2) for 2 mins. Then (PSS/PAH)$_2$ was coated on inner surface of PCL tube by following procedure: alternatively immersing capillaries in PSS (1 mg mL^{-1}) for 20 min and PAH solution (1.0 mg mL^{-1} pH=5.0) for 20 min. Water was used to rinse in between each deposition step until the desired number of layers was obtained. The (PSS/PAH)$_2$ coated tubes was used for the fluid flow assembly.[1]

The interaction between TMV and the substrate plays an important role on forming this oriented structure. This interaction depends on two major factors: the surface energy and the surface charge distribution. Because the pI of TMV is around 3.4,[41] in our general protocol, chitosan was used to give the capillary a positively charged internal surface. The

6

water contact angle of chitosan coated surface was 48 ±2°. In Control 2 and 3, two other cationic compounds, poly(diallyldimethylammonium chloride) (PDDA) and (3-aminopropyl)triethoxysilane (APTES), were used to obtain similar positively charged surface, but different surface energy. Simply judged from the water contact angles, Control 2 has higher while Control 3 has lower surface energy than chitosan modified surface (water contact angles were 30 ±1° and 81 ±2°, respectively). After the fluid flow, similar assembly morphologies were obtained (Figure 1.3b) for both cases. Their comparable HPW and surface coverage percent values with the typical sample (Table 1.1) indicate the surface energy was not a key factor on controlling the alignment. On the other hand, if the surface was negatively charged or neutral, as shown in Control 4-6, the high HPW were generated (Table 1.1), suggesting TMV particles were randomly distributed (Figure 1.3c). In addition, the surface coverage of Control 4-6 are much lower than the Control 2-3 and typical chitosan modified samples (Table 1.1) due to electrostatic repulsion between TMV and the substrate. These results revealed that the electrostatic interaction between TMV and the substrate is critical for the formation of the aligned structure. To confirm this hypothesis, we increased the ionic strength of the TMV solution by adding 50 mM phosphate buffer (pH 7.0) to weaken the electrostatic attraction between TMV and chitosan coated surface (Control 7). As our expectation, weakening attraction resulted in increased HPW and decreased surface coverage (Table 1.1 and Figure 1.3d), indicating much less TMV particles deposited and a worse alignment. Overall, the shearing force generated by fluid flow can drag TMV particles to align along the flow direction, *i.e.* the long axis of capillary tube, due to its anisotropic shape. The attractive force between TMV and capillary internal surface plays an important role in pinning the TMV particles on the surface.

7

Finally, we found that, once it was dried by following gas immediately, the deposited TMV with aligned structure was almost no change on the HPW and slight decrease in surface coverage after it was immersed into PBS solution at 37 °C for 24h (Figure 1.3f). This feature suggests that it is a relatively stable environment for the cell study. However, TMV particles could be washed off if the sample was not dried completely by the gas glow (Figure 1.3e), which gave a decreased surface coverage and a similar HPW (Control 8 in Table 1.1).
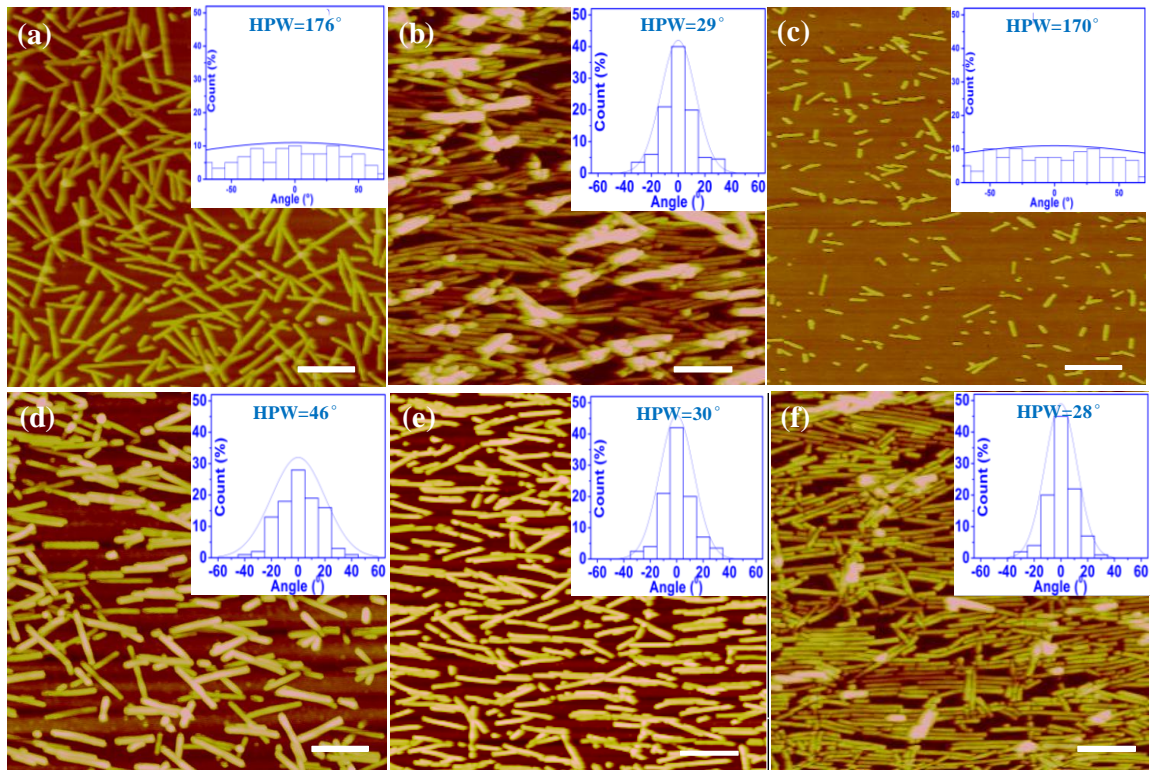
Figure 1.3. Charge-charge interaction affects flow assembly. AFM images of (a) Control 1; (b) Control 2 (Control 3 gave similar results); (c) Control 4-6; (d) Control 7; (e) Control 8; and (f) The typical sample after immersed into PBS for overnight at 37 °C. All scale bars indicate 200 nm. The insets are the histograms of TMV angular distribution at corresponding flow rates. The curve in each histogram is fitted by Gaussian equation based on the histogram data. The angle distribution histograms were obtained by statistical analysis of angular distribution of about 200 TMV particles with respect to the flow direction.[1]

1.2.3 Effect of Flow Rate on TMV Alignment

For testing the effect of flow shearing force on the alignment of TMV, different flow rates ranging from 50 to 200 cm s^{-1} were applied to prepare samples with fixed TMV concentration at 0.02 mg mL^{-1}. Based on the AFM images (Figure 1.4a-d), TMV angular spread distribution histograms were obtained by analyzing the angles of more than 200 particles with respect to the flow direction, then the histograms were simulated by Gaussian equation (insets of Figure 1.4a-d). Obviously, with the increased flow rate, the width of TMV angular distribution was narrowed, while the distribution near angle 0 ° in the histograms increased. To evaluate the alignment degree of 1D NPs, the HPW was plotted against flow rate and shown in Figure 1.4e. The HPW decreased from 52 ° to 28 ° with the increased flow rate from 50 cm s^{-1} to 200 cm s^{-1}. It implies that the alignment of TMV was improved greatly by increasing the flow rate, which is consistent with the previous report.[17] This phenomenon can be explained from the Newton shear flow theory: the shearing force increases proportionally with the flow rate. Because the TMV particles are aligned in response to the shearing force, a higher flow rate means a bigger shearing force, hence leads to a better alignment. The best alignment in the experimental flow range for this system is that about 84% TMV nanorods were aligned within ±10 ° at flow rate 200 cm s^{-1}. Thus the flow rate of 200 cm s^{-1} was used for next samples preparation if it was not mentioned specially. In all tested flow rate range, samples exhibited constant surface coverage around 85%, as shown in Figure 1.4e. For testing the effect of flow shearing force on the alignment of TMV, different flow rates ranging from 50 to 200 cm s^{-1} were applied to prepare samples with fixed TMV concentration at 0.02 mg mL^{-1}. Based on the AFM images (Figure 1.4a-d), TMV angular spread distribution histograms were obtained

9

by analyzing the angles of more than 200 particles with respect to the flow direction, then the histograms were simulated by Gaussian equation (insets of Figure 1.4a-d). Obviously, with the increased flow rate, the width of TMV angular distribution was narrowed, while the distribution near angle 0 °in the histograms increased. To evaluate the alignment degree of 1D NPs, the HPW was plotted against flow rate and shown in Figure 1.4e. The HPW

Figure 1.4. AFM images of flow assembly TMV on chitosan modified capillary tube at different flow rates: (a) 50 cm s^{-1}; (b) 100 cm s^{-1}; (c) 150 cm s^{-1}; and (d) 175 cm s^{-1}. The TMV concentrations were 0.02 mg mL^{-1}. The insets are the histograms of TMV angular distribution at corresponding flow rates. The curve in each histogram was fitted by Gaussian equation based on the histogram data. The angle distribution histograms were obtained by statistical analysis of angular distribution of about 200 TMV particles with respect to the flow direction. (e) The dependence of HPW direction on flow rate. All scale bars indicate 200 nm.[1]

decreased from 52 ° to 28 °with the increased flow rate from 50 cm s^{-1} to 200 cm s^{-1}. It implies that the alignment of TMV was improved greatly by increasing the flow rate, which

10

is consistent with the previous report.[16] This phenomenon can be explained from the Newton shear flow theory: the shearing force increases proportionally with the flow rate. Because the TMV particles are aligned in response to the shearing force, a higher flow rate means a bigger shearing force, hence leads to a better alignment. The best alignment in the experimental flow range for this system is that about 84% TMV nanorods were aligned within $\pm 10°$ at flow rate 200 cm s^{-1}. Thus the flow rate of 200 cm s^{-1} was used for next samples preparation if it was not mentioned specially. In all tested flow rate range, samples exhibited constant surface coverage around 85%, as shown in Figure 1.4e.

1.2.4 Influence of TMV Concentration on Alignment and Substrate Coverage

The surface coverage of the TMV can be controlled by the TMV concentration. As shown in Figure 1.5a-c, the average coverage are about 95%, 86% and 50% for the TMV concentration at 0.05, 0.02 and 0.005 mg mL^{-1} respectively. In addition, the decreased concentration also led to the slightly decreased alignment, as revealed by the HPW of the simulated peaks (insets of Figure 1.5a-c). These results are consistent with previous report.[42] The differences in coverage in micro-scale as well as the alignment are important for controlling cell orientation and differentiation, which will be further discussed in the following cell study section.

1.2.5 Influence of 1D NPs Physical Properties on the Alignment

We extended our method to other 1D NPs and showed how the physical properties affect the fluid flow assembly. A selection of different kinds of representative 1D NPs were studied, including potato virus X (PVX),[43] TMV-Aniline hybridized fibers,[41] filamentous bacteriophage M13,[44] and gold nanorods (GNRs).[45] The selection of these 1D NPs is due to not only their representatives in their respective family, but also their distinctive physical

properties (aspect rations and rigidity). The preparation and purification of the selected 1D

NPs were described in detailed in the Experimental Section. The physical properties of

these 1D NPs are listed in Table 1.2 and TEM images are shown in Figure 1.6a-d.
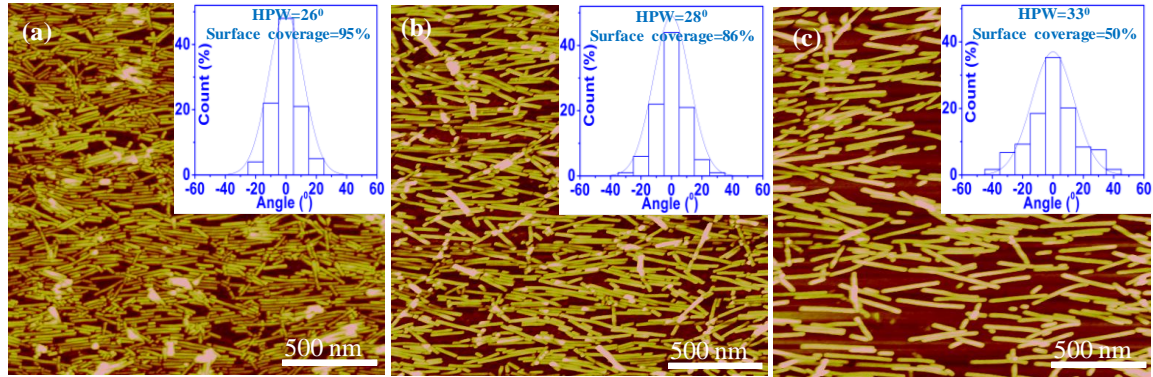
Figure 1.5. AFM images of flow assembly with different concentrations of TMV on chitosan modified capillary tubes at a fixed flow rate of 200 cm s^{-1}: (a) 0.05 mg mL^{-1}; (b) 0.02 mg mL^{-1}; and (c) 0.005 mg mL^{-1}. The insets are their corresponding angular spread distribution histograms of TMV with respect to the flow direction and HPW values.[1]

We fixed the flow rate at 200 cm s^{-1} and the 1D NPs concentration at 0.02 mg mL^{-1}

during the flow assembly process and the final results were observed by AFM (Figure 1.6e-

h). The particle alignment with respect to the fluid flow direction was analyzed, and

corresponding angular spread distribution histograms were obtained as shown in the insets

of the Figure 1.6e-h. The alignment degree was evaluated by the HPW, as plotted in Figure

1.6e. All of these 1D NPs showed the aligned orientation but with different degree. We

hypothesize that rigidity and aspect ratio of 1D NPs are two major factors on the alignment,

and 1D NPs with higher aspect ratio and higher rigidity can lead to a better alignment.

To study how the rigidity and aspect ratio affect the alignment, we set those 1D

NPs into several pairs for comparison, based on comparable rigidity or aspect ratio. The

role of rigidity on the alignment was illustrated by comparing alignment degrees of two 1D

NPs with similar aspect ratio, but different modulus, *i.e.* GNRs and TMV. The HPW of

12

GNRs (14 °) is much narrower angular spread than TMV (28 °) because of the 45-fold higher modulus of GNRs (Figure 1.6h *versus* Figure 1.1d), suggesting the higher rigidity of 1D NPs result in the better alignment. The dependence of alignment on the aspect ratio of 1D NPs could be reflected when compared two 1D NPs with similar modulus, but different aspect ratio, *e.g.* TMV *vs.* TMV-Aniline fiber. The HPW of TMV-Aniline fiber had been narrowed to 16 ° from 28 ° with the increased length from 300 nm to 4 μm (Figure 1.6f *versus* Figure 1.1d). Similarly, PVX, a little bit longer than TMV but with comparable rigidity, showed a slightly better alignment degree (25 ° in HPW) than TMV (28 ° in HPW) (Figure 1.6e *versus* Figure 1.1d). Furthermore, under comparable modulus, TMV, PVX and TMV-Aniline fiber having gradually increased aspect ratio displayed the gradual decrease in HPW. All of these results indicate higher aspect ratio of 1D NPs leads to a higher alignment degree. Compared the HPW of TMV-Aniline fiber (16 °) to M13 (44 °), much bigger difference between TMV-Aniline fiber and M13 than other pairs of 1D bio-NPs was observed due to the synergetic enhancement from longer length and higher modulus of TMV-Aniline fiber than M13 (Figure 1.6f *versus* Figure 1.6g). The surface coverage is over 90% for all tested samples except the GNRs with 34% surface coverage (Figure 1.6). The low coverage of the GNRs might be caused by its surface chemistry defects.[46]

Finally, all tested 1D NPs had formed the aligned orientation. Among these 1D NPs, TMV-Aniline fiber and GNRs have higher rigidities (Table 2.2), thus resulting in the best alignment, *i.e.* 95% particles aligned within $\pm 10^o$ and 98% aligned within $\pm 10^o$, respectively, which may have potentials in the electronic and optic applications.[47-48] The rigidity and aspect ratio of the 1D NPs are two major factors on the alignment of the 1D

13

NPs, which should be considered when this method is applied. The same method might be used to control the alignment of other 1D NPs if optimized fluid flow and suitable attraction between 1D NPs and substrate were applied
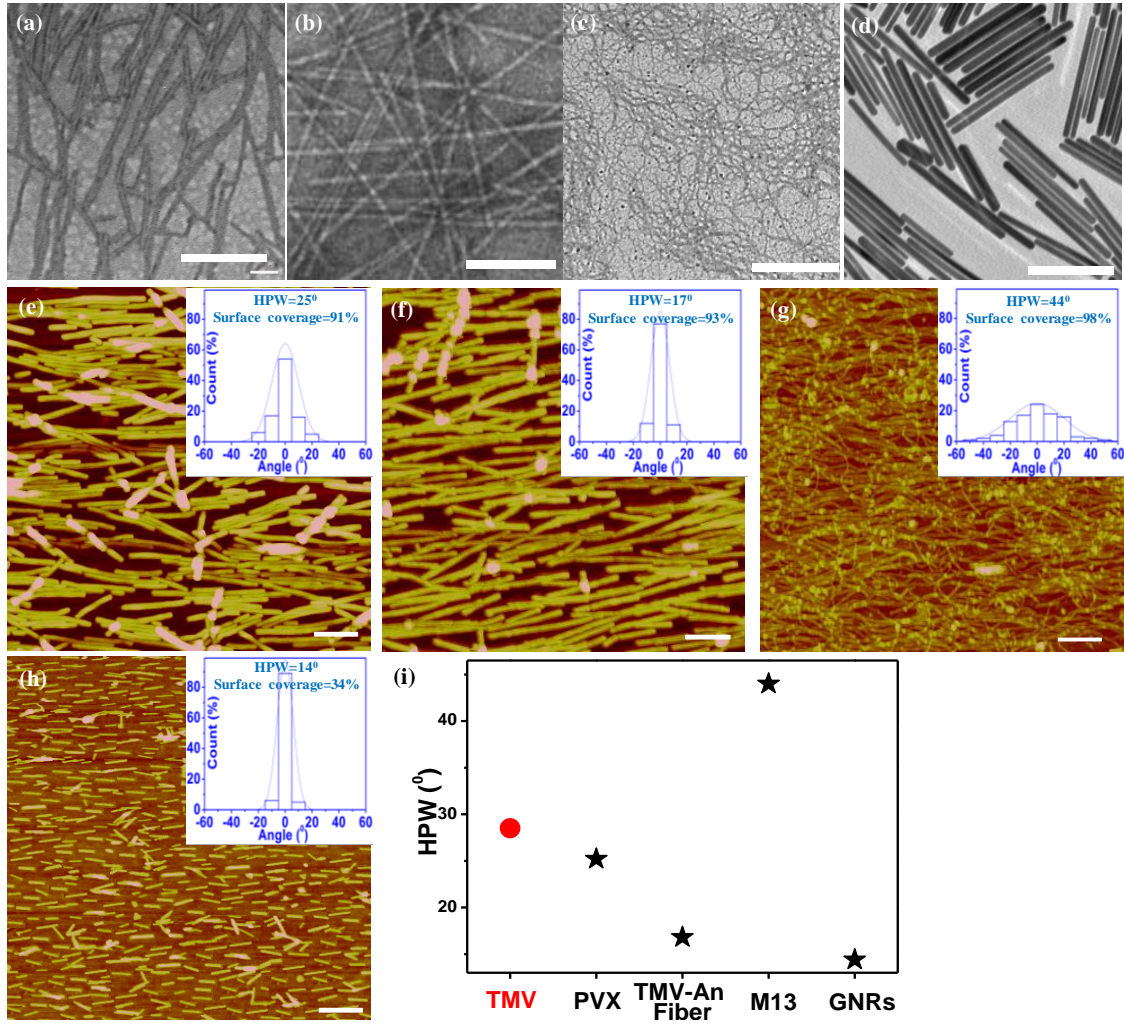
Figure 1.6. Flow assembly of other 1D NPs. (a-d) are the TEM images of (a) PVX; (b) TMV-Aniline fiber; (c) M13; and (d) gold nanorods (GNRs). (e-h) are the AFM images of inner wall of capillary after flow assembly with (e) PVX; (f) TMV-Aniline fiber; (g) M13; and (h) GNRs, with fixed flow rate of 200 cm s^{-1} and the concentration of 0.02 mg mL^{-1} of NPs. The capillary was modified by (PDDA/PAA)$_3$ for (h), others are modified by chitosan. The insets in (e-h) are their corresponding angular spread distribution histograms with respect to the flow direction. Each histogram was obtained by statistical analysis of angular distribution of about 200 nanorods. (i) The HPW plot of different 1D NPs. The scale bars indicate 400 nm for all TEM images (a-d), 200 nm for (e), 500 nm for (f) and (g), and 1 μm for (h).[1]

14

1.2.6 Alignment and Differentiation of Myotubes

Enhancing the differentiation and alignment of cells in biomaterials is crucial for engineering functional tissues with anisotropic properties.[49] For example, in native musculoskeletal tissue, the myoblasts form aligned fibers in a highly organized manner through the fusion into the multi-nucleated myotubes.[23] The similar organization with the alignment also exists in myocardial tissue.[24] This aligned arrangement is indispensable for tissues to generate the contractile force. Using the aligned topographical features created by flow assembly, we studied the orientation and differentiation of C2C12 myoblasts guided by the contact cues.

Skeletal myogenesis, as a terminal differentiation process, is involved in the differentiation and fusion of proliferating mono-nucleated myoblasts into multi-nucleated myoblasts. C2C12 myoblasts have been used as a model system to study various types of muscular dystrophies *in vitro*.[50-52] Many studies have described the patterning of C2C12 cells on different modified surfaces. For instance, micro-contact printing has been used to generate fibronectin islands with different geometric cues to study the C2C12 cells alignment and maximize the differentiation.[53] Previous study revealed a 2D substrate coated with TMV or TMV mutants promotes rat bone marrow stromal cells osteogenic differentiation.[54] However, how the aligned TMV surfaces affect the alignment and differentiation of C2C12 cells is still unknown. Four kinds of aligned TMV and TMV-RGD-coated capillaries, TMVH, TMVL, RGDH and RGDL, were prepared for cell studies. The letter H denotes high coverage (starting with 0.02 mg mL^{-1} of TMV or TMV-RGD), while L denotes low coverage (starting with 0.005 mg mL^{-1} of TMV or TMV-RGD) of TMV or TMV-RGD assembled on chitosan modified capillary tubes at a fixed flow rate of

15

200 cm s^{-1}, and random arranged TMV coated capillary tubes were used as the control. TMV-RGD here is the mutant TMV with inserted sequence GRGDSPG, and had been proved to enhance cell attachment and stimulate osteogenic differentiation.[30, 55]

We first seeded C2C12 myoblasts in capillary tubes with different TMV alignments and allowed cells to attach overnight. We did not observe any significant difference in the cells attachment to substrates among different groups. After 3 day proliferation, cells were subjected to differentiation medium (DM). Figure 1.7a shows the fluorescence images of the cells with myosin heavy chain (MHC) (red) and DAPI (blue) staining on different substrates after 7 days cultured in DM (representative images with low magnification are shown in Figure 1.8). The appearance of MHC staining indicated the formation of the myotubes in all groups.

In order to quantify the degree of the myotube alignment, using ImageJ software, we measured the angles of myotubes with respect to the flow direction in 15 low magnification fluorescence images in each group and plotted the angular distribution histograms (Figure 1.7a). The TMVH showed the best alignment with HPW 34°; and the RGDH and RGDL showed the moderate alignment. RGDH (HPW 46°) was a little higher than RGDL (HPW 48°); and the TMVL displayed seldom alignment (HPW 126°), while there was no alignment (HPW 180°) in the random TMV coated sample. Within the deviation of $\pm 20^{\circ}$, about 93% of myotubes were aligned for TMVH, and this number decreased to 81%, 75%, and 49% for RGDH, RGDL and TMVL, respectively. The low degree of the alignment in TMVL might be due to the low density of TMV is insufficient to guide the C2C12 cells. However, the RGDL provides the strong binding motifs, RGD

peptides, to C2C12 cells. By displaying the cell binding motifs, the low density of TMV-RGD was still able to generate moderate guidance for the alignment of cells.
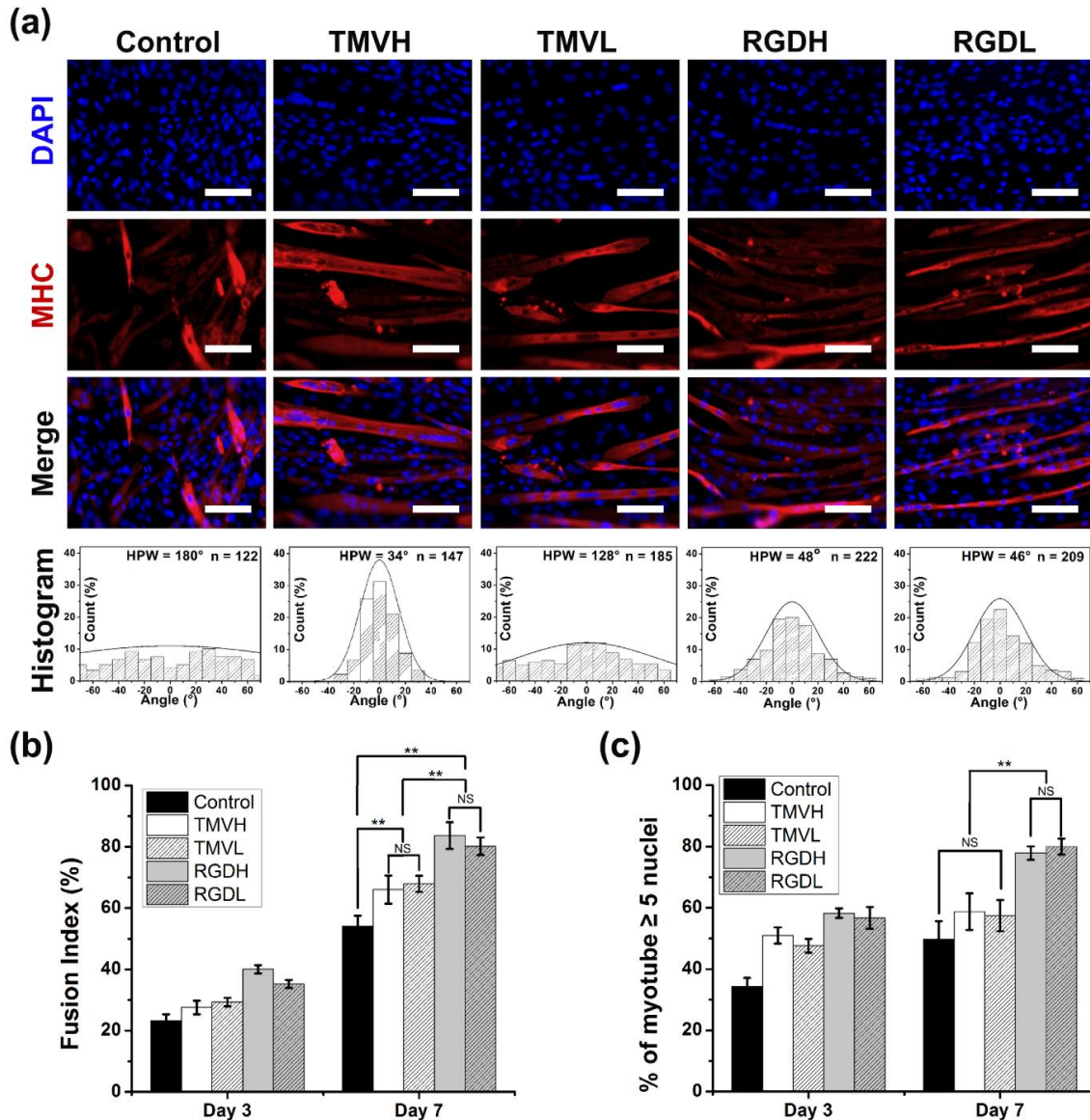
Figure 1.7. Alignment and differentiation of myotubes. (a) Fluorescent images of the C2C12 cells with the induction of differentiation for 7 days on the tubes with different NPs. Cells were stained for anti-MHC (red) and DAPI (blue). All scale bars indicate 100 μm. The bottom rows are corresponding histograms of the angular distribution of myotubes. (b) Quantification of the fusion index (b) and maturation index (c) for C2C12 cells in the tubes with different NPs. They were calculated as the ratio of nuclei number in myocytes with 2 or more nuclei over the total nuclei number and the percentage of myocyte with 5 or more nuclei, respectively. Significance: ** $p < 0.01$ and NS = not significant.[1]

17
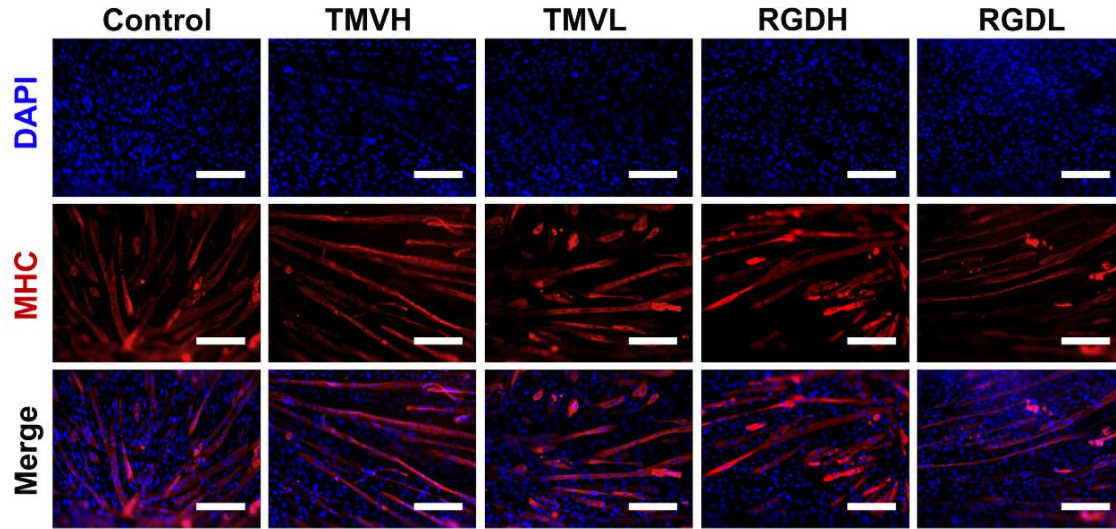
Figure 1.8. Fluorescent images of the C2C12 cells with the induction of differentiation for 7 days on the tubes with different NPs. Cells were stained for anti-MHC (red) and DAPI (blue). All scale bars indicate 200 μm.[1]

To quantify the differentiation of myoblasts, we calculated the fusion index and maturation index from the immunofluorescence images by determining the number of nuclei from multinucleated myocytes over the number of total nuclei in that field and the percentage of myotubes with 5 or more nuclei, respectively.[56] Two independent experiments were performed and 6 randomly images were used to determine the fusion index and maturation index for each group. The results show that the fusion indices for cells in TMVH and TMVL groups (66.1 ± 4.6% and 67.9 ± 2.6%, respectively) significantly increased compared to the control group (54.1 ± 3.4%) ($p < 0.01$). There is no significant difference between TMVH and TMVL groups. In addition, the fusion indices for cells in RGDH and RGDL (83.7 ± 4.4% and 80.2 ± 2.9%, respectively) are significant higher than counterparts in TMVH, TMVL and control groups ($p < 0.01$). There is no significant difference between RGDH and RGDL groups. Furthermore, the maturation indices of cells in RGDH and RGDL groups (77.9 ± 2.6% and 80.0 ± 2.2%, respectively) are statistically higher than TMVH, TMVL, and control groups (58.8 ± 5.3%, 58.8 ± 5.3%

18

and 49.8 $\pm$ 5.9 %, respectively). Taken together, the myotubes in RGDH and RGDL had the highest level of differentiation, which is consistent with previous report that RGD peptide promotes the myotubes differentiation.[57-59] Cells in TMVH and TMVL also increased the level of differentiation compared to control groups.
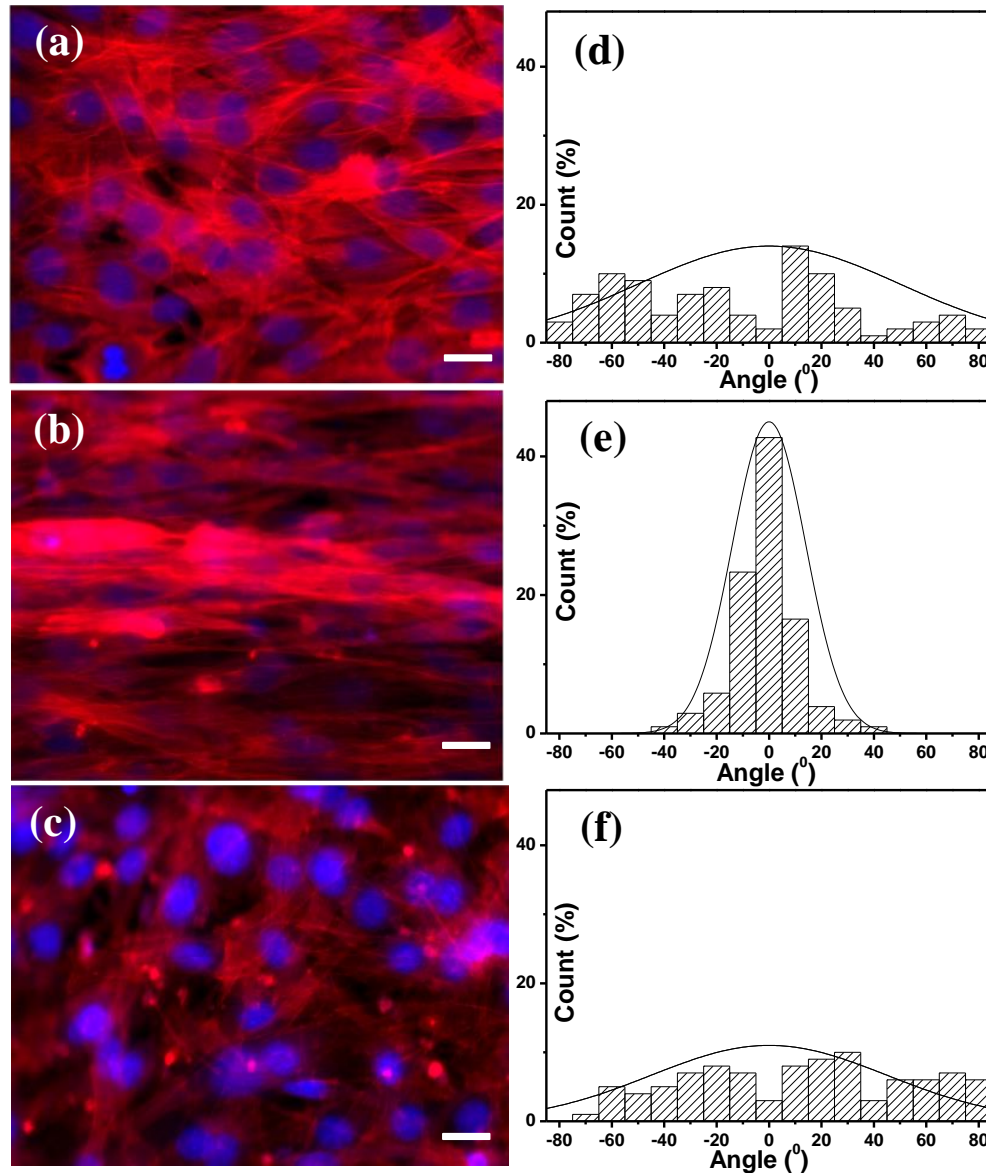
Figure 1.9. Immunofluorescent images of myoblasts (a-c), nuclei are DAPI-stained (blue), and actin filaments are rhodamine-phalloidin stained (red). Angular spread of myoblast actin filaments with respect to the flow direction is shown in (d-f). Un-aligned TMV as control (a and d); high coverage aligned TMV (b and e); and low coverage aligned TMV (c and f). All scale bars indicate 100 μm.[1]

19

Previous study has observed that the alignment of myoblasts promote their differentiation.[60] The differentiation of myoblasts depends on two critical events: the growth arrest [61] and the end-to-end contacts between myoblasts.[62] In day 3, we observed the C2C12 cells aligned along the orientation of TMV particles by F-actin staining (Figure 1.9). The alignment of myoblasts on capillary tubes with TMV particles may enhance aligned end-to-end contacts between the cells. Therefore higher percentages of cells in groups with aligned orientation were fused to differentiate into myotubes than control groups.

1.3 CONCLUSIONS

In this work, we have demonstrated that the fluid flow assembly can serve as a facile and robust method to align 1D NPs in large scale. The formation of thus aligned 1D NPs was dominated by the shearing force generated by the fluid flow, interactions between 1D NPs and substrate, and the following drying process. In addition, the alignment degree and coverage of the 1D NPs can be readily controlled by the flow rate, the concentration and the nature properties (length and modulus) of the 1D NPs. In general, a better aligned structure can be produced when longer and stiffer 1D NPs are used at higher flow rate and higher concentration. This method has been used to align various kinds of 1D NPs, including rod-like viral particles, hybridized conductive nanowires, and inorganic 1D NPs. Capitalizing on the simplicity, flexibility and macro-scale of this method, this technique can engineer aligned 1D NPs, with wide potential applications on tissue engineering, electronic, and optical fields. Furthermore, compared to control group, the aligned virus particles successfully guided myotubes alignment, and enhanced the myogenic differentiation of myoblasts. In summary, we envision this method can be employed to

mimic organized structures of the extracellular matrix (ECM), and can support and dictate the cell growth, spreading and other responses, which is critical for many applications in the emerging field of tissue engineering.

1.4 EXPERIMENTS

1.4.1 Materials

Poly(acrylic acid) (PAA) (*MW* 450000), poly(diallyldimethylammonium chloride) (PDDA) (20 wt % in water, *M*~200 000-350 000 g/mol), poly(styrene sulfonate) (PSS) (*MW* 70000 g/mol), chitosan (high purity, *MW* 60000-120000) and aminopropyltriethoxysilane (APTES) were purchased from Sigma-Aldrich; the materials were used as received. Deionized water (18.2 MΩ.cm) used for rinsing and preparing all the solutions was obtained from a Millipore Simplicity 185 purification unit. Serum media, DMEM high glucose, was made by adding 6.7 g powder media (Hyclone, SH30003.03), 1.2 g sodium bicarbonate (Fisher Scientific , S233-500), 3.57 g HEPES (Cellgro, 61-034-RM), 5.0 mL L-glutamine solution (Invitrogen, 25030081), and 5 mL penicillin-streptomycin (Invitrogen, 15140122) to 500 mL water (Millipore Synergy UV system, 18.2 MΩ.cm). The solution was then brought to pH 7.4 using 1 M sodium hydroxide solution (J.T. Baker, E31H10). The media was sterilized by vacuum filtration using a low protein binding media filter (Corning 0.22 μm, 431097). Then after filtration 50 mL fetal bovine serum (FBS) was added (Atlanta Biologicals, S12450).

1.4.2 Purification of 1D NPs

The TMV, TMVRGD1 and PVX were harvested from the infected leaves according to the reported methods.[30-31] Briefly, 10 mM potassium phosphate buffer (pH 7.4) with

21

0.2% β-mercaptoethanol was added into crashed leaves, and centrifuged at 9000 rpm for 15 min. The supernatant was clarified with equal volume of CHCl₃ and n-butanol (1:1 ratio). Toward the aqueous supernatant, 10% PEG800 and 0.2 M NaCl were added to precipitate TMV. After the centrifugation, the pellets were resuspended in 10 mM phosphate buffer. Finally, the pure viruses were obtained after the process of ultracentrifugation for 2.5 h at 42 000 rpm (rotor Ti 75).

1.4.3 Filamentous Bacteriophage.

M13 was harvested from the infected E. coli according to previously reported method.[38,63] Briefly, 1 L of E. coli ER2738 culture was grown in LB-tet media to mid-log phase and infected with 1 mL of wild type M13 bacteriophage (1012 PFU/mL). The culture was incubated at 37 °C with shaking for 5-6 h, centrifuged to remove bacterial cells, the virus collected by PEG-NaCl (20% PEG and 2.5 mol L^{-1} NaCl) precipitation and reconstituted in Tris buffer.

1.4.4 Synthesis of TMV-Aniline Fibers

TMV-Aniline fibers was synthesized according to reported method.[64] Briefly, distilled aniline (10 L) and ammonium persulfate (10 mg mL^{-1}, 1 mL) were added to TMV solution (1 mg mL^{-1}, 4 mL). The reaction was taken at room temperature for 24 h. The reaction mixture was purified by dialysis for 5 h.

1.4.5 Synthesis of Gold Nanorods (GNRs)

GNRs was synthesized according to the seed-mediate growth method.[45] The seed solution is prepared as follows: the 0.6 mL ice-cold NaBH4 (10 mM) was added into the mixture of CTAB solution (5 mL, 0.2 M) and HAuCl4 (5 mL, 0.5 mM); vigorous stirring

22

of the seed solution for 3 minutes. The growth solution was prepared by mixing CTAB solution (0.2 M) and HAuCl4 (0.5 mM) with same volume. The GNRs growth was achieved by three steps: 1) 0.2 mL seeding solution was added into 2 mL growth solution, which was transferred to 20 mL growth solution after 10 s; 2) after 30 s, the solution in step 2 was poured into 200 mL growth solution; 3) the GNRs was synthesized by incubating the solution at 25 °C for 18h. The GNRs was purified by centrifuge with spin speed 4000 rpm for 8 min. After re-dispersed into water, the GNRs were used for the assembly.

1.4.6 Modifications of Capillary Tube

The polyelectrolyte coated capillaries were obtained by alternatively immersing capillaries in PDDA (1 mg mL^{-1}) for 20 min and PSS or PAA solution (1.0 mg mL^{-1}) for 20 min, until (PDDA/PAA)$_3$ or (PDDA/PSS)$_3$ are obtained, where the value 3 indicates the number of bilayers. Water was used to rinse in between each deposition step until the desired number of layers was obtained. For chitosan modified capillaries: By immersing into chitosan (1 mg mL^{-1} in 0.1% acetic acid at pH=6.5), the chitosan coated capillaries were obtained. The resulting samples were washed by water before using. The APTES modified capillaries: Capillaries were immersed into 1% APTES in ethanol/water (95:5 by volume) for 10 min and washed with pure ethanol three times, and dried with Nitrogen, then incubated in vacuum at 120-130 °C for one hour.

1.4.7 Flow Assembly of 1D NPs

Typically, 10 mL solution containing 1 D NPs was injected into the 1D NPs feeder (Figure 1.1a), whose one end was connected to nitrogen tank and the other end was

23

connected to capillary tube. The solution was driven through the capillary tube, and dried by the following gas. The flow rate of solution was controlled by the gas pressure applied to the flow.

1.4.8 Characterization of 1D NPs

A solution of 1D NPs was dropped on the glow-discharged Formvar-carbon coated copper grid. After drying, the sample was negatively stained with 2% uranyl acetate for TEM (Philips CM-12 transmission electron microscope at 80 kEV) observation. The surface morphology was observed by AFM (SPA300, Seiko) in the tapping mode. The angles of 1D NPs were measured with ImageJ software and then plotted in angular distribution histograms. For M13, segments longer than 500 nm were measured for plot.

1.4.9 Cell Culture

The murine-derived muscle cell line, C2C12, was purchased from American Type Culture Collection (ATCC, Manassas, VA). Cells were cultured in Dulbecco's modified Eagle's medium (DMEM, #D6046, Sigma–Aldrich) supplemented with 10% heat inactivated fetal bovine serum (Hyclone, Thermo Scientific), 100 U mL^{-1} penicillin and 100 μg·mL^{-1} streptomycin (Gibco BRL, Invitrogen Corp., Carlsbad, CA, USA). C2C12 at 80-90% confluency were detached and re-suspend into culture medium in a concentration of 2×10^6 cells per mL. The capillary tubes with TMV particles sucked the cell suspension. After 5 hours, put the tubes with cells into the 12 well plates with culture medium. After three days, the cells were shifted to differentiation medium (DM), which is DMEM supplemented with 2% horse serum (Lonza Inc., Williamsport, PA). The medium was replaced every other day. The time points in the figures indicate time after shifting to DM.

24

1.4.10 Immunofluorescence Microscopy

Differentiated C2C12 cells were washed once with PBS and fixed with 4% paraformaldehyde (Sigma-Aldrich, P6148) in PBS for 15 minutes. Cells were then blocked with 5% goat serum and 0.3% TritonX100 for 60 min in PBS. The cells were incubated with MF20 (anti-myosin heavy chain (MHC), Developmental Studies Hybridoma Bank (DSHB), University of Iowa, IA) overnight at 4 °C and followed by Chromeo^{TM} 642 Goat anti-Mouse lgG (Active motif, Germany) and DAPI (Sigma, USA) in dark. Cells then were imaged using an Olympus IX81 microscope. The images were analyzed with ImageJ software. The images obtained from the MHC and DAPI signals were pseudo-colored red and blue respectively.

1.4.11 Calculation of Fusion Index and Maturation Index

The fusion index was calculated by determining the ratio of nuclei number in myocytes with two or more nuclei over the total number of nuclei. The maturation index was the percentage of myotubes with five or more nuclei. Because the cells are in the capillary tubes, cells on the edge were out of focus in images with low magnification. Cells on the edge, which were out of focus, were not used for analysis.

1.4.12 Statistical Analysis

Statistical analysis for mean comparison was performed by using one-way analysis of variance (ANOVA) Turkey's test in OriginPro 8.5. All data values in this study were reported as mean ± standard error of the mean.

Table 1.1. Sample preparation conditions and results.

Samples	Modification [a]	Surface charge	Phosphate buffer concentration (mM)	Flow rate ($cm\ s^{-1}$)	Washed before dry[b]	Results	
						HPW (°)[c]	Surface coverage (%)
Typical	Chitosan$_1$	+	0	200	N	28 (Y)	96
Control 1	Chitosan$_1$	+	0	0	N	176 (N)	44
Control 2	PDDA$_1$	+	0	200	N	29 (Y)	88
Control 3	APTES$_1$	+	0	200	N	29 (Y)	87
Control 4	(PDDA/PSS)$_3$	-	0	200	N	170 (N)	5
Control 5	(PDDA/PAA)$_3$	-	0	200	N	169 (N)	8
Control 6	Glass	Neutral	0	200	N	172 (N)	10
Control 7	Chitosan$_1$	+	50	200	N	46 (N)	57
Control 8	Chitosan$_1$	+	0	200	Y	30 (Y)	63

Note: [a] The subscript in this column noted as the modification cycle number; and the modification methods are shown in experimental part. [b] The sample was washed by water (Y) or not (N) before it was dried. [c] The aligned structure as Figure 1.1e can be obtained (Y) or not (N).

Table 1.2. Parameters of different 1D NPs used in experiments.

1D NPs	TMV	PVX	TMV-Aniline fiber	M13	GNRs
Contour length L (nm)	300	550	4, 000	880	350
Diameter (nm)	18	13.5	18.5	4.5	25
Aspect ratio	17	41	216	196	16
Persistent length P (μm)	~1, 000[65]	-	-	1.27[66]	-
Modulus (GPa)	1.1[67-68]	0.85[67]	1.23[66]	0.62[67-68]	64[69]

1.5 REFERENCE

1.   Zan, X.; Feng, S.; Balizan, E.; Lin, Y.; Wang, Q. Facile method for large scale alignment of one dimensional nanoparticles and control over myoblast orientation and differentiation. *ACS Nano* **2013,** *7* (10), 8385-96.

2.   Tay, C. Y.; Irvine, S. A.; Boey, F. Y. C.; Tan, L. P.; Venkatraman, S. Micro-/Nano-engineered Cellular Responses for Soft Tissue Engineering and Biomedical Applications. *Small* **2011,** *7* (10), 1361-78.

3.   Chung, W. J.; Oh, J. W.; Kwak, K.; Lee, B. Y.; Meyer, J.; Wang, E.; Hexemer, A.; Lee, S. W. Biomimetic self-templating supramolecular structures. *Nature* **2011,** *478* (7369), 364-8.

4.   Sun, B. Q.; Sirringhaus, H. Surface tension and fluid flow driven self-assembly of ordered ZnO nanorod films for high-performance field effect transistors. *J Am Chem Soc* **2006,** *128* (50), 16231-7.

5.   Duan, X. F.; Niu, C. M.; Sahi, V.; Chen, J.; Parce, J. W.; Empedocles, S.; Goldman, J. L. High-performance thin-film transistors using semiconductor nanowires and nanoribbons. *Nature* **2003,** *425* (6955), 274-8.

6.   Murphy, C. J.; San, T. K.; Gole, A. M.; Orendorff, C. J.; Gao, J. X.; Gou, L.; Hunyadi, S. E.; Li, T. Anisotropic metal nanoparticles: Synthesis, assembly, and optical applications. *J Phys Chem B* **2005,** *109* (29), 13857-70.

7.   Xia, Y. N.; Yang, P. D.; Sun, Y. G.; Wu, Y. Y.; Mayers, B.; Gates, B.; Yin, Y. D.; Kim, F.; Yan, Y. Q. One-dimensional nanostructures: Synthesis, characterization, and applications. *Adv Mater* **2003,** *15* (5), 353-89.

8.   Hone, J.; Llaguno, M. C.; Nemes, N. M.; Johnson, A. T.; Fischer, J. E.; Walters, D. A.; Casavant, M. J.; Schmidt, J.; Smalley, R. E. Electrical and thermal transport properties of magnetically aligned single walt carbon nanotube films. *Appl Phys Lett* **2000,** *77* (5), 666-8.

9.   Wang, X. B.; Liu, Y. Q.; Yu, G.; Xu, C. Y.; Zhang, J. B.; Zhu, D. B. Anisotropic electrical transport properties of aligned carbon nanotube films. *J Phys Chem B* **2001,** *105* (39), 9422-5.

10.   Heo, K.; Cho, E.; Yang, J.-E.; Kim, M.-H.; Lee, M.; Lee, B. Y.; Kwon, S. G.; Lee, M.-S.; Jo, M.-H.; Choi, H.-J.; Hyeon, T.; Hong, S. Large-Scale Assembly of Silicon Nanowire Network-Based Devices Using Conventional Microfabrication Facilities. *Nano Letters* **2008,** *8* (12), 4523-7.

11.   Rao, S. G.; Huang, L.; Setyawan, W.; Hong, S. Nanotube electronics: large-scale assembly of carbon nanotubes. *Nature* **2003,** *425* (6953), 36-7.

12.   Li, L. S.; Alivisatos, A. P. Semiconductor nanorod liquid crystals and their assembly on a substrate. *Adv Mater* **2003,** *15* (5), 408-11.

13.   Javey, A.; Nam; Friedman, R. S.; Yan, H.; Lieber, C. M. Layer-by-Layer Assembly of Nanowires for Three-Dimensional, Multifunctional Electronics. *Nano Letters* **2007,** *7* (3), 773-7.

14.   Fan, Z.; Ho, J. C.; Jacobson, Z. A.; Yerushalmi, R.; Alley, R. L.; Razavi, H.; Javey, A. Wafer-Scale Assembly of Highly Ordered Semiconductor Nanowire Arrays by Contact Printing. *Nano Letters* **2007,** *8* (1), 20-5.

15.   Takahashi, T.; Takei, K.; Ho, J. C.; Chueh, Y.-L.; Fan, Z.; Javey, A. Monolayer Resist for Patterned Contact Printing of Aligned Nanowire Arrays. *J Am Chem Soc* **2009,** *131* (6), 2102-3.

16.   Harnack, O.; Pacholski, C.; Weller, H.; Yasuda, A.; Wessels, J. M. Rectifying behavior of electrically aligned ZnO nanorods. *Nano Letters* **2003,** *3* (8), 1097-101.

17.   Huang, Y. Directed Assembly of One-Dimensional Nanostructures into Functional Networks. *Science* **2001,** *291* (5504), 630-3.

18.   Raez, J.; Moralez, J. G.; Fenniri, H. Long-range flow-induced alignment of self-assembled rosette nanotubes on Si/SiOx and poly(methyl methacrylate)-coated Si/SiOx. *J Am Chem Soc* **2004,** *126* (50), 16298-9.

19.   Kim, F.; Kwan, S.; Akana, J.; Yang, P. D. Langmuir-Blodgett nanorod assembly. *J Am Chem Soc* **2001,** *123* (18), 4360-1.

20.   Phillips, J. B.; Bunting, S. C. J.; Hall, S. M.; Brown, R. A. Neural tissue engineering: A self-organizing collagen guidance conduit. *Tissue Eng* **2005,** *11* (9-10), 1611-7.

21.   Crabb, R. A. B.; Chau, E. P.; Evans, M. C.; Barocas, V. H.; Hubel, A. Biomechanical and microstructural characteristics of a collagen film-based corneal stroma equivalent. *Tissue Eng* **2006,** *12* (6), 1565-75.

22.   Zhu, Y. B.; Cao, Y.; Pan, J.; Liu, Y. X. Macro-Alignment of Electrospun Fibers For Vascular Tissue Engineering. *J Biomed Mater Res B* **2010,** *92B* (2), 508-16.

23.   Wigmore, P. M.; Dunglison, G. F. The generation of fiber diversity during myogenesis. *Int J Dev Biol* **1998,** *42* (2), 117-25.

24.   Papadaki, M.; Bursac, N.; Langer, R.; Merok, J.; Vunjak-Novakovic, G.; Freed, L. E. Tissue engineering of functional cardiac muscle: molecular, structural, and electrophysiological studies. *Am J Physiol-Heart C* **2001,** *280* (1), H168-H178.

25.   Grefte, S.; Kuijpers-Jagtman, A. M.; Torensma, R.; Von den Hoff, J. W. Skeletal muscle development and regeneration. *Stem Cells Dev* **2007,** *16* (5), 857-68.

26.   Daley, W. P.; Peters, S. B.; Larsen, M. Extracellular matrix dynamics in development and regenerative medicine. *J Cell Sci* **2008,** *121* (3), 255-64.

27.   Lanfer, B.; Seib, F. P.; Freudenberg, U.; Stamov, D.; Bley, T.; Bornhauser, M.; Werner, C. The growth and differentiation of mesenchymal stem and progenitor cells cultured on aligned collagen matrices. *Biomaterials* **2009,** *30* (30), 5950-8.

28.   Lin, Y.; Balizan, E.; Lee, L. A.; Niu, Z. W.; Wang, Q. Self-Assembly of Rodlike Bio-nanoparticles in Capillary Tubes. *Angew Chem Int Edit* **2010,** *49* (5), 868-72.

29.   Shirokikh, N. E.; Agalarov, S. C.; Spirin, A. S. Chemical and enzymatic probing of spatial structure of the omega leader of tobacco mosaic virus RNA. *Biochemistry-Moscow* **2010,** *75* (4), 405-11.

30.   Lee, L. A.; Nguyen, Q. L.; Wu, L. Y.; Horyath, G.; Nelson, R. S.; Wang, Q. Mutant Plant Viruses with Cell Binding Motifs Provide Differential Adhesion Strengths and Morphologies. *Biomacromolecules* **2012,** *13* (2), 422-31.

31.   Wu, L. Y.; Zang, J. F.; Lee, L. A.; Niu, Z. W.; Horvatha, G. C.; Braxtona, V.; Wibowo, A. C.; Bruckman, M. A.; Ghoshroy, S.; zur Loye, H. C.; Li, X. D.; Wang, Q. Electrospinning fabrication, structural and mechanical characterization of rod-like virus-based composite nanofibers. *J Mater Chem* **2011,** *21* (24), 8550-7.

30

32.   Kobayashi, M.; Seki, M.; Tabata, H.; Watanabe, Y.; Yamashita, I. Fabrication of Aligned Magnetic Nanoparticles Using Tobamoviruses. *Nano Letters* **2010,** *10* (3), 773-6.

33.   Xu, H.; Cao, B. R.; George, A.; Mao, C. B. Self-Assembly and Mineralization of Genetically Modifiable Biological Nanofibers Driven by beta-Structure Formation. *Biomacromolecules* **2011,** *12* (6), 2193-9.

34.   Gilliland, A.; Singh, D. P.; Hayward, J. M.; Moore, C. A.; Murphy, A. M.; York, C. J.; Slator, J.; Carr, J. P. Genetic modification of alternative respiration has differential effects on antimycin A-induced versus salicylic acid-induced resistance to Tobacco mosaic virus. *Plant Physiol* **2003,** *132* (3), 1518-28.

35.   Wu, L. Y.; Lee, L. A.; Niu, Z. W.; Ghoshroy, S.; Wang, Q. Visualizing Cell Extracellular Matrix (ECM) Deposited by Cells Cultured on Aligned Bacteriophage M13 Thin Films. *Langmuir* **2011,** *27* (15), 9490-6.

36.   Kaur, G.; Valarmathi, M. T.; Potts, J. D.; Jabbari, E.; Sabo-Attwood, T.; Wang, Q. Regulation of osteogenic differentiation of rat bone marrow stromal cells on 2D nanorod substrates. *Biomaterials* **2010,** *31* (7), 1732-41.

37.   Zhu, H. B.; Cao, B. R.; Zhen, Z. P.; Laxmi, A. A.; Li, D.; Liu, S. R.; Mao, C. B. Controlled growth and differentiation of MSCs on grooved films assembled from monodisperse biological nanofibers with genetically tunable surface chemistries. *Biomaterials* **2011,** *32* (21), 4744-52.

38.   Wu, L.; Lee, L. A.; Niu, Z.; Ghoshroy, S.; Wang, Q. Visualizing Cell Extracellular Matrix (ECM) Deposited by Cells Cultured on Aligned Bacteriophage M13 Thin Films. *Langmuir* **2011,** *27* (15), 9490-6.

31

39.   Rong, J.; Lee, L. A.; Li, K.; Harp, B.; Mello, C. M.; Niu, Z.; Wang, Q. Oriented cell growth on self-assembled bacteriophage M13 thin films. *Chemical Communications* **2008,** (41), 5185-7.

40.   Sitasuwan, P.; Andrew Lee, L.; Bo, P.; Davis, E. N.; Lin, Y.; Wang, Q. A plant virus substrate induces early upregulation of BMP2 for rapid bone formation. *Integrative Biology* **2012,** *4* (6), 651-60.

41.   Niu, Z.; Bruckman, M. A.; Li, S.; Lee, L. A.; Lee, B.; Pingali, S. V.; Thiyagarajan, P.; Wang, Q. Assembly of Tobacco Mosaic Virus into Fibrous and Macroscopic Bundled Arrays Mediated by Surface Aniline Polymerization. *Langmuir* **2007,** *23* (12), 6719-24.

42.   Lanfer, B.; Freudenberg, U.; Zimmermann, R.; Stamov, D.; Körber, V.; Werner, C. Aligned fibrillar collagen matrices obtained by shear flow deposition. *Biomaterials* **2008,** *29* (28), 3888-95.

43.   Steinmetz, N. F.; Mertens, M. E.; Taurog, R. E.; Johnson, J. E.; Commandeur, U.; Fischer, R.; Manchester, M. Potato Virus X as a Novel Platform for Potential Biomedical Applications. *Nano Letters* **2009,** *10* (1), 305-12.

44.   Niu, Z.; Bruckman, M.; Harp, B.; Mello, C.; Wang, Q. Bacteriophage M13 as a scaffold for preparing conductive polymeric composite fibers. *Nano Research* **2008,** *1* (3), 235-41.

45.   Murphy, C. J.; Sau, T. K.; Gole, A. M.; Orendorff, C. J.; Gao, J.; Gou, L.; Hunyadi, S. E.; Li, T. Anisotropic Metal Nanoparticles: Synthesis, Assembly, and Optical Applications. *The Journal of Physical Chemistry B* **2005,** *109* (29), 13857-70.

46.   Menagen, G.; Macdonald, J. E.; Shemesh, Y.; Popov, I.; Banin, U. Au Growth on Semiconductor Nanorods: Photoinduced versus Thermal Growth Mechanisms. *J Am Chem Soc* **2009,** *131* (47), 17406-11.

47.   Chaney, S. B.; Shanmukh, S.; Dluhy, R. A.; Zhao, Y. P. Aligned silver nanorod arrays produce high sensitivity surface-enhanced Raman spectroscopy substrates. *Appl Phys Lett* **2005,** *87* (3).

48.   Perez-Juste, J.; Rodriguez-Gonzalez, B.; Mulvaney, P.; Liz-Marzan, L. M. Optical control and patterning of gold-nanorod-poly(vinyl alcohol) nanocomposite films. *Adv Funct Mater* **2005,** *15* (7), 1065-71.

49.   Aubin, H.; Nichol, J. W.; Hutson, C. B.; Bae, H.; Sieminski, A. L.; Cropek, D. M.; Akhyari, P.; Khademhosseini, A. Directed 3D cell alignment and elongation in microengineered hydrogels. *Biomaterials* **2010,** *31* (27), 6941-51.

50.   Faureau, C.; Delbarre, E.; Courvalin, J. C.; Buendia, B. Differentiation of C2C12 myoblasts expressing lamin A mutated at a site responsible for Emery-Dreifuss muscular dystrophy is improved by inhibition of the MEK-ERK pathway and stimulation of the PI3-kinase pathway. *Exp Cell Res* **2008,** *314* (6), 1392-405.

51.   Li, B.; Lin, M.; Tang, Y.; Wang, B.; Wang, J. H. C. A novel functional assessment of the differentiation of micropatterned muscle cells. *J Biomech* **2008,** *41* (16), 3349-53.

52.   Fanzani, A.; Stoppani, E.; Gualandi, L.; Giuliani, R.; Galbiati, F.; Rossi, S.; Fra, A.; Preti, A.; Marchesini, S. Phenotypic behavior of C2C12 myoblasts upon expression of the dystrophy-related caveolin-3 P104L and TFT mutants. *Febs Lett* **2007,** *581* (26), 5099-104.

53.   Bajaj, P.; Reddy, B.; Millet, L.; Wei, C. N.; Zorlutuna, P.; Bao, G.; Bashir, R. Patterning the differentiation of C2C12 skeletal myoblasts. *Integrative Biology* **2011,** *3* (9), 897-909.

54.   Kaur, G.; Wang, C.; Sun, J. A.; Wang, Q. A. The synergistic effects of multivalent ligand display and nanotopography on osteogenic differentiation of rat bone marrow stem cells. *Biomaterials* **2010,** *31* (22), 5813-24.

55.   Zan, X. J.; Sitasuwan, P.; Powell, J.; Dreher, T. W.; Wang, Q. Polyvalent display of RGD motifs on turnip yellow mosaic virus for enhanced stem cell adhesion and spreading. *Acta Biomater* **2012,** *8* (8), 2978-85.

56.   Sun, Y. T.; Ge, Y. J.; Dmevich, J.; Zhao, Y.; Band, M.; Chen, J. Mammalian target of rapamycin regulates miRNA-1 and follistatin in skeletal myogenesis. *J Cell Biol* **2010,** *189* (7), 1157-69.

57.   Boontheekul, T.; Kong, H. J.; Hsiong, S. X.; Huang, Y. C.; Mahadevan, L.; Vandenburgh, H.; Mooney, D. J. Quantifying the relation between bond number and myoblast proliferation. *Faraday Discuss* **2008,** *139*, 53-70.

58.   Rowley, J. A.; Mooney, D. J. Alginate type and RGD density control myoblast phenotype. *J Biomed Mater Res* **2002,** *60* (2), 217-23.

59.   Lee, L. A.; Nguyen, Q. L.; Wu, L.; Horvath, G.; Nelson, R. S.; Wang, Q. Mutant plant viruses with cell binding motifs provide differential adhesion strengths and morphologies. *Biomacromolecules* **2012,** *13* (2), 422-31.

60.   Wang, P. Y.; Yu, H. T.; Tsai, W. B. Modulation of Alignment and Differentiation of Skeletal Myoblasts by Submicron Ridges/Grooves Surface Structure. *Biotechnol Bioeng* **2010,** *106* (2), 285-94.

61.   Olson, E. N. Interplay between Proliferation and Differentiation within the Myogenic Lineage. *Dev Biol* **1992,** *154* (2), 261-72.

62.   Clark, P.; Dunn, G. A.; Knibbs, A.; Peckham, M. Alignment of myoblasts on ultrafine gratings inhibits fusion in vitro. *Int J Biochem Cell B* **2002,** *34* (7), 816-25.

63.   Niu, Z.; Bruckman, M. A.; Harp, B.; Mello, C. M.; Wang, Q. Bacteriophage M13 as a Scaffold for Preparing Conductive Polymeric Composite Fibers. *Nano Research* **2008,** *1* (3), 235-41.

64.   Niu, Z.; Bruckman, M.; Kotakadi, V. S.; He, J.; Emrick, T.; Russell, T. P.; Yang, L.; Wang, Q. Study and characterization of tobacco mosaic virus head-to-tail assembly assisted by aniline polymerization. *Chemical Communications* **2006,** (28), 3019-21.

65.   Dogic, Z.; Fraden, S. Smectic phase in a colloidal suspension of semiflexible virus particles. *Phys Rev Lett* **1997,** *78* (12), 2417-20.

66.   Khalil, A. S.; Ferrer, J. M.; Brau, R. R.; Kottmann, S. T.; Noren, C. J.; Lang, M. J.; Belcher, A. M. Single M13 bacteriophage tethering and stretching. *Proc. Natl. Acad. Sci. U. S. A.* **2007,** *104* (12), 4892-7.

67.   Tao, L.; Zan, X. J.; Wang, Q.; Lee, B. Assembly of Rodlike Tobacco Mosaic Virus into Superlattice through Depletion Interaction. *Langmuir* **2013,** 29 (41), 12777–84.

68.   Wang, X.; Niu, Z.; Li, S.; Wang, Q.; Li, X. Nanomechanical characterization of polyaniline coated tobacco mosaic virus nanotubes. *Journal of Biomedical Materials Research Part A* **2008,** *87A* (1), 8-14.

69.   Petrova, H.; Perez-Juste, J.; Zhang, Z.; Zhang, J.; Kosel, T.; Hartland, G. V. Crystal structure dependence of the elastic constants of gold nanorods. *J Mater Chem* **2006,** *16* (40), 3957-63.

CHAPTER 2

FLOW ASSEMBLY OF TMV MUTANTS TO GUIDE DIRECTIONAL OUTGROWTH OF NEURITES

2.1 INTRODUCTION

Tissue engineering provides a new therapeutic approach to regenerate or replace damaged or diseased tissues with malfunctions by using biomaterials either with or without living precursor cells.[1] Thus, an ideal tissue engineering scaffold should bring to cells with desired microenvironment that supports cellular growth and functions. The extracellular matrix (ECM) play an important role in the microenvironment because cells are in direct contact with ECM, which provides biochemical and mechanical cues to guide cellular behavior and organization *in vivo*.[2] Therefore, various biomaterials scaffolds, such as electrospinning scaffolds,[3] hydrogels,[4] self-assembly of peptides,[5] has been generated to mimic the ECM. These biomaterials, that either resemble the nature structures of ECM or possess biochemical compositions of ECM, may be useful in the tissue engineering field.

Recently, through chemical or genetic modification, viral particles have been used to display various peptides.[6] The resulting virus mutants have been extensively applied for biomedical application, such as vaccine generation,[7] stem cell differentiation,[8] and drug delivery.[9] In particularly, tobacco mosaic virus (TMV) is a rodlike plant virus with a capsid that is composed of 2130 identical copies of a protein monomer (coat protein, CP) and a single-stranded 6.4 kb ribonucleotide. The intact capsid of TMV is 18 nm in diameter and 300 nm in length.[10] By genetically fusing a cell binding motif to the surface exposed,

36

carboxyl end of the CP, the virus particles displaying 2130 identical cell binding motifs can be achieved. With this strategy, Lee et al. have generated TMV mutants displaying cell binding motifs (*i.e.* RGD1, RGD7, PSHRN3, P15, and DEGA) and investigated their effects on cellular morphologies and adhesion.[11] Since a previous study indicated that ECM derived peptides, such as RGD and PHSRN, could assist neural cells adhesion and promote neurite outgrowth, we hypothesize that the TMV mutants bearing ECM derived peptides can be used for neural tissue engineering.

Peripheral nerve injuries have caused much suffering every year. The most severe injury is a complete nerve transection. Clinical treatments typically consist of either directly end-to-end suturing the transected position (for small defects or gaps) or applying an autologous/allogeneic nerve grafts (for longer nerve gaps).[12] Although numerous FDA approved guidance conduits have been applied to treat the peripheral neural injuries, the effects of those materials are limited.[13] A plausible explanation for the limited efficacy of artificial nerve conduits is lack of physical guidance for the cells at a relevant nano-scale.[14] Therefore, besides meeting the general requirement for biomaterials, such as being biodegradable, permeable, and biocompatible, an ideal nerve conduit need to acquire the feature of displaying biochemical cues and topographical cues for nerve regeneration inside.

Numerous studies have shown that the nano or micro scale topographical feature are of importance for cells to possess proper orientation and function.[15-17] Previously, we have developed a facile method for large scale alignment of one dimensional (1D) nanoparticles in capillary tubes using external shear force. By doing so, various 1D nanoparticles can be aligned homogeneously in the inner surface of capillaries and provide

37

a topographical cues to guide cell orientation.[18] Since this approach can be achieved in biodegradable polymer capillaries, a potential application of this method is the fabrication of nerve conduits.

This chapter presents our *in vitro* investigation of growing neural cells N2a on substrates coated by TMV mutants with cell binding motifs. We demonstrated that the TMV mutants are able to maintain cell viability, proliferation, and neurite outgrowth. By aligning TMV mutants with shear force, we can achieve both homogeneously displaying cell binding motifs and topographical cues in the inner surface of capillaries. The resulting capillaries could be applied to guide directional neurite outgrowth of N2a *in vitro*.

2.2 RESULTS AND DISCUSSION

2.2.1 Cytocompatibility of TMV Mutants

Neural crest is a transient embryonic structure in vertebrates in which cells generate most of the peripheral nervous system and several non-neural cell types.[19] N2a cells is a mouse neural crest-derived cell line that has been extensively used for studies of neural differentiation,[20] neurite outgrowth,[21] and signaling pathway.[22] Since we sought to apply our newly generated materials in the repairmen of peripheral neural injuries, N2a cells are used to verify the biological compatibility of various TMV mutants. Before the cell experiments, various TMV mutants were isolated from tobacco leaves and characterized by MALDI-TOF MS and TEM imaging prior use (Table 2.1 and Figure 2.1).

As with any biomaterial, a prerequisite task is to ensure they are non-toxic to the target cells. To investigate the toxic effect of TMV-wildtype, and mutants including RGD1, RGD7, P15, DGEA, and PHSRN3, were added to culture medium of N2a at various concentration. Cell viability and proliferation were the measured with CellTiter Blue assay

at day 1, 3, and 5 after TMV addition and compared to the population of cells cultured in the same culture media without TMV (Figure 2.2a). N2a cells grown in media supplemented with RGD1-, RGD7-, PHSRN3-, P15-, DEGA-, and wildtype-TMV showed similar number as the control at each of the concentrations and time points measured. Moreover, as the positive control group, cells in TMV media showed significant proliferation over the tested period ($P < 0.001$, two-way ANOVA with replication, $n = 6$).

Table 2.1. List of isolated TMV mutants

Virus	Insert Sequence	Calculated Mass (m/z)	Observed mass (m/z)
TMV-wt	N/A	17534	17533
TMV-RGD1	GRGDSPG	18161	18165
TMV-RGD7	AVTGRGDSPASS	18621	18622
TMV-DGEA	DGEA	17908	17950
TMV-PHSRN3	EDVRPHSRNSIT	18927	18957
TMV-P15	GTPGPQGIAGQRGVV	18910	18903
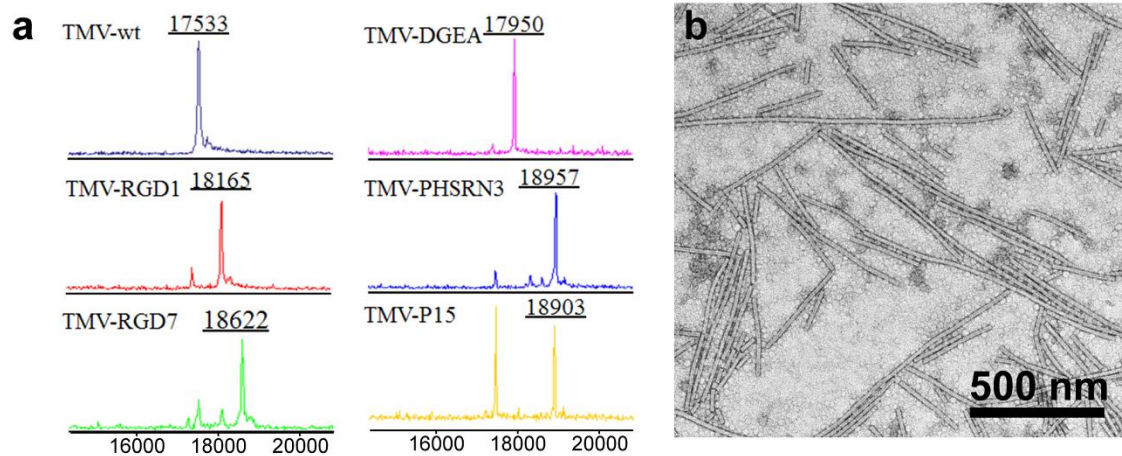
Figure 2.1. Characterizations of TMV mutants. (a) Direct detection of the coat protein from crude plant sap by MALDI-TOF MS. TMV mutants were detected on various positions regarding to their molecular weights. (b) Transmission electron microscopy image of an isolated TMV mutant, TMV-RGD1. The scale bar indicates 500 nm.
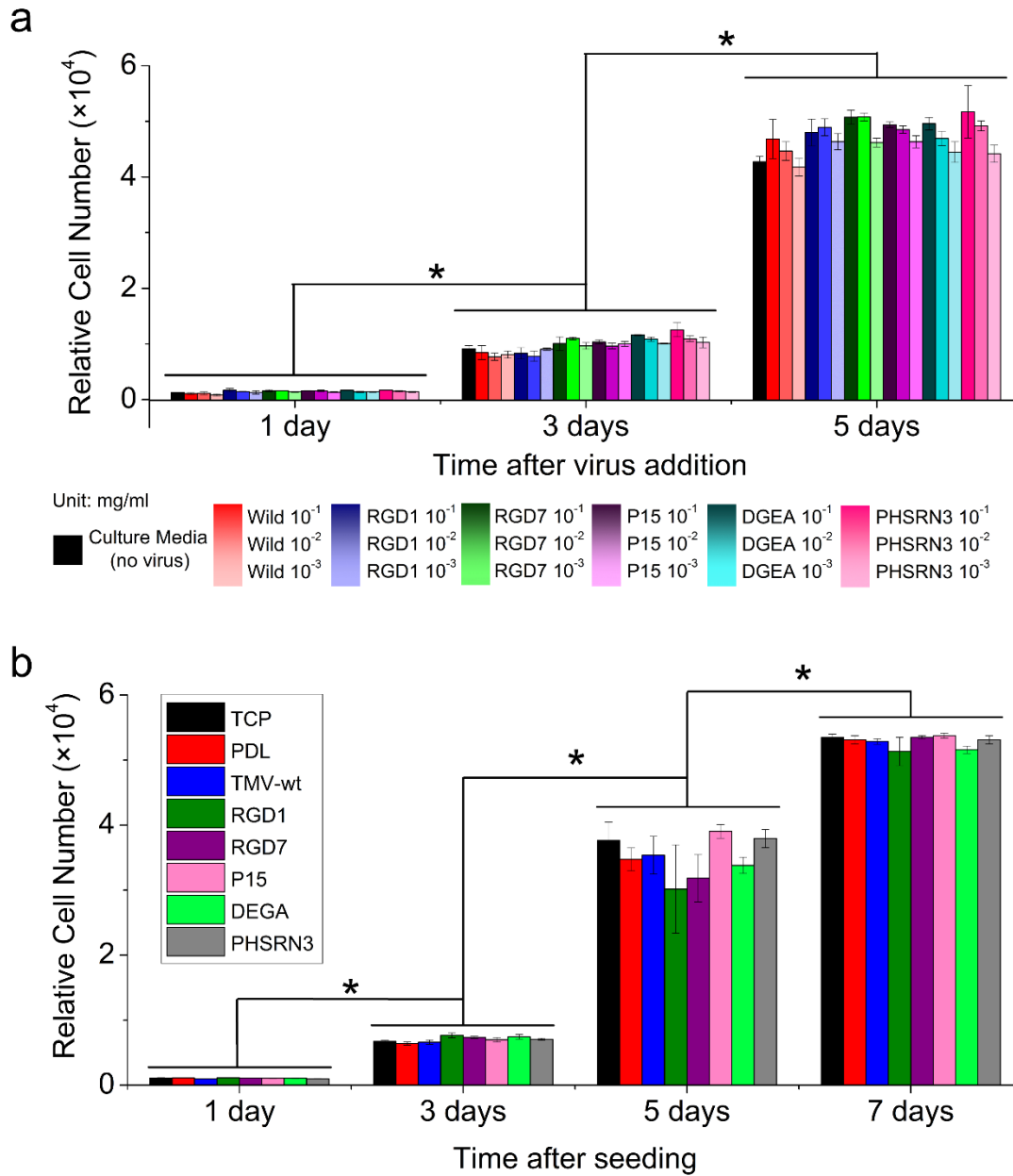
Figure 2.2. Biocompatibility of TMV materials. Cell viability and proliferation with TMV exposure. (a) N2a cells exhibited similar cell numbers regardless of TMV addition to the media at each of the tested time points. Cells exhibited significant proliferation ($P < 0.001$, two-way ANOVA, n = 6) in the presence of each type of TMV mutants during the tested time, same as the positive control (culture media without TMV). (b) N2a cells cultured on various substrates coated by various TMV mutants exhibited similar proliferation rate, same as the control cultured on tissue culture plastics (TCP) and PDL coating substrates proliferation (* $P < 0.001$, two-way ANOVA , n = 6).

2.2.2 Cell Proliferation and Differentiation on TMV mutants

To investigate whether the TMV mutants assist N2a cells adhesion, proliferation, and differentiation, as the coating materials, we culture the N2a cells directly on top of substrates coated with various TMV mutants and compare it to the behaviors of cells on tissue culture plastics. Various virus particles were deposited on poly-D-lysine (PDL) coated 12-well plates. In the PBS at pH 7.4, PDL plates carry positive charge on the surface, where TMV bear negative charge on the surface. Thus, the electrostatic interaction between PDL and TMV drive those virus particles tightly deposit on the surface of 12-well plates. The presence of TMV particles on PDL coated surface was confirmed by atomic force microscopy (AFM) and scanning electron microscopy (SEM) (Figure 2.3). The AFM images suggested that the PDL coated surface were homogeneously and fully covered by TMV particles and most of TMV particles maintain the natural rod-like morphology. Previous study suggests that the resulting nano-scale topography of TMV substrates promoted osteogenic differentiation of rat bone marrow stromal cells.[23-24]
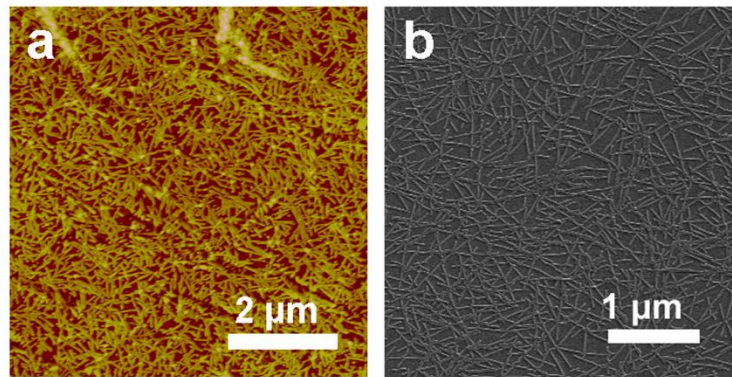
Figure 2.3. Visualization of TMV coating on tissue culture plastics. (a) AFM image of TMV coated tissue culture plastics. Scale bar represents 2 μm. (b) SEM image of TMV coated tissue culture plastics. Scale bar represents 1 μm.

With 2D substrates coated with various TMV particles in hand, we next investigate whether those substrates carrying different cell binding motifs affect the proliferation of N2a cells. When N2a cells were cultured on substrates coated with various TMV particles, we did not observed significant morphological difference. In addition, the CellTiter Blue assay was performed to determine cell proliferation on different substrates. As shown in Figure 2.2b, cells N2a cells grown on substrates coated with RGD1-, RGD7-, PHSRN3-, P15-, DGEA-, and wildtype-TMV showe similar number as the control at predetermined time point. Furthermore, as cells cultured on tissue culture plastics and PDL coated tissue culture plastics, cells on TMV substrates showed significant proliferation over the tested period ($P < 0.001$, two-way ANOVA with replication, n = 6) (Figure 2.2b). This indicates that the various cell binding motifs on TMV substrates did not affect N2a cells proliferation.

It is well known that neuronal cells has the unique feature that they have the tendency to aggregate and form the clusters when being cultured on unpleasant surfaces.[25] Although, N2a cell, a neuroblastoma, is a cancerous cells, it also has this feature, especially, when cells are confluent prior to their re-suspension.[26] In order to determine the efficacy of the TMV mutants as a neural tissue engineering material, we prepared substrates with various TMV mutants, and characterized their effect on cell growth patterns. To quantify the differences observed in the spatial distribution of cells on various virus substrates, we used a nearest neighbor analysis, a method of analyzing spatial relationship for a given population.[27-28] The probability distribution function G(*r*), represents the probability that a given cell will be located a certain distance *r*, away from its neighbor. The distance between cells were determined by measuring the center

coordinates of each cells represented in Figure 2.4. The control cell grown on tissue culture plastics and cell grown on TMV wild type were very similar to clustered distribution. On the contrary, cells grown on substrates coated with TMV mutants were more similar to the theoretically independent distribution. A study by Merzlyak revealed that neural progenitor cells grown on genetically modified M13 phages with cell binding motifs behaves similarly to their counterparts cultured on laminin.[28] Along with other previous works, these results showed that the adhesion and spatial distribution of neural cells highly depend on the type of cell binding ligands on surfaces.[29]

To determine the effect of being cultured on TMV mutants on neuronal differentiation, we cultured N2a cells on various substrates with TMV mutants for 0-48 hours. In the presence of 10% serum, most N2a Cells were remained round undifferentiated status. Most of N2a cells formed neurites after 48 hours being cultured in serum free medium (Figure 2.5). We then quantified the length of neurites with Image J software, and found that the cells cultured on TMV mutants with cell binding motifs significantly increased neurites length compared to cells on TMV wild-type and PDL control group, which are consistent with previous study that cell binding motifs promote neurite outgrowth.[29] One typical example is that RGD promote neurite outgrowth via interaction with the $\alpha_v\beta_3$ integrin.[30] Therefore, the TMV mutants with various cell binding motifs can be used to enhance the extension of neurites.
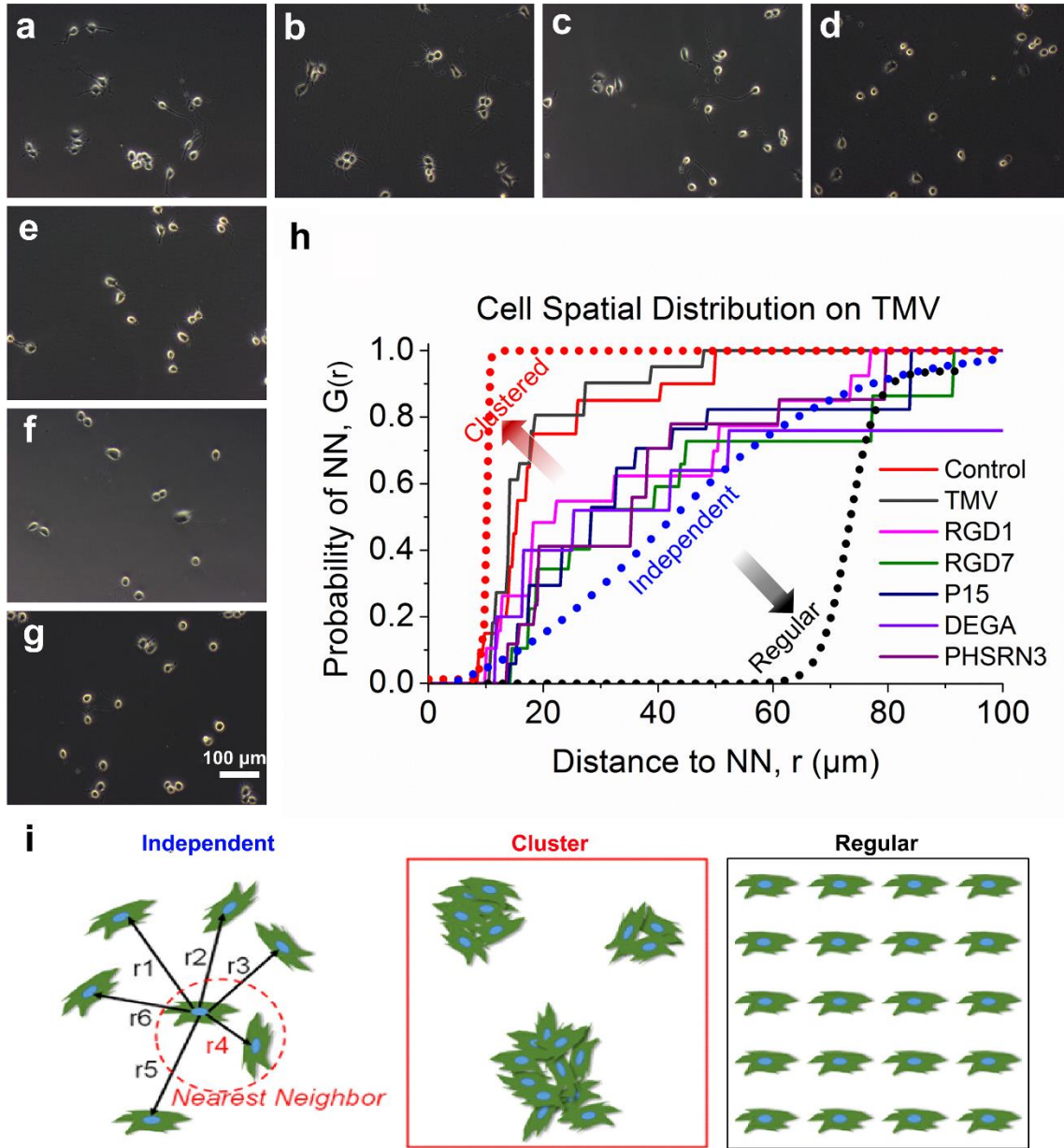
Figure 2.4. Growth patterns of differentiated N2a cells on TMV substrates. SEM images of differentiated N2a cells (24 hours in differentiated media) on TCP (a) and wildtype- (b), RGD1- (c), RGD7- (d), P15- (e), DGEA- (f), PHSRN3-TMV (g) substrates. (a-g) share the scale bar in (g), indicating 100 μm. (h) Plot of cell spatial distribution on TMV substrates. (i) Schematic diagrams of the nearest neighbor analysis.[28] In the analysis the distribution of cells can range from independent (represented by a theoretical Poisson's distribution), to clustered, or regular.
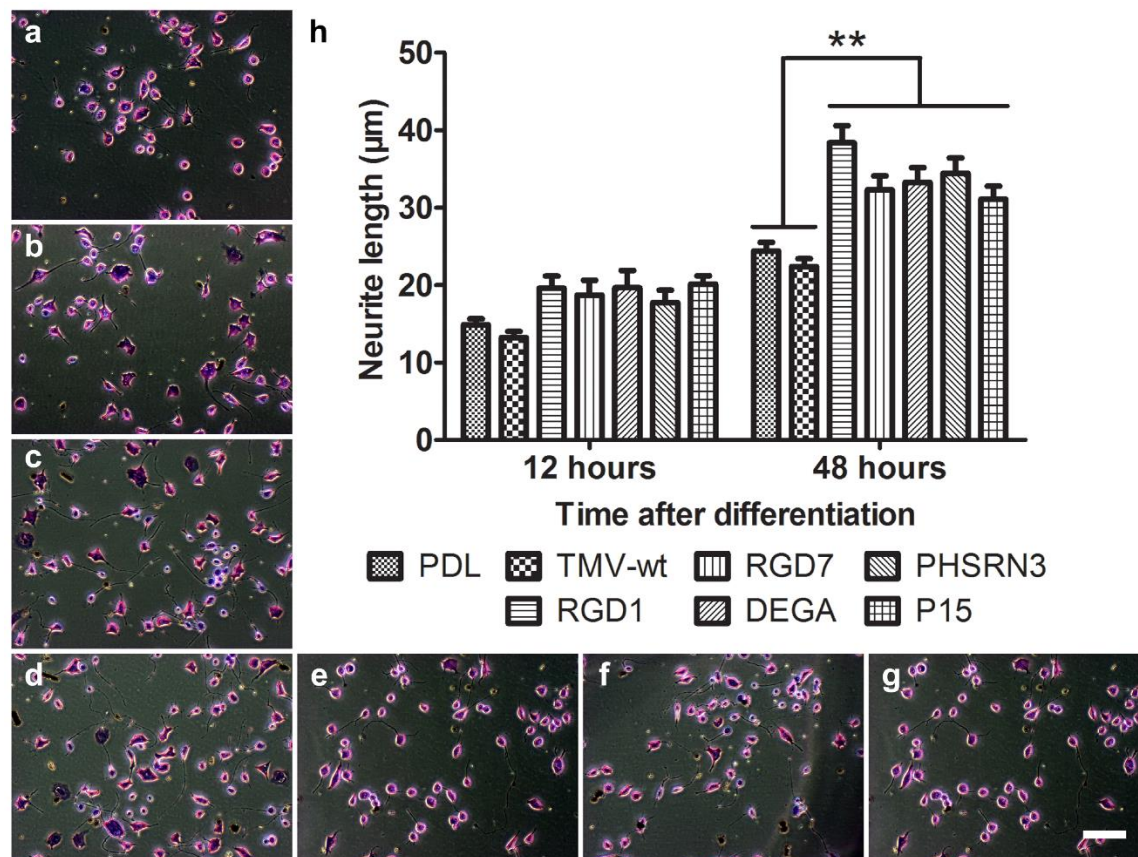
Figure 2.5. Neurite outgrowth of N2a cells on TMV substrates. Images are typical fields of differentiated N2a cells (48 hours in differentiation media) on PDL (a) and wildtype- (b), RGD1- (c), RGD7- (d), P15- (e), DGEA- (f), PHSRN3-TMV (g) substrates. (a-g) share the scale bar in (g), indicating 100 μm. (h) Average neurite length of cells in each group (at least 200 cells were measured). Each data point is the mean $\pm$ SE of three independent experiments. ** indicates $P < 0.001$.

2.2.3 Flow assembly of TMV mutants guide directional outgrowth of neurites

We have developed a robust and facile method for large scale alignment of one dimensional (1D) nanoparticles (NPs), in which 1D NPs are aligned by an aqueous flow. The resulting substrates with aligned TMV and TMV-RGD mutants promoted the differentiation and orientation of myotubes generated by myoblasts (as shown in Chapter 1).[18] Here, we applied this flow assembly method to align genetically modified TMV

mutants with various cell binding motifs. We hypothesized the aligned TMV mutants could induce the directional neurite outgrowth of N2a cells.
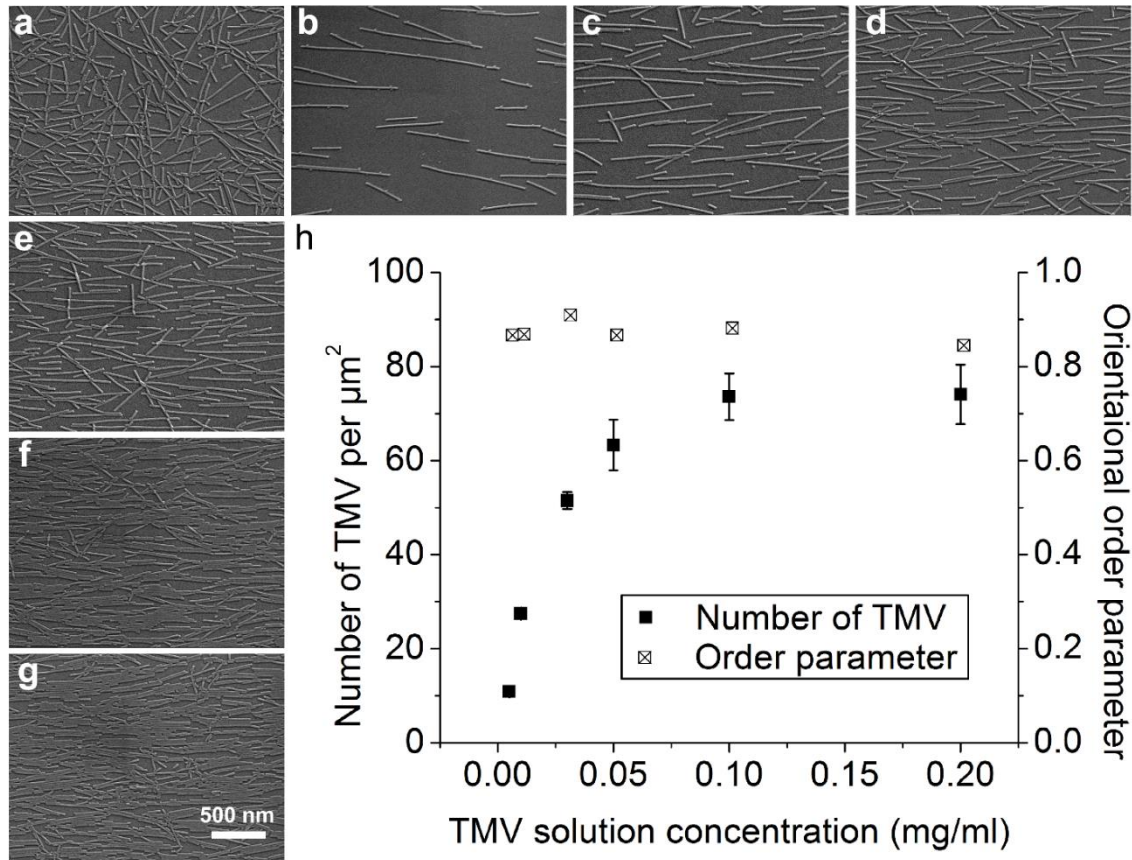
Figure 2.6. Flow assembly of TMV in capillaries in various densities. (a) SEM image of control (*i.e.* 0.05 mg mL^{-1} TMV solution was slowly added in a capillary without applying a fluid flow). SEM images of flow assembly of different concentrations of TMV on chitosan modified capillary tubes at a fixed flow rate of 200 cm s^{-1}: (b) 0.005 mg mL^{-1}, (c) 0.01 mg mL^{-1}, (d) 0.03 mg mL^{-1}, (e) 0.05 mg mL^{-1}, (f) 0.1 mg mL^{-1}, and (g) 0.2 mg mL^{-1}. All SEM images share the scale bar in (g), indicating 500 nm. (h) The dependence of TMV density on assembled solution concentration. Orientation order parameter for all conditions remain above 0.85.

In order to test our hypothesis, we first proceed the flow assembly for TMV wild type using TMV solution (0.005 − 0.2 mg ml^{-1}). SEM images verified that TMV formed the aligned orientation in the inner surface of glass capillaries after flow assembly, which is consistent with previous report. The density of the TMV on the inner surface of the

capillary kept increasing as the solution concentration increased, which has been demonstrated by SEM images (Figure 2.6b-g). The orientation of TMV was further quantitatively assessed by calculating the orientation order parameter ($OP = \frac{1}{2}\langle 3\cos^2\theta - 1\rangle$). OP = 1 means perfectly orientated, and OP = 0 indicates randomly oriented system. The orientation order parameters for each of condition ranged from 0.84 to 0.91 (Figure 2.6h). We then flow assembled other TMV mutants under same a solution concentration (0.02 mg ml^{-1}). The TMV particles were distributed evenly with above 85% surface coverage and an overall alignment along the long axis of the capillary as shown by the AFM images (Figure 2.7). The orientation order parameters for all TMV mutants were between 0.85 and 0.90, indicating aligned nanoparticles were formed.
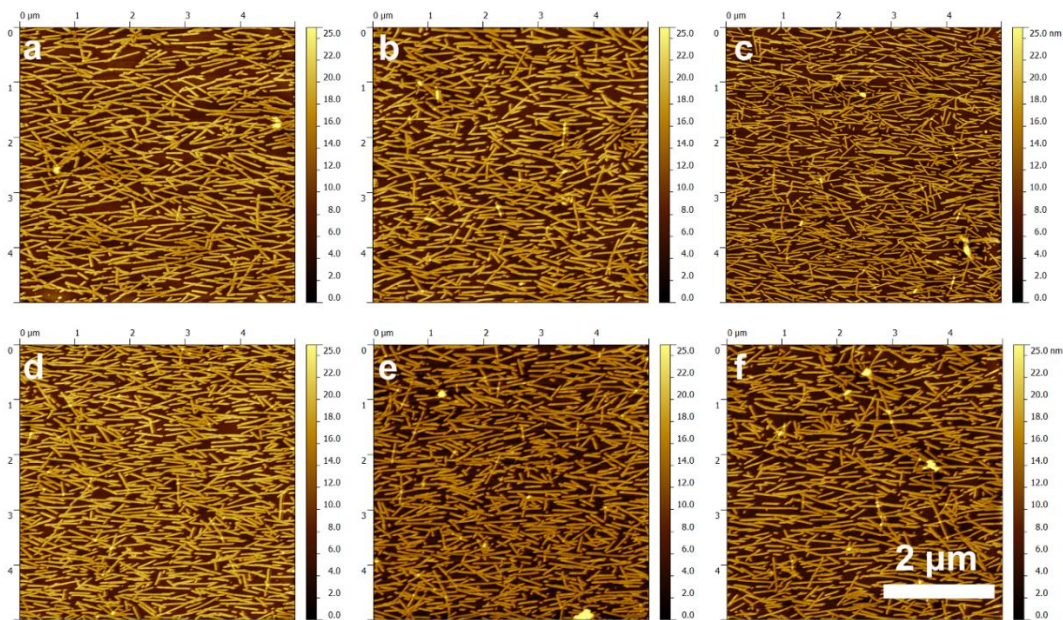
Figure 2.7. AFM images of flow assembly of TMV. (a) TMV, (b) RGD1, (c) RGD7, (d) P15, (e) DGEA, and (f) PHSRN3 were flow assembled in capillaries. All images share the scale bar in (f), indicating 2 μm.

Aligned organization of cells have been observed in various native tissues, such as extracellular matrices,[31] vascular epithelium,[32] striated muscle cells,[33] cardiomyocytes,[34]

47

and neuron cells.[35] Therefore, various techniques, such as mechanical loading, topographical patterning, surface chemical treatment, and electrical stimulation, have been utilized for engineering cells to form aligned organization in tissue engineering.[17] Previous study suggests the topographical cues with desired scale are crucial for nerve regeneration. In order to test our designed capillaries with aligned viruses as a guidance for neurites outgrowth, we seeded N2a cells into the capillaries with aligned viruses. After switch to differentiation media, N2a cells in the capillaries with aligned TMV were able to differentiate and extend neurites in a direction parallel to the long axis of the capillary, which is the flow direction (Figure 2.9b-g and Figure 2.8). The orientation order parameters of neurites for cells on TMV, RGD1, RGD7, P15, DGEA, and PHSRN3 were 0.62, 0.56, 0.45, 0.46, 0.61 and 0.52, respectively (Figure 2.8h). In contrast, the cells on control group, which is absent of NPs, did not show preferred orientation and has an OP = 0.28 (Figure 2.9a and 2.9h). These results indicates that the aligned TMV mutants guided the neurites directional outgrowth and also provide chemical signal to promote neurite extension.
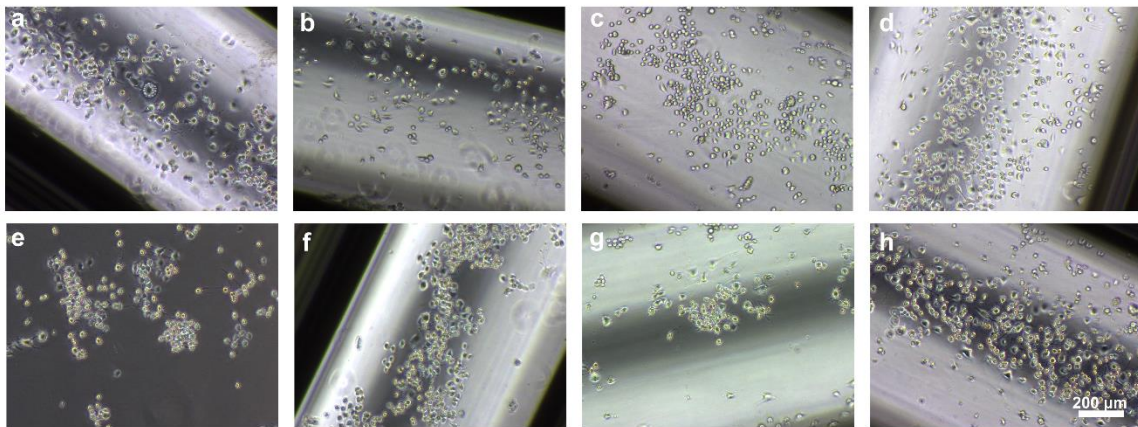
Figure 2.8. N2a cells growth in capillaries with aligned TMV mutants. N2a cells generated neurites in capillaries with flow assembled aligned TMV particles of (b) TMV-wildtype, (c) RGD1, (d) RGD7, (f) P15, (g) DGEA, and (h) PHSRN3. (a) Control group that cells were cultured in capillary without TMV. (e) Cells were cultured on tissue culture plastics. All images share the scale bar in (h), indicating 200 μm.
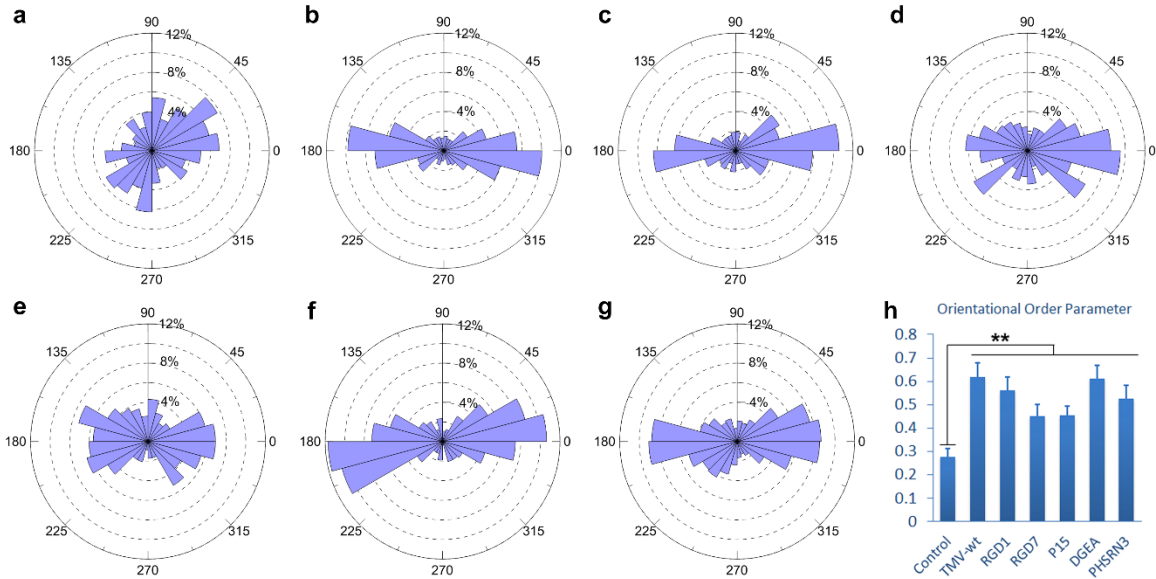
Figure 2.9. Orientation of neurite outgrowth on aligned TMV substrates. Wind rose plot of the neurite orientations on control (no virus) (a) and wildtype- (b), RGD1- (c), RGD7- (d), P15- (e), DGEA- (f), and PHSRN3-TMV (g) substrates. (h) Analysis of neurite alignment using the orientation order parameter (scale from 0 for no alignment to 1 for complete alignment). Each data point is the mean $\pm$ SE of three independent experiments. ** indicates $P < 0.001$.

2.3 CONCLUSIONS

In tissue engineering, understanding the cell-materials interaction is critical for developing specific cell-materials interfaces to control over cellular behaviors. In this chapter, we have tested five genetically modified TMV mutants that carry cell binding motifs of RGD1, RGD7, P15, DGEA, and PHSRN3, for their ability to support neural cells growth and differentiation. The virus particles were non-toxic towards neural cells. In addition, TMV mutants with cell binding motifs significantly improve neurites outgrowth of neural cells compared to TMV wild type and poly-D-lysine coating control. Furthermore, the aligned TMV and TMV mutants by flow assembly provide specific nanotopographical cues to guide directional neurite outgrowth. Given this method can be applied in biodegradable polymer capillaries to provide desired topographical guidance to

49

neural cells, we anticipate the combination of plant virus particles and flow assembly method might provide better nerve conduit for the repair of nerve injuries.

2.4 EXPERIMENTS

2.4.1 Cell Culture

N2a neuroblastoma cells is obtained from American cell type culture collection. Briefly, N2a cells were maintained in Dulbecco's modified Eagle's medium (DMEM, #D6046, Sigma–Aldrich) supplemented with 10% heat inactivated fetal bovine serum (Hyclone, Thermo Scientific), 100 U mL^{-1} penicillin and 100 μg mL^{-1} streptomycin (Gibco BRL, Invitrogen Corp., Carlsbad, CA, USA) in presence of 5% CO2 at 37°C.

2.4.2 Purification of TMV

The TMV, TMV-RGD1, TMV-RGD7, TMV-P15, TMV-DGEA and TMV-PHSRN3 were isolated from the infected leaves according to the reported methods.[11] Briefly, 10 mM potassium phosphate buffer (pH 7.4) with 0.2% β-mercaptoethanol was added into crashed leaves, and centrifuged at 9000 rpm for 15 min. The supernatant was clarified with equal volume of CHCl$_3$ and n-butanol (1:1 ratio). 10% PEG800 and 0.2 M NaCl were added to the aqueous supernatant to precipitate TMV. After the centrifugation, the pellets were resuspended in 10 mM phosphate buffer. Finally, the pure viruses were obtained after the process of ultracentrifugation for 2.5 h at 42 000 rpm (rotor Ti 75).

2.4.3 Cytotoxicity of Viruses to N2a Cells

Various concentrations (from 10^{-1} to 10^{-3} mg mL^{-1}) of genetically modified TMV mutants (displaying RGD1, RGD7, P15, DGEA, and PHSRN3) and wild-type TMV were added to the media. Given that the footprint of the TMV were a 18nm wide and 300 nm

long rectangle, we calculated that each well (0.34 cm^2 surface area) of the 96-well plates used for viability assays could be completely covered by approximately 6×10^9 TMV. This quantity of virus was used to set a median TMV concentration of 10^{-2} mg ml^{-1}, and TMV concentrations that were 10 times greater and 10 times less were tested to determine whether the TMV mutants affected cellular viability. The culture medium containing constant TMV concentration were changed daily for each group. Cell viability was determined by CellTiter-Blue^{TM} Cell Viability Assay (Promega, Madison, WI) at predetermined time points.

2.4.4 Preparation of Cell Culture Substrates

All surfaces used for culturing N2a cells were pre-coated before cell plating. 0.7 ml viruses in aqueous solution (1 mg mL^{-1}) were dropped into 12 well plates that were coated with Poly-d-Lysine using protocol suggested by Corning®. The virus solutions were incubated with the PDL coated plate in sterile cells culture hood for overnight. Then each well was rinsed briefly with 18.2 mΩ water before used for N2a culture.

2.4.5 Surface Characterization of Virus Based Substrates by AFM

The surface morphology of virus based scaffolds was observed by AFM (Nanoscope IIIA MultiMode AFM (Veeco)). The bottoms of each 12 well plate were cut out after virus coating and rinsed with 18.2 mΩ water then dried with a stream of nitrogen gas before mounted onto AFM sample holder for imaging in the tapping mode.

2.4.6 Nearest Neighbor Analysis

Spatial distribution analysis of the cells on various genetically engineered TMV and control surfaces was performed by using ImageJ and R software packages. The images

51

of cell were initially processed with ImageJ to be represented by particles, and their centroid coordinates were determined. This data was then imported into R for nearest neighbor analysis using the SpatStat module.[36]

2.4.7 Quantification of Neurite Outgrowth

To quantify the length of the neurite outgrowth, we stained cells using crystal violet. Briefly, cells cultured on various TMV substrates and control were induced to differentiation by low serum culture medium (1% FBS). Cells were washed in PBS, fixed with ice-cold methanol at -20°C for 15 min. and then stained with 0.5% crystal violet solution in methanol for 30 min at room temperature. Using an inverted light microscope, we took the images and quantified the length of neurites by ImageJ. Five random fields were examined from each well, giving a total cell count of at least 200 cells per well. Each data point represents the mean of three independent experiments.

2.4.8 Flow Assembly of TMV

Flow assembly of various viruses for cell culture were performed as previously described.[18] Briefly, the chitosan coated capillaries were obtained by immersing into chitosan (1 mg mL^{-1} in 0.1% acetic acid at pH=6.5). Water was used to wash before using. 10 mL solution containing 1 D NPs was injected into the 1D NPs feeder, which one end was connected to nitrogen tank and the other end was connected to capillary tube. The solution was driven through the capillary tube, and dried by the following gas. The flow rate of solution was controlled by the gas pressure applied to the flow.

2.4.9 Characterization of TMV and TMV Coated Substrates

TMV solution was dropped on the glow-discharged Formvar-carbon coated copper grid. After drying, the sample was negatively stained with 2% uranyl acetate for TEM (Philips CM-12 transmission electron microscope at 80 kEV) observation. The surface morphology was observed by AFM (SPA300, Seiko) in the tapping mode. The angles of 1D NPs were measured with ImageJ software and then calculated for the orientation order parameter ($OP = \frac{1}{2}\langle 3\cos^2\theta - 1\rangle$).

2.4.10 Directional Neurite Outgrowth in Capillaries with TMV

N2a cells were trypsinized and then seeded in the capillaries with aligned viruses. After 24 hours, cells were switched into differentiation medium. After 48 hours differentiation, samples were observed under microscopy. The angles of neurites were measured with ImageJ software and angular distribution were then plotted in a circular histogram and calculated for the orientation order parameter ($OP = \frac{1}{2}\langle 3\cos^2\theta - 1\rangle$). For each of the group, at least 300 neurites were measured from three independent experiments.

2.5 REFERENCE

1.   Langer, R.; Vacanti, J. P. Tissue engineering. *Science* **1993,** *260* (5110), 920-6.

2.   Watt, F. M.; Huck, W. T. S. Role of the extracellular matrix in regulating stem cell fate. *Nat Rev Mol Cell Bio* **2013,** *14* (8), 467-73.

3.   Feng, S.; Duan, X.; Lo, P. K.; Liu, S.; Liu, X.; Chen, H.; Wang, Q. Expansion of breast cancer stem cells with fibrous scaffolds. *Integr Biol (Camb)* **2013,** *5* (5), 768-77.

4.   Geckil, H.; Xu, F.; Zhang, X. H.; Moon, S.; Demirci, U. Engineering hydrogels as extracellular matrix mimics. *Nanomedicine-Uk* **2010,** *5* (3), 469-84.

5.   Zhang, S.; Gelain, F.; Zhao, X. Designer self-assembling peptide nanofiber scaffolds for 3D tissue cell cultures. *Semin Cancer Biol* **2005,** *15* (5), 413-20.

6.   Lee, L. A.; Nguyen, H. G.; Wang, Q. Altering the landscape of viruses and bionanoparticles. *Org Biomol Chem* **2011,** *9* (18), 6189-95.

7.   McCormick, A. A.; Palmer, K. E. Genetically engineered Tobacco mosaic virus as nanoparticle vaccines. *Expert Rev Vaccines* **2008,** *7* (1), 33-41.

8.   Sitasuwan, P.; Lee, L. A.; Li, K.; Nguyen, H. G.; Wang, Q. RGD-conjugated rod-like viral nanoparticles on 2D scaffold improve bone differentiation of mesenchymal stem cells. *Front Chem* **2014,** *2*, 31.

9.   Suthiwangcharoen, N.; Li, T.; Li, K.; Thompson, P.; You, S. J.; Wang, Q. M13 Bacteriophage-Polymer Nanoassemblies as Drug Delivery Vehicles. *Nano Res* **2011,** *4* (5), 483-93.

10.   Klug, A. The tobacco mosaic virus particle: structure and assembly. *Philos Trans R Soc Lond B Biol Sci* **1999,** *354* (1383), 531-5.

11. Lee, L. A.; Nguyen, Q. L.; Wu, L.; Horvath, G.; Nelson, R. S.; Wang, Q. Mutant plant viruses with cell binding motifs provide differential adhesion strengths and morphologies. *Biomacromolecules* **2012,** *13* (2), 422-31.

12. Schmidt, C. E.; Leach, J. B. NEURALTISSUEENGINEERING: Strategies for Repair and Regeneration. *Annual Review of Biomedical Engineering* **2003,** *5* (1), 293-347.

13. Kehoe, S.; Zhang, X. F.; Boyd, D. FDA approved guidance conduits and wraps for peripheral nerve injury: A review of materials and efficacy. *Injury* **2012,** *43* (5), 553-72.

14. Spivey, E. C.; Khaing, Z. Z.; Shear, J. B.; Schmidt, C. E. The fundamental role of subcellular topography in peripheral nerve repair therapies. *Biomaterials* **2012,** *33* (17), 4264-76.

15. Yim, E. K.; Reano, R. M.; Pang, S. W.; Yee, A. F.; Chen, C. S.; Leong, K. W. Nanopattern-induced changes in morphology and motility of smooth muscle cells. *Biomaterials* **2005,** *26* (26), 5405-13.

16. Hu, J.; Hardy, C.; Chen, C. M.; Yang, S.; Voloshin, A. S.; Liu, Y. L. Enhanced Cell Adhesion and Alignment on Micro-Wavy Patterned Surfaces. *PLoS One* **2014,** *9* (8).

17. Li, Y.; Huang, G.; Zhang, X.; Wang, L.; Du, Y.; Lu, T. J.; Xu, F. Engineering cell alignment in vitro. *Biotechnology Advances* **2014,** *32* (2), 347-65.

18. Zan, X.; Feng, S.; Balizan, E.; Lin, Y.; Wang, Q. Facile method for large scale alignment of one dimensional nanoparticles and control over myoblast orientation and differentiation. *ACS Nano* **2013,** *7* (10), 8385-96.

19. Shakhova, O.; Sommer, L. Neural crest-derived stem cells. In: StemBook [Internet]. Cambridge (MA): Harvard Stem Cell Institute; **2010**.

20.   Tremblay, R. G.; Sikorska, M.; Sandhu, J. K.; Lanthier, P.; Ribecco-Lutkiewicz, M.; Bani-Yaghoub, M. Differentiation of mouse Neuro 2A cells into dopamine neurons. *J Neurosci Meth* **2010,** *186* (1), 60-7.

21.   Wang, X.; Meng, D.; Chang, Q.; Pan, J.; Zhang, Z.; Chen, G.; Ke, Z.; Luo, J.; Shi, X. Arsenic inhibits neurite outgrowth by inhibiting the LKB1-AMPK signaling pathway. *Environ Health Perspect* **2010,** *118* (5), 627-34.

22.   Bronisz, A.; Gajkowska, B.; Domanska-Janik, K. PKC and Raf-1 inhibition-related apoptotic signalling in N2a cells. *J Neurochem* **2002,** *81* (6), 1176-84.

23.   Kaur, G.; Valarmathi, M. T.; Potts, J. D.; Jabbari, E.; Sabo-Attwood, T.; Wang, Q. Regulation of osteogenic differentiation of rat bone marrow stromal cells on 2D nanorod substrates. *Biomaterials* **2010,** *31* (7), 1732-41.

24.   Kaur, G.; Wang, C.; Sun, J.; Wang, Q. The synergistic effects of multivalent ligand display and nanotopography on osteogenic differentiation of rat bone marrow stem cells. *Biomaterials* **2010,** *31* (22), 5813-24.

25.   Saha, K.; Irwin, E. F.; Kozhukh, J.; Schaffer, D. V.; Healy, K. E. Biomimetic interfacial interpenetrating polymer networks control neural stem cell behavior. *Journal of Biomedical Materials Research Part A* **2007,** *81A* (1), 240-9.

26.   Kadmon, G.; Imhof, B. A.; Altevogt, P.; Schachner, M. Adhesive hierarchy involving the cell adhesion molecules L1, CD24, and alpha 6 integrin in murine neuroblastoma N2A cells. *Biochem Biophys Res Commun* **1995,** *214* (1), 94-101.

27.   Campbell, D. J.; Clarke, D. J. Nearest Neighbor Tests of Significance for Non-Randomness in Spatial-Distribution of Singing Crickets (Teleogryllus-Commodus (Walker). *Anim Behav* **1971,** *19* (4), 750-6.

28.   Merzlyak, A.; Indrakanti, S.; Lee, S. W. Genetically engineered nanofiber-like viruses for tissue regenerating materials. *Nano Lett* **2009,** *9* (2), 846-52.

29.   Cooke, M. J.; Zahir, T.; Phillips, S. R.; Shah, D. S. H.; Athey, D.; Lakey, J. H.; Shoichet, M. S.; Przyborski, S. A. Neural differentiation regulated by biomimetic surfaces presenting motifs of extracellular matrix proteins. *Journal of Biomedical Materials Research Part A* **2010,** *93A* (3), 824-32.

30.   Yip, P. M.; Zhao, X. N.; Montgomery, A. M. P.; Siu, C. H. The Arg-Gly-Asp motif in the cell adhesion molecule L1 promotes neurite outgrowth via interaction with alpha(v)beta(3) integrin. *Mol Biol Cell* **1998,** *9* (2), 277-90.

31.   Whitby, D. J.; Ferguson, M. W. J. The Extracellular-Matrix of Lip Wounds in Fetal, Neonatal and Adult Mice. *Development* **1991,** *112* (2), 651-68.

32.   Kissa, K.; Herbomel, P. Blood stem cells emerge from aortic endothelium by a novel type of cell transition. *Nature* **2010,** *464* (7285), 112-5.

33.   Gokhin, D. S.; Fowler, V. M. A two-segment model for thin filament architecture in skeletal muscle. *Nat Rev Mol Cell Biol* **2013,** *14* (2), 113-9.

34.   Kim, D. H.; Lipke, E. A.; Kim, P.; Cheong, R.; Thompson, S.; Delannoy, M.; Suh, K. Y.; Tung, L.; Levchenko, A. Nanoscale cues regulate the structure and function of macroscopic cardiac tissue constructs. *Proceedings of the National Academy of Sciences* **2009,** *107* (2), 565-70.

35.   Pacary, E.; Martynoga, B.; Guillemot, F. Crucial first steps: the transcriptional control of neuron delamination. *Neuron* **2012,** *74* (2), 209-11.

36.   Baddeley, A.; Turner, R. Spatstat: An R Package for Analyzing Spatial Point Patterns. *Journal of Statistical Software* **2005,** *12* (6), 1-42.

57

CHAPTER 3

EXPANSION OF BREAST CANCER STEM CELLS WITH FIBROUS SCAFFOLDS

Portions of this chapter appear in the following manuscript: expansion of breast cancer stem cells with fibrous scaffolds.[1]

3.1 INTRODUCTION

Cells cultured *in vitro* two dimensional (2D) tissue culture plastics (TCP) lack of the structural architecture necessary for proper cell-cell and cell-matrix interactions that exists *in vivo*.[2-4] The complexity of the *in vivo* system, being composed of many uncontrollable factors, such as immune response, endogenous growth factors, hemodynamics and mechanical cues, complicates researches on effects of individual factor on cell behaviours. On the other hand, although rodent animal models are relative reliable system for human cancer research and have been used for several decades,[5-8] the significant difference in telomerase regulation between humans and rodents makes transgenic and inducible mouse cancer model questionable in term of replicating the human cancers.[9] Hence, three-dimensional (3D) cell culture models emerged to bridge the gap between *in vivo* human cancer studies and *in vitro* 2D cell culture models, as well as animal models.

The fabrications of 3D scaffolds for the study of tumor cells *in vitro* have adopted techniques from developed fields of tissue engineering.[2, 10-11] Among those techniques, the electrospinning process is a simple and rapid method to generate scaffolds with fibers range from micrometer to nanometer in diameter.[12] Although cells in electrospun fibrous scaffolds often adhere on the surface with minimum penetration, researchers consider these

scaffolds as a 3D-like culture system because cells are able to acquire the nutrition and extracellular signal three dimensionally.[13] Among various natural and synthetic polymers available for electrospinning process, poly(ε-caprolactone) (PCL) have attracted interests of researchers due to low melting temperature, good blend-compatibility, FDA approval, and low cost.[14] Nano and micro scale fibrous scaffolds by electrospinning are ideal for 3D cells culture, because their structures are similar to components in extracellular matrix, providing essential cues for cellular survival, proliferation, organization, and function.[13]

Tumor cells grown in 3D scaffolds tend to develop the morphologies and phenotypes observed *in vivo*[15-17] and displayed higher invasive capability, and increased drug resistance relative to cells in a 2D culture condition.[18-19] However, the mechanism of those alterations is still unclear. Recent researches revealed extracellular matrix (ECM) proteins can be either coated in 2D dishes or fabricate into 3D scaffolds for the enhancement and maintenance of the stemness properties of cancer cells.[20-21]

Cancer stem cells (CSCs) are rare subpopulations that have the capability to initiate tumor growth. Recent researches reveal that CSCs are responsible for metastasis,[22] chemo-resistance,[23] and radio-resistance.[24] In the present study, we hypothesized that the electrospun PCL fibrous scaffolds itself without any protein component can increase CSCs population. Using aldehyde dehydrogenase (ALDH) activity as a CSCs marker[25] and mammosphere formation assay,[26] we found that MCF-7, T47D, SK-BR-3 and MDA-MB-231 cells cultured in electrospun PCL fibrous scaffolds increased the CSCs population. The enhanced invasiveness and upregulation of epithelial-to-mesenchymal transition (EMT) markers indicates cells were undergoing EMT, which might trigger the transformation of non-stem cancer cells to CSCs.[27]

59

3.2 RESULTS AND DISCUSSION

3.2.1 Fabrication of Electrospun PCL Fibrous Scaffolds

PCL fibrous scaffolds were fabricated using a home-made electrospinning apparatus. For electrospun scaffolds to be reproduced, the important parameters of electrospinning were recorded and illustrated (Figure 3.1a). With a stationary collector placed at 10 cm underneath the tip, random fibrous scaffolds were obtained, and no preferred fiber orientation was observed under scanning electron microscope (SEM) (Figure 3.1b). The average fiber diameter calculated by Image J software was 1.63 ± 0.36 μm and the diameter distribution of this PCL scaffolds ranged from 0.76 to 2.35 μm (Figure 3.1c).
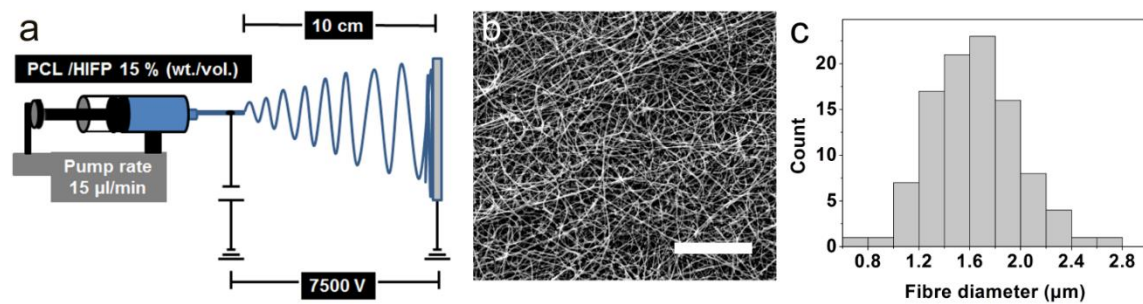
Figure 3.1. PCL fibrous scaffolds were fabricated by the electrospinning process. (a) The electrospinning setup was illustrated schematically. (b) The SEM image of the electrospun PCL fibrous scaffold. Scale bar indicates 100 μm. (c) The distribution of the fiber diameter on PCL fibrous scaffolds fabricated in the described setting.

Although in diseases or during the movement, the ECM will be reorganized in aligned orientation, the major component of ECM, collagen fibers, usually randomly surrounded the breast epithelial cells,[28] which is similar to the organization of the electrospun PCL random fibrous scaffolds. Our lab found that luminal-type cell line MCF-7 maintained cell-cell contact and random orientation on aligned fibrous scaffolds, indicating less impacts of the aligned fibers on the cells.[29] The aligned fiber orientation will

introduce the mechanical stretch on the cells, which might complicate the interpretation of results. Therefore, in this study we use random orientation fibrous scaffolds for cell culture.

3.2.2 Cellular Morphology and Growth on Electrospun PCL 3D Scaffolds

MCF-7 cells successfully propagated on PCL fibrous scaffolds. Fluorescence microscopy revealed different morphologies between MCF-7 cells cultured on electrospun PCL fibrous scaffolds and TCP (Figure 3.2). Cells on TCP exhibited trigonal or polygonal morphologies, whereas cells on PCL fibrous scaffolds showed round shuttle-like shape. We also observed similar results in T47D, SK-BR-3, and MDA-MB-231 cells (Figure 3.3). Relative to cells on TCP with a spreading-out morphology, cells on PCL fibrous scaffolds displayed smaller F-actin staining area and round-like shape. This is might be due to that fibers surrounding cells limited cells spreading and cells increased the thickness (Figure 3.4).
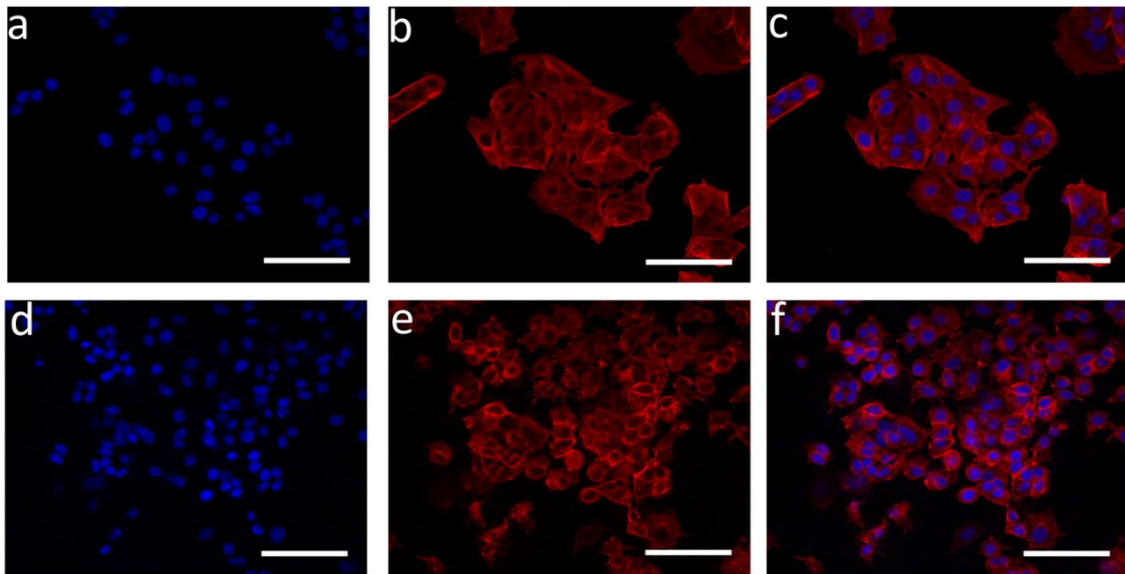
Figure 3.2. Fluorescence microscopy images of MCF-7 cells cultured in 2D tissue culture plastics. (a-c) and 3D PCL fibrous scaffolds (d-f). Blue indicates nuclei (DAPI); red indicates F-actin (Rhodamine-Phalloidin). All scale bars indicate 100 μm.
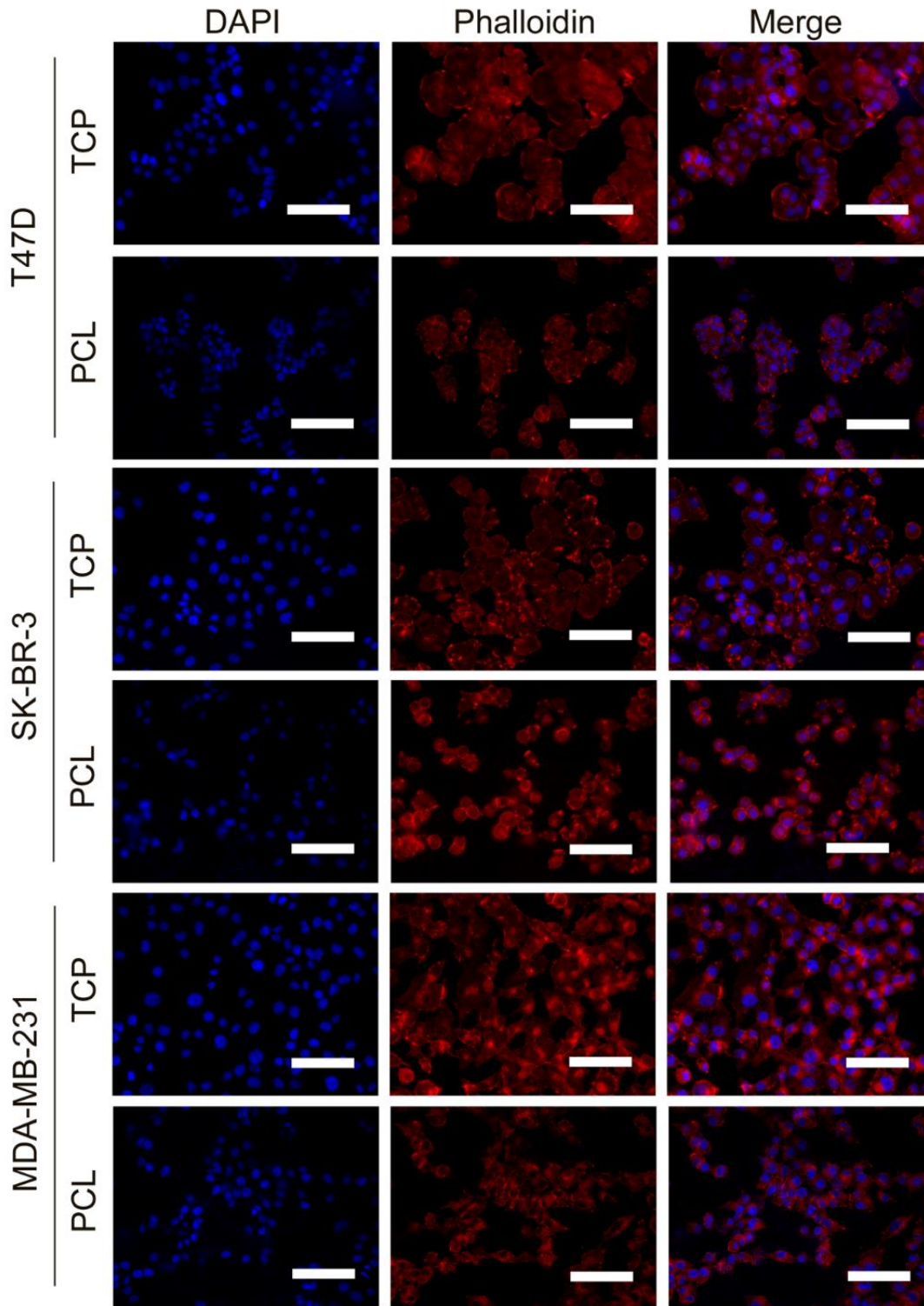
Figure 3.3. Fluorescence microscopy images of T47D, SK-BR-3, and MDA-MB-231 cells cultured in 2D tissue culture plastics and 3D PCL fibrous scaffolds . Blue indicates nuclei (DAPI); red indicates F-actin (Rhodamine-Phalloidin). All scale bars indicate 100 μm.
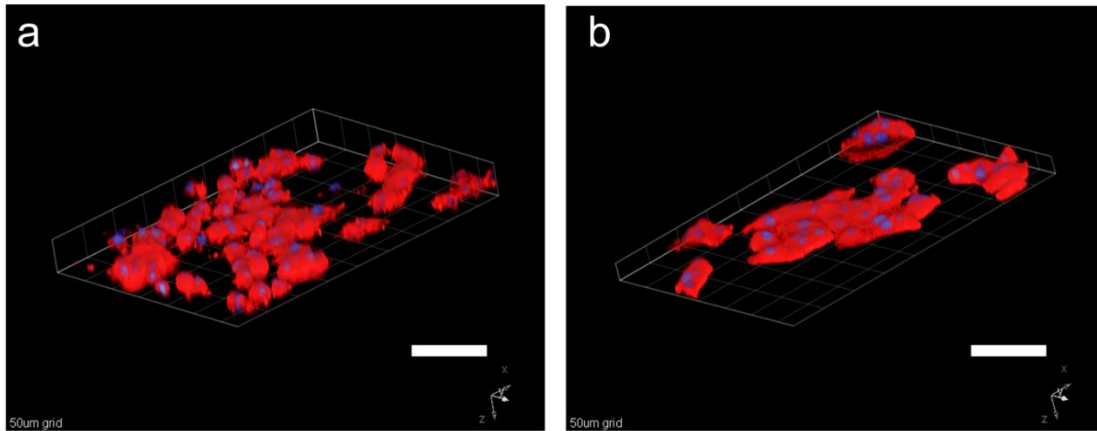
Figure 3.4. MCF-7 cells seeded in PCL fibrous scaffold occupied architectural features of the matrix in three dimensions as observed using confocal microscope. 3D reconstruction of sequential strata demonstrated MCF-7 occupation of sub-surface niches within the PCL scaffold. Serial z-plane sampling was conducted for total z-scan distance of 45 μm at 3 μm per plane for cells in PCL scaffolds (a) and 20 μm at 3 μm per plane for cells on TCP (b) . Blue indicates nuclei (DAPI); red indicates F-actin (Rhodamine-Phalloidin). All scale bars indicate 100 μm.

We utilized CellTiter-Blue assay measured cell growth on PCL scaffolds. On day 7, MCF-7 cells on TCP and fibrous scaffolds proliferated to 15.00 ± 0.48-fold and 13.87 ± 0.56-fold relative to day 1, respectively. There was no statistically significant difference in proliferation rate between cells on TCP and PCL fibrous scaffolds during the first 7 days. However, on day 9, cells cultured on TCP reached plateau, whereas cells on PCL fibrous scaffolds continue propagating to 17.58 ± 1.43-fold relative to day 1 (Figure 3.5). Considering the seeding cell densities were the same in these two culture systems, the discrepancy might come from the expanding space for cell growth in 3D PCL fibrous scaffolds. We also observed similar trends in MDA-MB-231 cells (Figure 3.6).

63
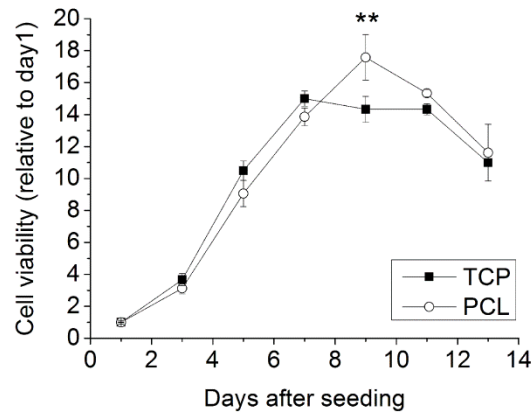
Figure 3.5. The proliferations of MCF-7 in 2D tissue culture plastics and 3D PCL scaffolds were measured at indicated time points by CellTiter-Blue assay. Results were shown as mean ±standard deviation. Statistical significance of the differences between cells on TCP and PCL is indicated by two asterisks (P < 0.005, n = 3).
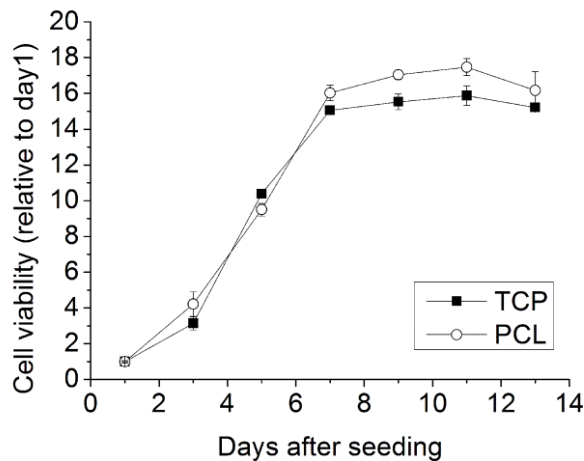
Figure 3.6. The proliferations of MDA-MB-231 in 2D tissue culture plastics and 3D PCL fibrous scaffolds. Results were shown as mean ±standard deviation. Statistical significance of the differences between cells in TCP and PCL is indicated by two asterisks (P < 0.005, n = 3).

3.2.3 Culturing MCF-7 cells on PCL Fibrous Scaffolds Induces the Expansion of CSCs

The CSC theory postulates that a small group of cells, which is selected by specific combination of markers, are responsible for the initiation and maintenance of tumors. Chen and his colleagues found that MCF-7 cells in 3D collagen scaffolds displayed enhanced

64

stemness relative to counterparts in 2D culture.[21] The collagen scaffolds provides not only a 3D culture scaffold, but also a microenvironment with protein-protein interactions between membrane proteins of MCF-7 cells and collagen. In this study, the unmodified electrospun PCL scaffolds excludes the protein-protein interaction between cells and scaffolds. We cultured MCF-7 cells on PCL fibrous scaffolds to test how this fibrous scaffolds culture condition affects the size of CSCs population.

Aldehyde dehydrogenase, which is a detoxifying enzyme responsible for the oxidation of intracellular aldehyde, may play a role in early differentiation of stem cells through its role in oxidizing retinol to retinoic acid.[30] Accumulating data indicates that ALDH expression is related to cells with enhanced tumorigenic and metastatic potential.[31-33] In addition, based on ALDH activity, Ginestier and colleagues successfully isolated CSCs from human breast tumors, and the expression of ALDH1 was considered as a predictor of clinical outcomes in breast cancer patients.[25] We utilized the ALDEFLUOR assay to assess the proportion of CSCs in breast cancer cells from PCL fibrous scaffolds and TCP respectively.[34] The ratio of ALDH-positive population of MCF-7 cells increased to 6.33% $\pm 0.55\%$ in 3D PCL scaffolds relative to 2.00% $\pm 0.04\%$ in 2D TCP after 6 days culture without passage (Figure 3.7a and d). We also assessed CSCs in another two luminal-type cell lines, T47D and SK-BR-3, from PCL fibrous scaffolds and TCP. The proportion of ALDH-positive cells in T47D and SK-BR-3 increased to 6.80% $\pm 0.58\%$ and 18.27% $\pm 1.73\%$ on PCL fibrous scaffolds from 1.82% $\pm 0.74\%$ and 7.22% $\pm 0.19\%$ on TCP, respectively (Figure 3.7).
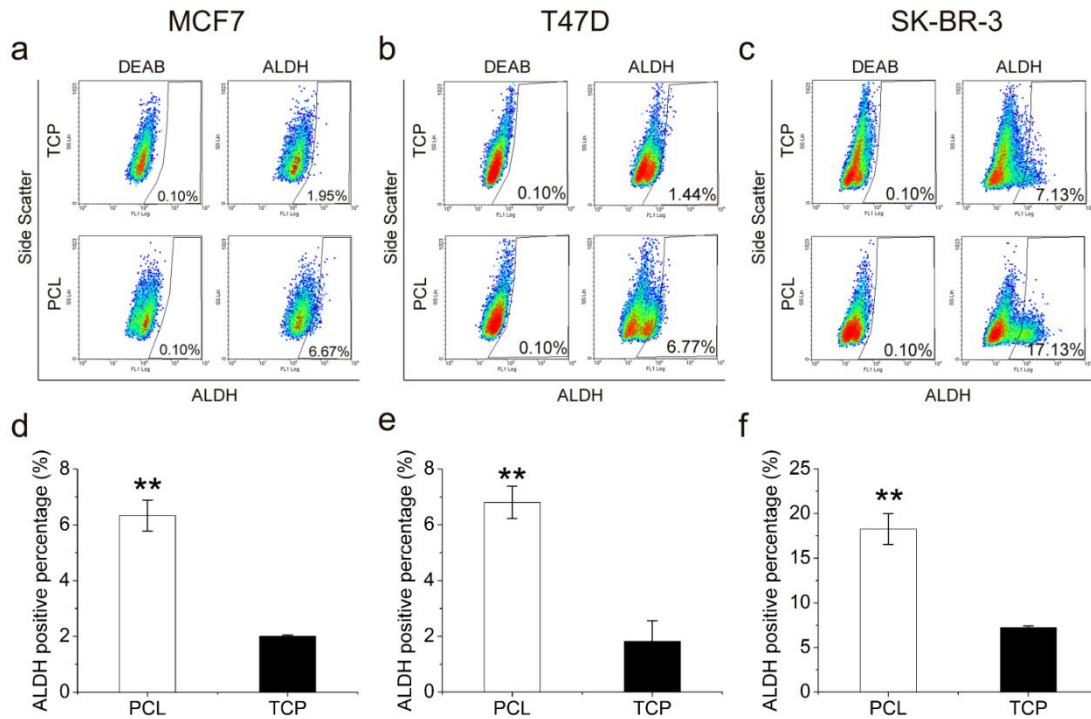
Figure 3.7. Epithelial breast cancer cell lines, MCF-7, T47D, and SK-BR-3 cultured on PCL fibrous scaffolds increased ALDH-positive population compared with counterparts cultured on TCP. (a-c) After being cultured 6 day on PCL and TCP without passage, cells were harvested and analyzed by ALDEFLUOR assay. The ALDH inhibitor, diethylaminobenzaldehyde (DEAB) (15 μM), was added to the cell suspension in ALDEFLUOR assay buffer with the substrate as a negative control. Numbers indicate percentage of cells in the gated area. (d-f) The percentage of ALDH-positive cells in MCF-7, T47D, and SK-BR-3 cells cultured on PCL and TCP. Results were shown as mean ± standard deviation. Statistical significance is indicated by double asterisks (P < 0.001, n=3).

Previous research reported that mammary epithelial stem and progenitor cells can survive and propagate in an attachment-independent manner and form floating spherical colonies, which is termed mammospheres.[26] Therefore the mammosphere formation assay is often used to identify and enrich CSCs. To further confirm whether the PCL fibrous scaffolds culture system increases the size of CSCs population, we measured the mammosphere formation ability of MCF-7 cells from TCP and PCL fibrous scaffolds. We found the MCF-7 cells from PCL fibrous scaffolds formed approximately 2.0-fold more mammospheres than control cells from TCP (Figure 3.8a). The sphere formation efficiency

of T47D and SK-BR-3 from PCL fibrous scaffolds increased to 1.81% ±1.07% and 3.44% ± 0.42%, relative to 1.07% ± 0.50% and 2.51% ± 0.16% for cells on TCP, respectively (Figure 3.8b-c). Some of those spheres have a large size of around 100 μm. These spheres probably came from multiple cells fusion.[35-36] Those data suggests that CSCs expanded in those mammary cancer cell lines when cultured in electrospun PCL fibrous scaffolds.
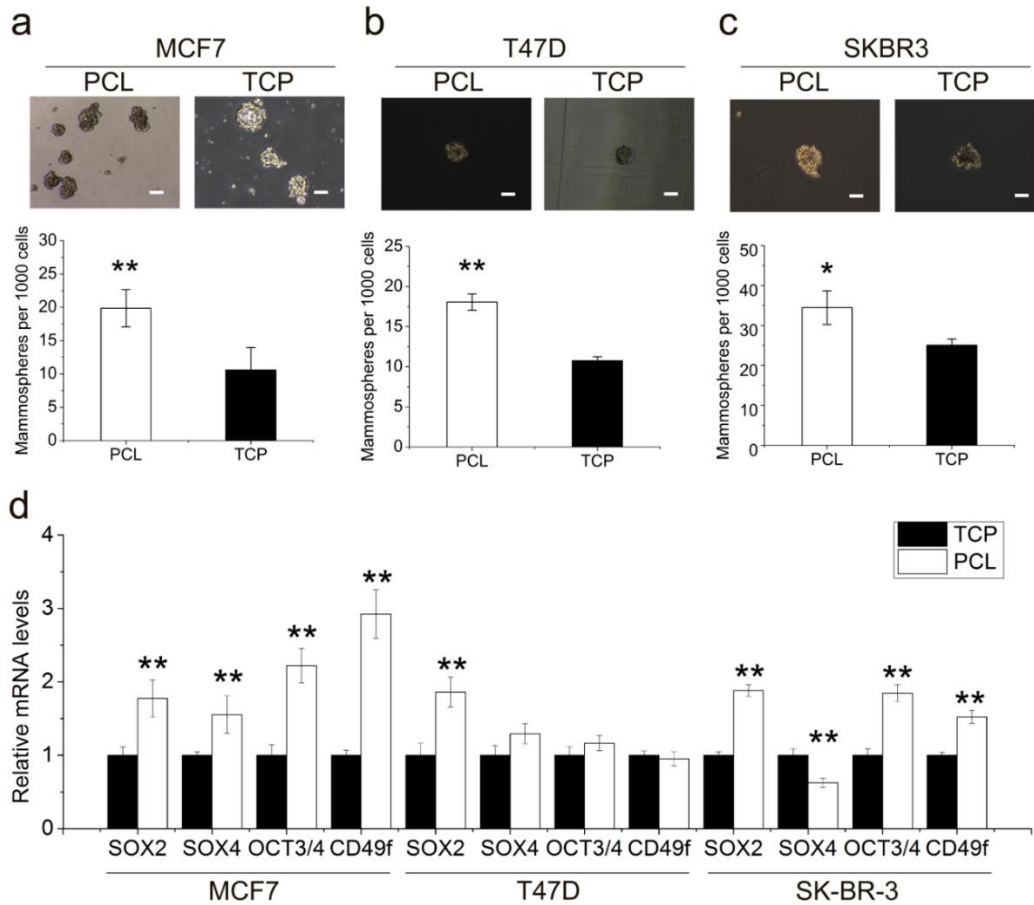
Figure 3.8. Epithelial breast cancer cell lines, MCF7, T47D, and SK-BR-3 on PCL fibrous scaffolds increased the property of stemness. (a-c) Cells cultured on PCL and TCP for 6 days without passage were harvested for mammoshpere formation assay. Mammospheres were observed under microscopy and enumerated. Results were shown as mean ± standard deviation. Statistical significance is indicated by single asterisk ($P < 0.05$, n = 6) or double asterisks ($P < 0.005$, n = 6). Scale bars indicate 100 μm. (d) SOX2, SOX4, OCT3/4, and CD49f expression in MCF-7, T47D, and SK-BR-3 cultured on PCL and TCP. Results were shown as mean ± standard deviation. Statistical significance is indicated by single asterisk ($P < 0.05$, n = 3) or double asterisks ($P < 0.005$, n = 3).

OCT3/4 and SOX2 function cooperatively to regulate their own transcription and the transcription of a large set of other genes, which control the self-renewal and pluripotency of stem cells.[37] SOX4 functions in the progression of breast cancer by orchestrating EMT.[38] CD49f have been used for enrichment of normal and CSCs,[39-40] which maintains the pluripotency and stemness through the direct regulation of OCT4 and SOX2.[41] In our study, transcriptional factors related to stem cells, including SOX2 and OCT3/4, and breast CSC signatures, including SOX4 and CD49f, were enhanced in MCF-7 cultured on fibrous scaffolds by 1.77 ± 0.25-fold, 2.22 ± 0.23-fold, 1.56 ± 0.25-fold, and 2.92 ± 0.33-fold, respectively, relative to cells on TCP (Figure 3.8a). In addition, among stemness related genes, only SOX2 were upregulated in T47D from PCL fibrous scaffolds, while OCT3/4, SOX2, and CD49f were upregulated in SK-BR-3 cells from PCL fibrous scaffolds, relative to cells from TCP (Figure 3.8b).

To investigate whether the effect of 3D PCL fibrous scaffolds culture on CSCs expansion is cell-phenotype specific, we examined how CSCs response to the fibrous scaffolds culture in high malignant basal-type cell line, MDA-MB-231 cells. ALDEFLUOR assay, mammosphere formation assay, and gene expression pattern all show that MDA-MB-231 cells on PCL fibrous scaffolds increased CSCs population relative to cells on TCP (Figure 3.9). Although the proportion of CSCs in MDA-MB-231 cells cultured on PCL fibrous scaffolds increases not as dramatically as in epithelial cell lines, the same trend of changes in the CSC population in several breast cancer cell lines cultured indicates that this phenomenon is not cell- phenotype specific.

Studies have demonstrated that tumor cells cultured in 3D systems displayed properties of increased malignancy and drug resistance compared to standard 2D cultured

68

tumor cells.[17, 19, 42-43] Given the fact that CSCs are responsible for metastasis and drug resistance, the expansion of CSCs in tumor cells cultured in 3D may account for this change.
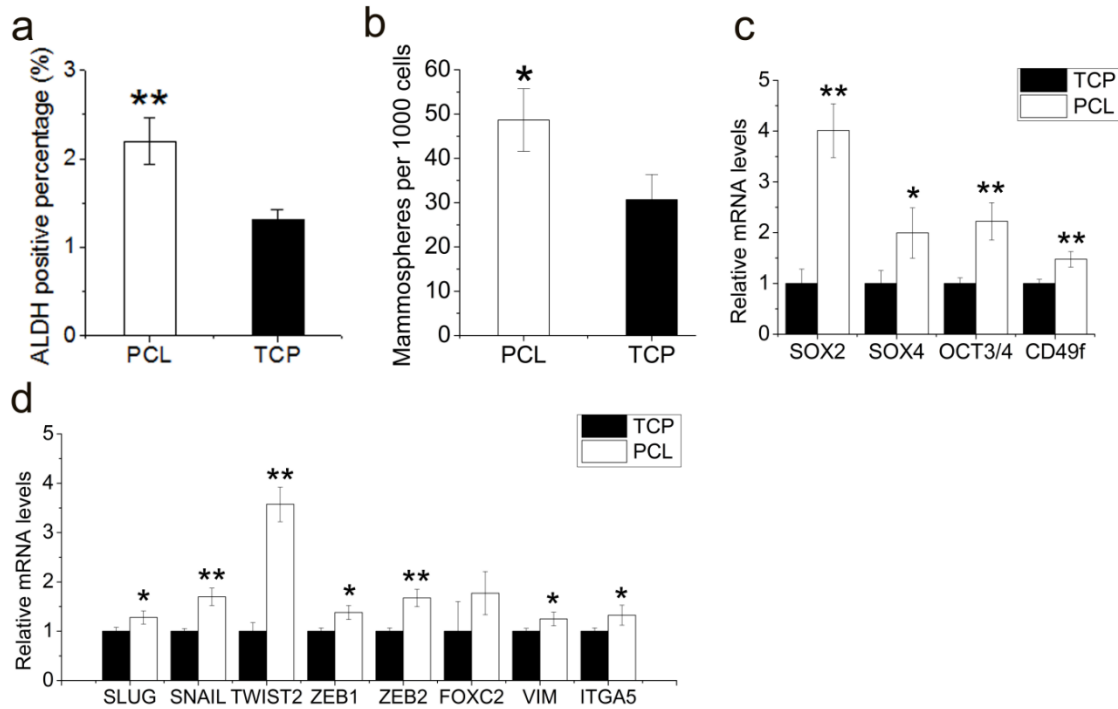
Figure 3.9. MDA-MB-231 cells cultured in PCL fibrous scaffolds displayed increased CSCs properties and gene expression pattern of EMT. (a) The percentage of ALDH-positive cells in MDA-MB-231 cells cultured in TCP and PCL Results were shown as mean ± standard deviation. Statistical significance is indicated by double asterisks (P < 0.001, n = 3). (b) MDA-MB-231 cultured in PCL and TCP were trypsinized and then plated in non-adherent conditions in mammosphere medium, as described in Methods. Mammospheres were numerated. Results were shown as mean ± standard deviation. Statistical significance is denoted by single asterisks (P < 0.05, n = 3). (c) qRT-PCR analysis was used to quantify the expression of stem cell markers, SOX2, SOX4, OCT3/4, and CD49f. (d) qRT-PCR analysis was used to quantify the expression of EMT markers in MDA-MB-231 from PCL and TCP. Results were shown as mean± standard deviation. Statistical significance is indicated by single asterisk (P < 0.05, n = 3) or double asterisks (P < 0.005, n = 3).

3.2.4 The Enhancement of EMT-Associated Properties in Cells from PCL Fibrous Scaffolds

The EMT is a developmental process, in which epithelial cells with tight cell junctions and relative low migratory ability convert to mesenchymal cells with migratory and invasive phenotype. Recent studies demonstrate that during the carcinoma progression, some tumor cells are undergoing the EMT.[44] The inducing factors of EMT include growth factors, cell-matrix interaction, and hypoxia. In addition, EMT may also trigger the transformation of non-stem cancer cells to CSCs, in which tumor cells are acquiring properties of invasion, drug-resistance, chemo-resistance, and radio-resistance.[27]

We previously reported that culture on PCL fibrous scaffolds with either aligned fibers or random fibers can stimulate mouse mammary cell line H605 to undergo EMT.[29] Here, we investigated whether human epithelial-type breast cancer cell lines MCF-7, T47D, and SK-BR-3 cells cultured on PCL fibrous scaffolds were undergoing EMT.

TCP   PCL
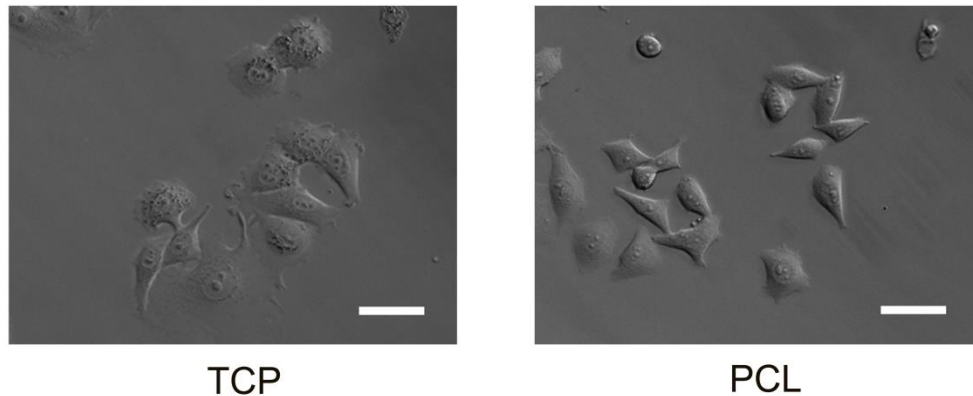
Figure 3.10. Cells from PCL fibrous scaffolds culture displayed a mesenchymal morphology after being re-plated in TCP (right), relative cells from TCP (left). Scale bars indicate 50 μm.

A classical definition of EMT is a multiple step process, in which cells acquire a mesenchymal morphology and then demonstrate increased migration and invasion.[45] MCF-

70

7 cells from PCL fibrous scaffolds were reseeded to TCP, of which about 10% demonstrated elongated spindle-like morphology (Figure 3.10). There was no morphological change for reseeded T47D and SK-BR-3 cells from fibrous scaffolds. Using Transwell assay, we measured invasive property of MCF-7, T47D, and SK-BR-3 cells, a characteristic associated with EMT. Cells from PCL fibrous scaffolds showed significant increases in the number of cells passing through the membrane (Figure 3.11).
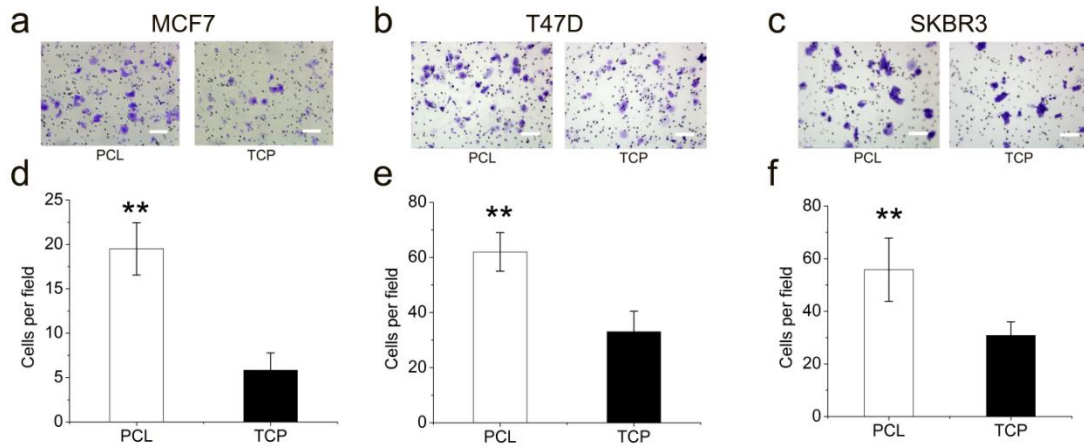
Figure 3.11. Culture on PCL fibrous scaffolds increases the invasion of MCF-7, T47D, and SK-BR-3 cells. (a-c) MCF-7, T47D, SK-BR-3 cells from PCL displayed higher invasive capability in Transwell invasion assay compared to counterparts from TCP. Cells that successfully migrated through the filter pores were fixed with 3.7% paraformaldehyde and stained with 0.5% crystal violet in 2% ethanol. Scale bars indicate 100 μm. (d-f) The average number of migrated cells per field was assessed by counting six random fields. Statistical significance is indicated by double asterisks (P < 0.001, n=3).

To further confirm cells on PCL fibrous scaffolds were undergoing EMT, we measured the transcriptions of EMT related genes in cells from two different culture conditions. The expression of EMT related transcriptional factors, including SLUG, SNAIL, TWIST1, TWIST2, ZEB1, ZEB2, and FOXC2, and other EMT markers, including VIM and ITGA5, were significantly upregulated in MCF-7 cells on PCL fibrous scaffolds in comparison with cells cultured on TCP (Figure 3.14). In T47D cells on PCL fibrous scaffolds, EMT related transcriptional factors, SNAIL, TWIST1, TWIST2, and ZEB2 were
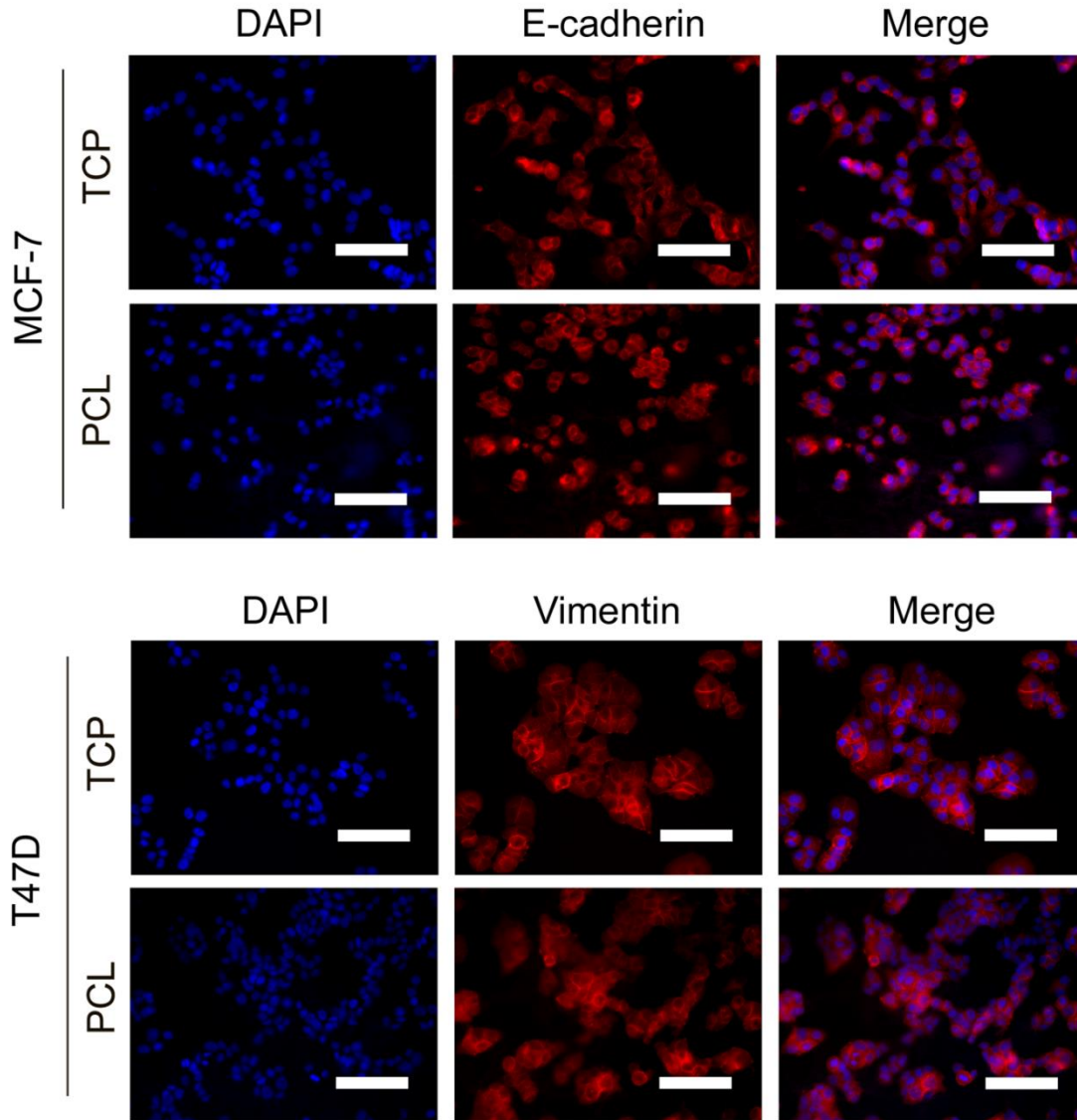
Figure 3.12. Immunofluorescence staining for *E*-cadherin in MCF-7 and T47D cells cultured in tissue culture plastics and PCL fibrous scaffolds. Blue indicates nuclei (DAPI); red indicates *E*-cadherin. All scale bars indicate 100 μm.

upregulated, compared to cells on TCP. In SK-BR-3 cells, only ZEB2, VIM, and ITGA5 were upregulated. Meanwhile, the expression of the epithelial marker, CDH-1 (*E*-cadherin), decreased in cells from PCL fibrous scaffolds relative to cells from TCP (Figure 3.14). Indirect immunofluorescence staining of cells with *E*-cadherin antibody revealed most of cells, if not all, on fibrous scaffolds still expressed *E*-cadherin protein (Figure

www.manaraa.com

3.12). Western blot analysis indicates there is no significant change in protein level for *E*-cadherin and vimentin in cells from fibrous scaffolds relative to cells from TCP (Figure 3.13). It is probably because the cells are still undergoing the early transition of EMT, which is a relatively slow process. For example, TGF-β normally induces EMT within about two weeks.[46] The improvement of invasion and enhancement of expression of EMT markers suggests cells on PCL fibrous scaffolds were undergoing EMT.
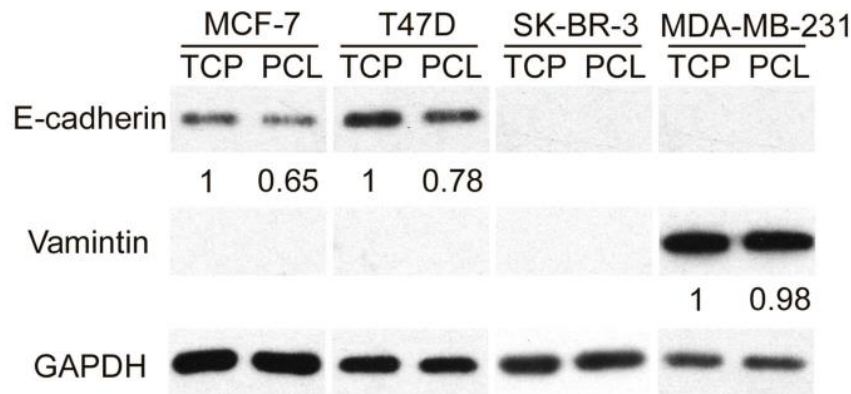
Figure 3.13. After culturing for 6 days on PCL fibrous scaffolds and tissue culture plastics, cell extracts were used for Western blot analysis to detect the expression of *E*-cadherin and Vimentin. The density of each band was quantified with The Image J software and divided by the density of the corresponding GAPDH band. The ratio is presented under each blot after normalizing the values for TCP control as one unit.

It was reported that immortalized human mammary epithelial cells undergoing EMT displayed a shift in CD44 expression from variant isoforms (CD44v) to the standard form (CD44s).[47] In the present study, we observed CD44v, CD44s and CD44t were all upregulated in cells cultured on PCL fibrous scaffolds (Figure 3.15). CD24 regulates TGF-β3 and *E*-cadherin in oral epithelial cells during EMT.[48] The downregulation of CD24 and the upregulation of TGF-β3 in cells culture on fibrous scaffolds suggest cells were undergoing EMT (Figure 3.15).

73
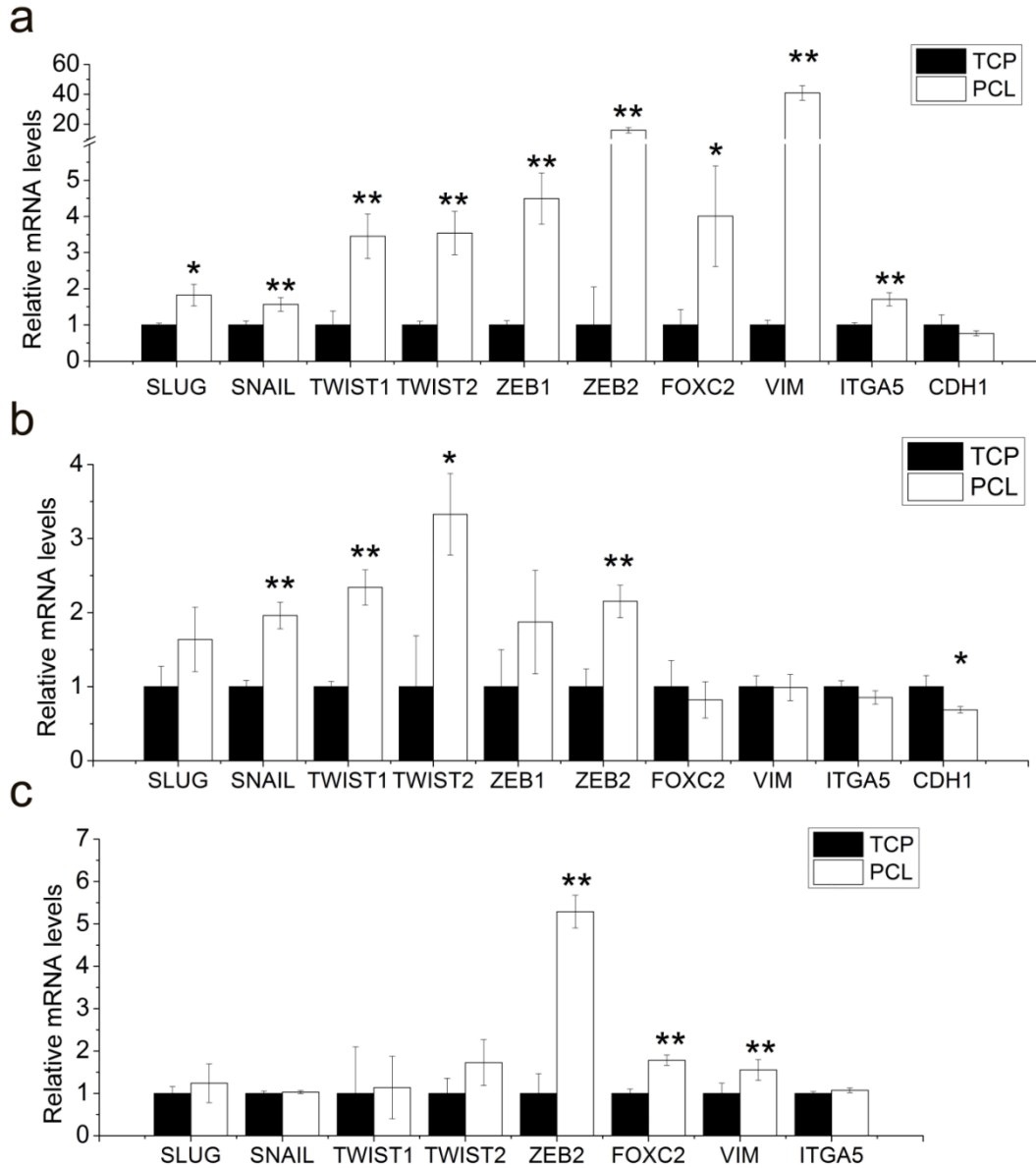
Figure 3.14. PCL fibrous scaffolds culture enhanced the expression of EMT related markers in breast cancer cells. Differential expressions of EMT markers were measured by qRT-PCR in MCF-7 (a), T47D (b), and SK-BR-3 (c) from PCL and TCP. Results were shown as mean ± standard deviation. Statistical significance is indicated by single asterisk (P<0.05, n=3) or double asterisks (P < 0.005, n=3).

MDA-MB-231 cells have basal-like properties and possessed mesenchymal phenotype due to high expression of vimentin.[49-50] Indeed, the basal level of EMT related gene in MDA-MB-231 cells is higher than in epithelial-like cells, MCF7, T47D, and SK-BR-3. Culture on fibrous scaffolds further enhances the expression of EMT related genes

74

in MDA-MB-231 cells (Figure 3.9). It is acknowledged that the EMT process is related to stemness.[27] If the increased CSCs came from the transformation of non-stem cancer cells induced by EMT, CSCs proportion in mesenchymal-type cell line, MDA-MB-231, would not change as dramatically as the epithelial-type cell lines, because the mesenchymal cell line cannot undergo the EMT process.
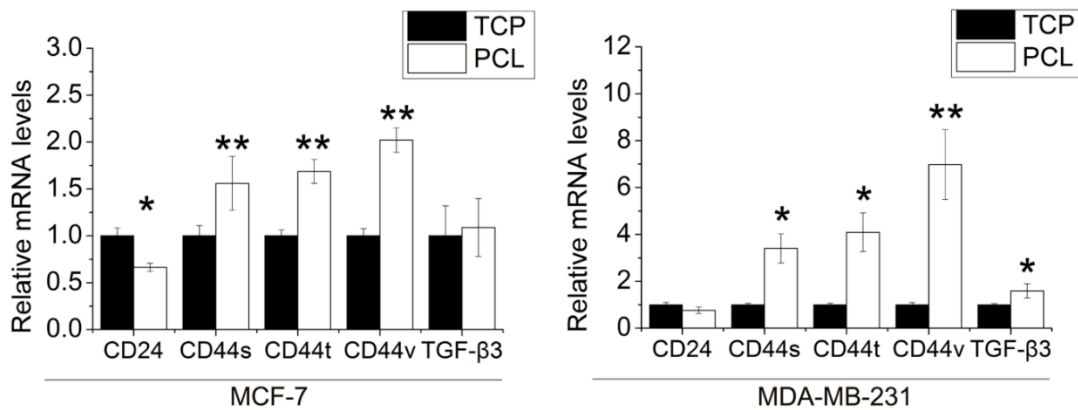
Figure. 15. Real time quantitative PCR analysis of CD24, CD44 variants and TGF-β3 expression in MCF-7 and MDA-MB-231 cells cultured in 3D scaffolds compared to cells on tissue culture plastics. Results were shown as mean ± standard deviation. Statistical significance is indicated by single asterisk (P < 0.05, n=3) or double asterisks (P < 0.005, n=3).

Previous study suggests MCF-7 cells in 3D collagen scaffolds were induced to undergo EMT may be due to the adaption to the hypoxia condition.[51] In our study most of cells localized on the surface of scaffolds, and a few cells infiltrated into lower layers, which is not sufficient to induce the hypoxia condition. Therefore it might be other factor rather than hypoxia that induced cells to undergo EMT in this case. It is acknowledged that compressive forces generated by the interaction between cells and their surrounding environment can cause, either directly or indirectly, alterations of cell in the structure and function of ECM receptors to actively influence signaling pathway. EMT in the tumor environment is a force-dependent phenomenon.[52] TGF-β studies revealed that dynamic

75

compression and contraction of cell-matrix interaction activates latent ECM bound TGF-β, thereafter stimulates a feedback loop to induce EMT in the cell itself.[53-54] Further research will be required to elucidate the detailed mechanism of how the 3D PCL fibrous scaffolds induce cells to undergo EMT.

Although EMT can induce the conversion of non-stem cancer cells to CSCs, a recent study suggests EMT and stemness are not necessarily linked.[55] In the present study, we found PCL fibrous scaffolds culture condition increased CSCs properties and induced EMT. However, it is still unclear whether that EMT and the increase of CSCs are two independent events or two events with causal relationship. Further work needs to be done to understand the relationship between EMT and the increase of CSCs in electrospun PCL fibrous scaffolds.

3.3 CONCLUSIONS

Cancer stem cells, which are responsible for the tumorigenesis, chemo-resistance, radio-resistance, and metastases, play a vital role in the tumor initiation and regression. Previous studies suggest that cells in traditional 2D culture fail to represent in vivo tumor cells, due to the loss of the malignancy. In the present study, using electrospinning process, we generated PCL fibrous scaffolds for 3D cell culture. Three epithelial-type breast cancer cell lines, including MCF-7, T47D, SK-BR-3, cultured on PCL fibrous scaffolds showing increased CSCs population relative to cells cultured on TCP, which may likely attribute to the EMT process.

Recently we have developed a set of mathematical models with two negative feedbacks to explore essential biological factors that control the CSC population during tumor growth, in which an excellent agreement with experimental data has been achieved.

76

To characterize the underlying features of CSCs induced by 3D PCL fibrous scaffolds, we plan next to extend mathematical models as proposed by including the transformation from non-stem cells to CSCs to further investigate whether the enrichment of CSCs by 3D PCL fiber scaffolds is primarily due to transformation of non-stem cells to CSCs, or increasing symmetric division or differentiation rates of CSCs, or the combination of these different factors. With this data, we anticipated that PCL fibrous scaffolds culture system, in which cells demonstrate higher malignancy and the expansion of CSCs, could be used as a useful scaffold for the evaluation of novel anti-cancer drugs and the enrichment of cancer stem cells *in vitro*.

3.4 EXPERIMENTS

3.4.1 Preparation of Electrospun PCL Fibrous Scaffolds

A 15% w/w solution of poly (ε-caprolactone) (PCL) (Average M_n ca. 60 kDa, Sigma), in 1,1,1,3,3,3-hexafluro-2-propanol (HFIP) (Sigma Aldrich) were made. The electrospinning system are placed in a humidity-controlled chamber and schematically depicted in Figure 3.1a. The electrospinning process was conducted as follows: The polymer solution was transferred to a 1.0 mL plastic syringe (BD) with a 21 G blunt needle (BD precision glide). A syringe driver was used to control the solution flow rate at 15 µL min^{-1}. A high voltage supply (HVR Orlando, FL) was used to build up a voltage of 6-7 kV electro filed between the needle and the grounded collector. The distance between the collector and needle was fixed at 10 cm. The PCL fibrous scaffold was fertilized by immersing into 75% ethanol for 20 min, dried overnight and then irradiated under ultraviolet light for 20 min in a laminar flow hood.

77

3.4.2 Cell Culture

Human breast cancer cell lines MCF-7, T47D, SK-BR-3, and MB-MDA-231 were purchased from the American Type Culture Collection. MCF-7 and MDA-MB-231 cell were cultured in Dulbecco's modified Eagle's medium (DMEM, #D6046, Sigma–Aldrich) supplemented with 10% heat inactivated fetal bovine serum (Hyclone, Thermo Scientific), 100 U mL^{-1} penicillin and 100 μg mL^{-1} streptomycin (Gibco BRL, Invitrogen Corp., Carlsbad, CA, USA). T47D was maintained in RPMI-1604 media (Sigma-Aldrich) containing 10% FBS, 100 U mL^{-1} penicillin and 100 μg mL^{-1} streptomycin. SK-BR-3 was maintained in KBR3 cells were grown in McCoy's 5A (Sigma-Aldrich) supplemented with 10% FBS, 10% FBS and 100 U mL^{-1} penicillin and 100 μg mL^{-1} streptomycin. Cells were cultured in a 5% CO_2 humidified incubator at 37 ℃. Sterilized PCL fiber scaffolds were soaked in media 30 min prior cell seeding. Cells in exponential growth phase were trypsinized by 0.25% trypsin and seeded on PCL fibrous scaffold at a density of 5.2×10^3 cells per cm^2. The cells used in experiments were cultured on PCL and TCP for 6 days without passage, unless otherwise specified.

3.4.3 Confocal and Scanning Electron Microscopy Studies

Cells on PCL fiber scaffolds were rinsed with phosphate buffered saline (PBS) twice and fixed with 4% paraformaldehyde for 20 min at room temperature. Then scaffolds were rinsed with PBS. Cells were permeabilized with 0.2% Triton X-100 for 10 min. To prevent non-specific labeling, 3% bovine serum albumin (BSA) in PBS were applied as a blocking buffer for 20 min. Actin cytoskeleton was stained with rhodamine phalloidin (Cytoskeleton Inc.) (1:200) in a blocking buffer for 20 min, and nuclei were stained with 4′,6-diamidino-2-phenylindole (DAPI) (Invitrogen) in a blocking buffer for 10 min. The

78

fluorescence was visualized and captured under confocal microscope (Olympus IX81) with DAPI filter and Cy3 filter set. The morphology of PCL fiber scaffolds were examined by a field emission scanning electron microscopy (FEI Quanta 200 ESEM). PCL scaffold samples were dried with nitrogen, and coated with gold for 30 seconds with sputter coater. To examine the uniformity of the fiber diameters several areas were imaged. Fiber diameters were measured using image J (National Institutes of Health).

3.4.4 ALDEFLUOR Assay

The ALDEFLUOR kit (Stem Cell Technologies, Durham, NC, USA) was used to identify the cancer stem cell population with high ALDH enzyme activity. Briefly, the cells were suspended in ALDEFLUOR assay buffer containing ALDH substrate BAAA (1 μM) in a concentration of 1×10^6 cells mL^{-1} and incubated for 45 min at 37 °C. As a negative control, the ALDH inhibitor, diethylaminobenzaldehyde (DEAB) (15 μM) were added to the cell suspension in ALDEFLUOR assay buffer with BAAA. A Cytomics FC500 flow cytometry system (Beckman Coulter Inc., Miami, FL, USA) was used to detect the ALDH-positive cell population.

3.4.5 Cell Proliferation Assay

The effect of PCL fiber scaffolds on cell growth was assessed by CellTiter-Blue™ Cell Viability Assay (Promega, Madison, WI). The cell titer blue reagent was added to the medium directly (100 μL per 1 mL medium) and incubated for four hours at 37°C. Fluorescence at $560_{ex}/590_{em}$ nm filter setting was measured using a Tecan infinite M200 plate reader (Tecan, Salzburg, Austria). After correction of background fluorescence, the intensity of fluorescence for each sample was normalized by the first day intensity of

fluorescence. The cell viabilities on day 1, 3, 5, 7, 9, 11, and 13 were determined. Three independent experiments were determined for each case.

3.4.6 Mammosphere Formation Assay

Cells from 2D culture or 3D PCL fibrous scaffolds were plated in ultralow attachment six-well plates (Corning, Acton, MA, USA) at a density of 10000 cells mL^{-1} for MCF-7 and 1000 cells mL^{-1} for MDA-MB-231. in serum-free DMEM/F12 medium (Invitrogen, Carlsbad, CA, USA) supplemented with 20 ng mL^{-1} epidermal growth factor (sigma, St Louis, MO, USA), 10 ng mL^{-1} basic fibroblast growth factor (Sigma), 5 µg mL^{-1} insulin (Sigma), $1 \times$ B27 supplement (Invitrogen) and 0.4% bovine serum albumin (Sigma). Cells were cultured in a 5% CO_2 humidified incubator at 37 ℃ for a week. The number of mammospheres was counted under microscopy. Three independent experiments were performed for each group.

3.4.7 RNA Extraction and Quantitative Reverse-Transcription PCR

Total RNA was isolated using RNeasy mini purification kit (Qiagen). Quantitative reverse-transcription PCR (qRT-PCR) was performed in two steps. Isolated RNA reverse-transcribed with qScript^{TM} cDNA synthesis kit (Quanta Biosciences Inc.) and then Quantitative (Real-time) PCR was performed with Bio-Rad iCycler with My iQ™ camera detection system and the method used was 40 cycles of PCR (95 ℃ for 30 s, 60 ℃ for 15 s, 72°C for 30s), after initial denaturation step of 5 min at 95°C. In a 25 µL total volume of reaction mixture, 12.5 µL iQ SYBR-Green™ SuperMix (Bio-Rad), 400 nM of both forward and reverse primers (Table 3.1) and the cDNA template at a final concentration of 25 ng µL^{-1} were employed. Data analysis was performed using $2^{-\Delta\Delta C}T$ method for relative

quantification,[56] and all samples were normalized to GAPDH expression as the internal control.

3.4.8 Transwell Invasion Assay

The invasion chamber consisted of a cell culture insert with a membrane pore size of 8 μm in a 24-well plate (BD Biocoat^{TM} Matrigel^{TM} Invasion Chamber, BD Biosciences, Franklin Lakes, NJ). Cells cultured in 2D and 3D were trypsinized and washed by PBS. Then cells were plated in the top chamber with Matrigel-coated membrane at a density of 2.5×10^5 cells per well for MCF-7 and 1×10^6 cells per well for SK-BR-3 and T47D. Cells were plated in the serum free medium and medium with 10% FBS was used as a chemoattractant in the lower chamber. The cells were incubated in a 5% CO_2 humidified incubator at 37 ℃ for 72 h. Cells fail to invade through pores were removed by a cotton swab. Cells on the lower surface of the membrane were fixed 3.7% paraformaldehyde and stained with 0.5% crystal violet in 2% and counted under a microscopy.

3.4.9 Statistical analysis

All assays were performed in triplicates unless otherwise stated. Data are indicated as mean $\pm$ standard deviation. Comparisons between two groups were done using unpaired student's t-test.

Table 3.1. List of primers

Gene Name	Forward sequence 5'-3'	Reverse sequence 3'-5'
SOX2	GCTTTTGTTCGATCCCAACTTTC	ATGGATTCTCGGCAGACTGATTC
OCT3/4	CGAAAGAGAAAGCGAACCAGTATC	AGAACCACACTCGGACCACATC
SOX4	GCATGATGATAGCATATGTGTTCAGGT	CGGCATATTGCACAGGATGGA
ITGA6	CAAATGCAGGCACTCAGGTTC	GCATCAAGATCCCAGCGAGA
ITGA5	GTCAGCAGCTCCTATATGTGACCAGA	CCCTCGGGATCCAACTCCAG
SNAIL	GCCTAGCGAGTGGTTCTTCTG	CTGCTGGAAGGTAAACTCTGGATT
SLUG	GCGAACTGGACACACATACAGTGAT	GTGGAATGGAGCAGCGGTAGT
ZEB1	GAGACATAAATATGAACACACAGGTAAAAGAC	TTGAGAATAAGACCCAGAGTGTGAGAAG
ZEB2	CCACCAGTCCAGACCAGTATTCCT	CATCAAGCAATTCTCCCTGAAATC
TWIST1	GCCGGAGACCTAGATGTCATTGT	GCCCTGTTTCTTTGAATTTGGAT
TWIST2	GCTGCCCTCTGACAAGCTGA	CTTATTGTCCATCTCGTCGCTCTG
VIM	GAAGGCGAGGAGAGCAGGATT	AGAAGTTTCGTTGATAACCTGTCCA
FOXC2	CAGCAGCAAACTTTCCCCAAC	CAGTATTTCGTGCAGTCGTAGGAGTAG
CDH-1	AGGCCAAGCAGCAGTACATT	ATTCACATCCAGCACATCCA
CD24	AAACAACAACTGGAACTTCAAGTAACTC	GGTGGTGGCATTAGTTGGATTT
CD44t	TCCAACACCTCCCAGTATGACA	GGCAGGTCTGTGACTGATGTACA
CD44v	CCACATTCTACAAGCACAA	CTGTTGCCAAACCACTGTTCC
CD44s	TCCCTGCTACCAGAGACCAAGACA	ACCAGAGGTTGTGTTTGCTCCACC
GAPDH	GAGTCAACGGATTTGGTCGTAT	ATGGGTGGAATCATATTGGAAC
TGF-beta3	AGCGGAATGAGCAGAGGATCGA	CTCAACAGCCACTCACGCACAG

3.5 REFERENCE

1. Feng, S.; Duan, X.; Lo, P. K.; Liu, S.; Liu, X.; Chen, H.; Wang, Q. Expansion of breast cancer stem cells with fibrous scaffolds. *Integr Biol (Camb)* **2013,** *5* (5), 768-77.

2. Kim, J. B. Three-dimensional tissue culture models in cancer biology. *Seminars in cancer biology* **2005,** *15* (5), 365-77.

3. Griffith, L. G.; Swartz, M. A. Capturing complex 3D tissue physiology in vitro. *Nature reviews. Molecular cell biology* **2006,** *7* (3), 211-24.

4. Szot, C. S.; Buchanan, C. F.; Freeman, J. W.; Rylander, M. N. 3D in vitro bioengineered tumors based on collagen I hydrogels. *Biomaterials* **2011,** *32* (31), 7905-12.

5. Anisimov, V. N.; Ukraintseva, S. V.; Yashin, A. I. Cancer in rodents: does it tell us about cancer in humans? *Nature reviews. Cancer* **2005,** *5* (10), 807-19.

6. Rangarajan, A.; Weinberg, R. A. Opinion: Comparative biology of mouse versus human cells: modelling human cancer in mice. *Nature reviews. Cancer* **2003,** *3* (12), 952-9.

7. Frijhoff, A. F.; Conti, C. J.; Senderowicz, A. M. Advances in molecular carcinogenesis: current and future use of mouse models to screen and validate molecularly targeted anticancer drugs. *Molecular carcinogenesis* **2004,** *39* (4), 183-94.

8. de Jong, G. M.; Aarts, F.; Hendriks, T.; Boerman, O. C.; Bleichrodt, R. P. Animal models for liver metastases of colorectal cancer: research review of preclinical studies in rodents. *J Surg Res* **2009,** *154* (1), 167-76.

9. Rangarajan, A.; Hong, S. J.; Gifford, A.; Weinberg, R. A. Species- and cell type-specific requirements for cellular transformation. *Cancer cell* **2004,** *6* (2), 171-83.

10.   Hartman, O.; Zhang, C.; Adams, E. L.; Farach-Carson, M. C.; Petrelli, N. J.; Chase, B. D.; Rabolt, J. F. Biofunctionalization of electrospun PCL-based scaffolds with perlecan domain IV peptide to create a 3-D pharmacokinetic cancer model. *Biomaterials* **2010,** *31* (21), 5700-18.

11.   Szot, C. S.; Buchanan, C. F.; Gatenholm, P.; Rylander, M. N.; Freeman, J. W. Investigation of cancer cell behavior on nanofibrous scaffolds. *Mat Sci Eng C-Mater* **2011,** *31* (1), 37-42.

12.   Han, D.; Gouma, P. I. Electrospun bioscaffolds that mimic the topology of extracellular matrix. *Nanomedicine : nanotechnology, biology, and medicine* **2006,** *2* (1), 37-41.

13.   Nisbet, D. R.; Forsythe, J. S.; Shen, W.; Finkelstein, D. I.; Horne, M. K. Review paper: a review of the cellular response on electrospun nanofibers for tissue engineering. *Journal of biomaterials applications* **2009,** *24* (1), 7-29.

14.   Cipitria, A.; Skelton, A.; Dargaville, T. R.; Dalton, P. D.; Hutmacher, D. W. Design, fabrication and characterization of PCL electrospun scaffolds—a review. *Journal of Materials Chemistry* **2011,** *21* (26), 9419-53.

15.   Yamada, K. M.; Cukierman, E. Modeling tissue morphogenesis and cancer in 3D. *Cell* **2007,** *130* (4), 601-10.

16.   Wang, X.; Sun, L.; Maffini, M. V.; Soto, A.; Sonnenschein, C.; Kaplan, D. L. A complex 3D human tissue culture system based on mammary stromal cells and silk scaffolds for modeling breast morphogenesis and function. *Biomaterials* **2010,** *31* (14), 3920-9.

17.	Fischbach, C.; Chen, R.; Matsumoto, T.; Schmelzle, T.; Brugge, J. S.; Polverini, P. J.; Mooney, D. J. Engineering tumors with 3D scaffolds. *Nat Methods* **2007,** *4* (10), 855-60.

18.	Faute, M. A. D.; Laurent, L.; Ploton, D.; Poupon, M. F.; Jardillier, J. C.; Bobichon, H. Distinctive alterations of invasiveness, drug resistance and cell-cell organization in 3D-cultures of MCF-7, a human breast cancer cell line, and its multidrug resistant variant. *Clinical & experimental metastasis* **2002,** *19* (2), 161-168.

19.	Leung, M.; Kievit, F. M.; Florczyk, S. J.; Veiseh, O.; Wu, J.; Park, J. O.; Zhang, M. Chitosan-alginate scaffold culture system for hepatocellular carcinoma increases malignancy and drug resistance. *Pharm Res* **2010,** *27* (9), 1939-48.

20.	Pollard, S. M.; Yoshikawa, K.; Clarke, I. D.; Danovi, D.; Stricker, S.; Russell, R.; Bayani, J.; Head, R.; Lee, M.; Bernstein, M.; Squire, J. A.; Smith, A.; Dirks, P. Glioma stem cell lines expanded in adherent culture have tumor-specific phenotypes and are suitable for chemical and genetic screens. *Cell stem cell* **2009,** *4* (6), 568-80.

21.	Chen, L.; Xiao, Z. F.; Meng, Y.; Zhao, Y. N.; Han, J.; Su, G. N.; Chen, B.; Dai, J. W. The enhancement of cancer stem cell properties of MCF-7 cells in 3D collagen scaffolds for modeling of cancer and anti-cancer drugs. *Biomaterials* **2012,** *33* (5), 1437-44.

22.	Abraham, B. K.; Fritz, P.; McClellan, M.; Hauptvogel, P.; Athelogou, M.; Brauch, H. Prevalence of CD44(+)/CD24(-/low) cells in breast cancer may not be associated with clinical outcome but may favor distant metastasis. *Clinical Cancer Research* **2005,** *11* (3), 1154-59.

85

23.	Li, X. X.; Lewis, M. T.; Huang, J.; Gutierrez, C.; Osborne, C. K.; Wu, M. F.; Hilsenbeck, S. G.; Pavlick, A.; Zhang, X. M.; Chamness, G. C.; Wong, H.; Rosen, J.; Chang, J. C. Intrinsic resistance of tumorigenic breast cancer cells to chemotherapy. *Journal of the National Cancer Institute* **2008,** *100* (9), 672-9.

24.	Diehn, M.; Cho, R. W.; Lobo, N. A.; Kalisky, T.; Dorie, M. J.; Kulp, A. N.; Qian, D. L.; Lam, J. S.; Ailles, L. E.; Wong, M. Z.; Joshua, B.; Kaplan, M. J.; Wapnir, I.; Dirbas, F. M.; Somlo, G.; Garberoglio, C.; Paz, B.; Shen, J.; Lau, S. K.; Quake, S. R.; Brown, J. M.; Weissman, I. L.; Clarke, M. F. Association of reactive oxygen species levels and radioresistance in cancer stem cells. *Nature* **2009,** *458* (7239), 780-3.

25.	Ginestier, C.; Hur, M. H.; Charafe-Jauffret, E.; Monville, F.; Dutcher, J.; Brown, M.; Jacquemier, J.; Viens, P.; Kleer, C. G.; Liu, S.; Schott, A.; Hayes, D.; Birnbaum, D.; Wicha, M. S.; Dontu, G. ALDH1 is a marker of normal and malignant human mammary stem cells and a predictor of poor clinical outcome. *Cell stem cell* **2007,** *1* (5), 555-67.

26.	Dontu, G.; Abdallah, W. M.; Foley, J. M.; Jackson, K. W.; Clarke, M. F.; Kawamura, M. J.; Wicha, M. S. In vitro propagation and transcriptional profiling of human mammary stem/progenitor cells. *Genes & development* **2003,** *17* (10), 1253-1270.

27.	Mani, S. A.; Guo, W.; Liao, M. J.; Eaton, E. N.; Ayyanan, A.; Zhou, A. Y.; Brooks, M.; Reinhard, F.; Zhang, C. C.; Shipitsin, M.; Campbell, L. L.; Polyak, K.; Brisken, C.; Yang, J.; Weinberg, R. A. The epithelial-mesenchymal transition generates cells with properties of stem cells. *Cell* **2008,** *133* (4), 704-15.

28.	Provenzano, P. P.; Eliceiri, K. W.; Campbell, J. M.; Inman, D. R.; White, J. G.; Keely, P. J. Collagen reorganization at the tumor-stromal interface facilitates local invasion. *Bmc Med* **2006,** *4* (1), 38.

29. Saha, S.; Duan, X.; Wu, L.; Lo, P. K.; Chen, H.; Wang, Q. Electrospun fibrous scaffolds promote breast cancer cell alignment and epithelial-mesenchymal transition. *Langmuir* **2012,** *28* (4), 2028-34.

30. Chute, J. P.; Muramoto, G. G.; Whitesides, J.; Colvin, M.; Safi, R.; Chao, N. J.; McDonnell, D. P. Inhibition of aldehyde dehydrogenase and retinoid signaling induces the expansion of human hematopoietic stem cells. *Proceedings of the National Academy of Sciences of the United States of America* **2006,** *103* (31), 11707-12.

31. Charaffe-Jauffret, E.; Ginestier, C.; Iovino, F.; Tarpin, C.; Diebel M.; Esterni B.; Houvenaeghel G.; Extra J. M.; Bertucci F.; Jacquemier J.; Xerri L.; Dontu, G.; Stassi G.; Xiao Y.; Barsky S. H.; Birnbaum, D.; Viens, P.; Wicha, M. S. Aldehyde Dehydrogenase 1–Positive Cancer Stem Cells Mediate Metastasis and Poor Clinical Outcome in Inflammatory Breast Cancer. *Clin Cancer Res.* **2010,** *16*(1), 45-55.

32. Wang, Y.; Zhe, H.; Gao, P.; Zhang, N.; Li, G.; Qin, J. Cancer stem cell marker ALDH1 expression is associated with lymph node metastasis and poor survival in esophageal squamous cell carcinoma: a study from high incidence area of northern China. *Diseases of the esophagus : official journal of the International Society for Diseases of the Esophagus / I.S.D.E* **2011**.

33. Croker, A. K.; Goodale, D.; Chu, J.; Postenka, C.; Hedley, B. D.; Hess, D. A.; Allan, A. L. High aldehyde dehydrogenase and expression of cancer stem cell markers selects for breast cancer cells with enhanced malignant and metastatic ability. *Journal of cellular and molecular medicine* **2009,** *13* (8B), 2236-52.

34. Storms, R. W.; Trujillo, A. P.; Springer, J. B.; Shah, L.; Colvin, O. M.; Ludeman, S. M.; Smith, C. Isolation of primitive human hematopoietic progenitors on the basis of

aldehyde dehydrogenase activity. *Proceedings of the National Academy of Sciences of the United States of America* **1999,** *96* (16), 9118-23.

35.   Reynolds, B. A.; Rietze, R. L. Neural stem cells and neurospheres--re-evaluating the relationship. *Nat Methods* **2005,** *2* (5), 333-6.

36.   Jinesh, G. G.; Choi, W.; Shah, J. B.; Lee, E. K.; Willis, D. L.; Kamat, A. M. Blebbishields, the emergency program for cancer stem cells: sphere formation and tumorigenesis after apoptosis. *Cell death and differentiation* **2013,** 20(3), 382-95.

37.   Okumura-Nakanishi, S.; Saito, M.; Niwa, H.; Ishikawa, F. Oct-3/4 and Sox2 regulate Oct-3/4 gene in embryonic stem cells. *The Journal of biological chemistry* **2005,** *280* (7), 5307-17.

38.   Zhang, J.; Liang, Q.; Lei, Y.; Yao, M.; Li, L.; Gao, X.; Feng, J.; Zhang, Y.; Gao, H.; Liu, D. X.; Lu, J.; Huang, B. SOX4 induces epithelial-mesenchymal transition and contributes to breast cancer progression. *Cancer research* **2012,** 72(17), 4597-608.

39.   Stingl, J.; Eirew, P.; Ricketson, I.; Shackleton, M.; Vaillant, F.; Choi, D.; Li, H. I.; Eaves, C. J. Purification and unique properties of mammary epithelial stem cells. *Nature* **2006,** *439* (7079), 993-7.

40.   Lo, P. K.; Kanojia, D.; Liu, X.; Singh, U. P.; Berger, F. G.; Wang, Q.; Chen, H. CD49f and CD61 identify Her2/neu-induced mammary tumor-initiating cells that are potentially derived from luminal progenitors and maintained by the integrin-TGFbeta signaling. *Oncogene* **2012,** *31* (21), 2614-26.

41.   Yu, K. R.; Yang, S. R.; Jung, J. W.; Kim, H.; Ko, K.; Han, D. W.; Park, S. B.; Choi, S. W.; Kang, S. K.; Scholer, H.; Kang, K. S. CD49f Enhances Multipotency and Maintains

Stemness Through the Direct Regulation of OCT4 and SOX2. *Stem Cells* **2012,** *30* (5), 876-87.

42.   Horning, J. L.; Sahoo, S. K.; Vijayaraghavalu, S.; Dimitrijevic, S.; Vasir, J. K.; Jain, T. K.; Panda, A. K.; Labhasetwar, V. 3-D tumor model for in vitro evaluation of anticancer drugs. *Molecular pharmaceutics* **2008,** *5* (5), 849-62.

43.   Xu, F.; Burg, K. J. Three-dimensional polymeric systems for cancer cell studies. *Cytotechnology* **2007,** *54* (3), 135-43.

44.   Tomaskovic-Crook, E.; Thompson, E. W.; Thiery, J. P. Epithelial to mesenchymal transition and breast cancer. *Breast Cancer Research* **2009,** *11* (6), 213.

45.   Thiery, J. P. Epithelial-mesenchymal transitions in tumour progression. *Nature reviews. Cancer* **2002,** *2* (6), 442-54.

46.   Oft, M.; Peli, J.; Rudaz, C.; Schwarz, H.; Beug, H.; Reichmann, E. TGF-beta1 and Ha-Ras collaborate in modulating the phenotypic plasticity and invasiveness of epithelial tumor cells. *Genes & development* **1996,** *10* (19), 2462-77.

47.   Brown, R. L.; Reinke, L. M.; Damerow, M. S.; Perez, D.; Chodosh, L. A.; Yang, J.; Cheng, C. CD44 splice isoform switching in human and mouse epithelium is essential for epithelial-mesenchymal transition and breast cancer progression. *The Journal of clinical investigation* **2011,** *121* (3), 1064-74.

48.   Ye, P.; Nadkarni, M. A.; Hunter, N. Regulation of E-cadherin and TGF-beta3 expression by CD24 in cultured oral epithelial cells. *Biochemical and biophysical research communications* **2006,** *349* (1), 229-35.

49.   Chen, M. H.; Yip, G. W.; Tse, G. M.; Moriya, T.; Lui, P. C.; Zin, M. L.; Bay, B. H.; Tan, P. H. Expression of basal keratins and vimentin in breast cancers of young women

correlates with adverse pathologic parameters. *Modern pathology : an official journal of the United States and Canadian Academy of Pathology, Inc* **2008,** *21* (10), 1183-91.

50.   Vuoriluoto, K.; Haugen, H.; Kiviluoto, S.; Mpindi, J. P.; Nevo, J.; Gjerdrum, C.; Tiron, C.; Lorens, J. B.; Ivaska, J. Vimentin regulates EMT induction by Slug and oncogenic H-Ras and migration by governing Axl expression in breast cancer. *Oncogene* **2011,** *30* (12), 1436-48.

51.   Yang, M. H.; Wu, K. J. TWIST activation by hypoxia inducible factor-1 (HIF-1): implications in metastasis and development. *Cell Cycle* **2008,** *7* (14), 2090-6.

52.   Lopez, J. I.; Mouw, J. K.; Weaver, V. M. Biomechanical regulation of cell orientation and fate. *Oncogene* **2008,** *27* (55), 6981-93.

53.   Wells, R. G.; Discher, D. E. Matrix elasticity, cytoskeletal tension, and TGF-beta: the insoluble and soluble meet. *Science signaling* **2008,** *1* (10), pe13.

54.   Wipff, P. J.; Rifkin, D. B.; Meister, J. J.; Hinz, B. Myofibroblast contraction activates latent TGF-beta1 from the extracellular matrix. *The Journal of cell biology* **2007,** *179* (6), 1311-23.

55.   Ocana, O. H.; Corcoles, R.; Fabra, A.; Moreno-Bueno, G.; Acloque, H.; Vega, S.; Barrallo-Gimeno, A.; Cano, A.; Nieto, M. A. Metastatic colonization requires the repression of the epithelial-mesenchymal transition inducer prrx1. *Cancer cell* **2012,** *22* (6), 709-24.

56.   Livak, K. J.; Schmittgen, T. D. Analysis of relative gene expression data using real-time quantitative PCR and the 2(-Delta Delta C(T)) Method. *Methods* **2001,** *25* (4), 402-8.

90

CHAPTER 4

BIOLOGICAL THIOLS-TRIGGERED HYDROGEN SULFIDE RELEASING MICROFIBERS FOR TISSUE ENGINEERING APPLICATIONS

4.1 INTRODUCTION

Hydrogen sulfide (H_2S) has long been considered as a malodorous toxic gas. Abe and Kimura first reported the possible role of endogenous H_2S in the neuromodulation,[1] indicating the biological relevance of H_2S as a gasotransmitter. Together with nitric oxide (NO) and carbon monoxide (CO), H_2S forms part of a group of active gaseous molecules that modulate cellular functions through intracellular signaling cascades.[2] Most, if not all, of endogenous formation of H_2S is attributed to four enzymes, cystathionine β-synthase (CBS), cystathionine γ-lyase (CSE), and the tandem enzymes cysteine aminotransferase (CAT) and 3-mercaptopyruvate sulfurtransferase (3-MST).[3-5] Tightly controlled endogenous H_2S has involved in diverse physiological and pathophysiological processes, including learning and memory, neurodegeneration, regulation of inflammation and blood pressure, metabolism, and anti-apoptosis.[6] Possessing all positive effects of NO without generating a toxic metabolite such as $ONOO^-$,[7] H_2S holds great therapeutic potential for various diseases and has drawn increased attention of biomedical scientists.

Limited available H_2S releasing agents (i.e. H_2S donors), such as sulfide salts, natural polysulfide compounds such as diallyl trisulfide, synthetic H_2S donors such as Lawesson's reagent derivative, GYY4137, have been developed and applied for the studies of the physiological and pathological functions of H_2S.[8] Recently, a polymeric H_2S donor

synthesized by conjugating 5-(4-hydroxyphenyl)-3H-1,2-dithiole-3-thione (ADT-OH) to polymers showed effects of potentiating lipopolysaccharide-induced inflammation and altered cellular trafficking.[9] However, the shortage of aforementioned H_2S donors is that the H_2S release is either too fast or uncontrollable, which poorly mimic the biological generation of H_2S. To overcome this drawback, we have developed a series of N-(benzoylthio)benzamides derivatives (NSHD), which are controllable and have a relative slow-releasing profile.[10] The H_2S release of these donors can be triggered by biological thiols such as cysteine and glutathione (GSH), which are prevail in the biological system. Therefore, NSHDs are promising candidate for H_2S-based therapeutic strategy.

Electrospinning is a simple, cost-effective, and versatile technique in which natural or synthetic polymers are fabricated into fibers with diameters ranging from tens nanometers to micrometers. The unique advantages, such as high surface to volume ratio, adjustable porosity and fibers orientation, and the flexibility to form various sizes, make the electrospun fibers an ideal system for a broad range of biomedical applications, such as wound dressing, blood vessel tissue engineering, neural repair, bone or cartilage tissue engineering, and controlled drug release, as described in several reviews.[11-13] Previously, researchers have functionalized electrospun fibers with biological relevant macromolecules, such as low molecular weight heparin,[14] growth factor BMP2,[15] neural growth factor,[16] and specific genes.[17] Notably, several groups have generated electrospun fibers with capability to release gaseous messenger nitric oxide.[18-22] Though emerging role of H_2S in physiological and pathophysiological processes indicates H_2S holds great therapeutic potential,[23] to the best of our knowledge, no H_2S-releasing electrospun fibers (H_2S-fibers) has been generated and evaluated so far.

Fibrous scaffolds generated by electrospinning have been used to generate substitutes and grafts for various tissue regeneration and achieved significant progress.[12] The electrospun fibers served as cell scaffolds for the therapeutic cells to adhere, proliferate, and differentiation, in the damaged tissues or organs.[11] However, in the process of transplantation of organs, tissue substitutes, and therapeutic cells, ischemia *in vitro* and post-transplantation is the most well-known cause of malfunction of transplanted grafts. [24-25] Since the production of endogenous H_2S and the exogenous administration of H_2S elicit a wide range of protective actions, especially in cardiovascular systems, including vasodilation, anti-inflammatory, antioxidant, and down regulation of cellular metabolism under stress,[23, 26] H_2S-fibers would enhance the regenerative capacity of tissue engineering grafts by protecting encapsulated cells from ischemia.

We hypothesized that electrospinning biodegradable polymers doped with a H_2S donor (NSHD1) will generate H_2S-fibers with a controllable slow-releasing profile, which could be used as cell scaffolds to protect cell from ischemia reperfusion injury. To test this hypothesis, we fabricated H_2S-fibers by electrospinning biodegradable polycaprolactone solution containing NSHD1. The resultant H_2S-fibers not only supported the growth of cardiac myoblasts H9c2 and fibroblast NIH 3T3, but also protected cells from hydrogen peroxide (H_2O_2) induced oxidative damage by releasing H_2S. Given the broad biological functions of H_2S, we anticipate this H_2S-releasing scaffold will have great potential for biomedical applications.

4.2 RESULTS AND DISCUSSION

4.2.1 Fabrication of H₂S-fibers

Electrospinning is a simple method to generate fibrous scaffolds with diameters ranging from nanometers to microns. The generation of fibers with desired diameters highly dependent on a variety of parameters such as solution concentration, solvent vapor pressure, conductivity, surface tension, applied voltage, gap distance, and flow rate.[27] Previously, several studies have explored how different parameters affect fiber diameters.[28-30] However, results from different groups are inconsistent primarily due to differences in the control of ambient environments and home-made devices. Therefore, optimizing the electrospinning setup is essentially required before incorporating H₂S donor into fibers with desired morphology. The biodegradable polycaprolactone (PCL) is being used in the present study because it has been approved by Food Drug Administration (FDA) in specific devices used in human body for various biomedical applications and fabricated into cellular scaffolds for culturing different types of cells.[31]

In this study, by simply adjusting PCL concentrations, we fabricated various microstructures, including spheres, beaded fibers and uniform fibers using our home-made electrospinning equipment (Figure 4.1). This is consistent with previous report of the transition stage between the sphere and fiber morphologies.[32] The fine uniform fibers were eventually produced as the PCL concentration increased to 6%. Although the resulting electropining products that lack of uniform fibrous morphology cannot be used as cell scaffolds, Fattahi and colleagues had systematically investigated the drug-loading application of microspheres by encaptulating anti-tumor medicine.[33]

94
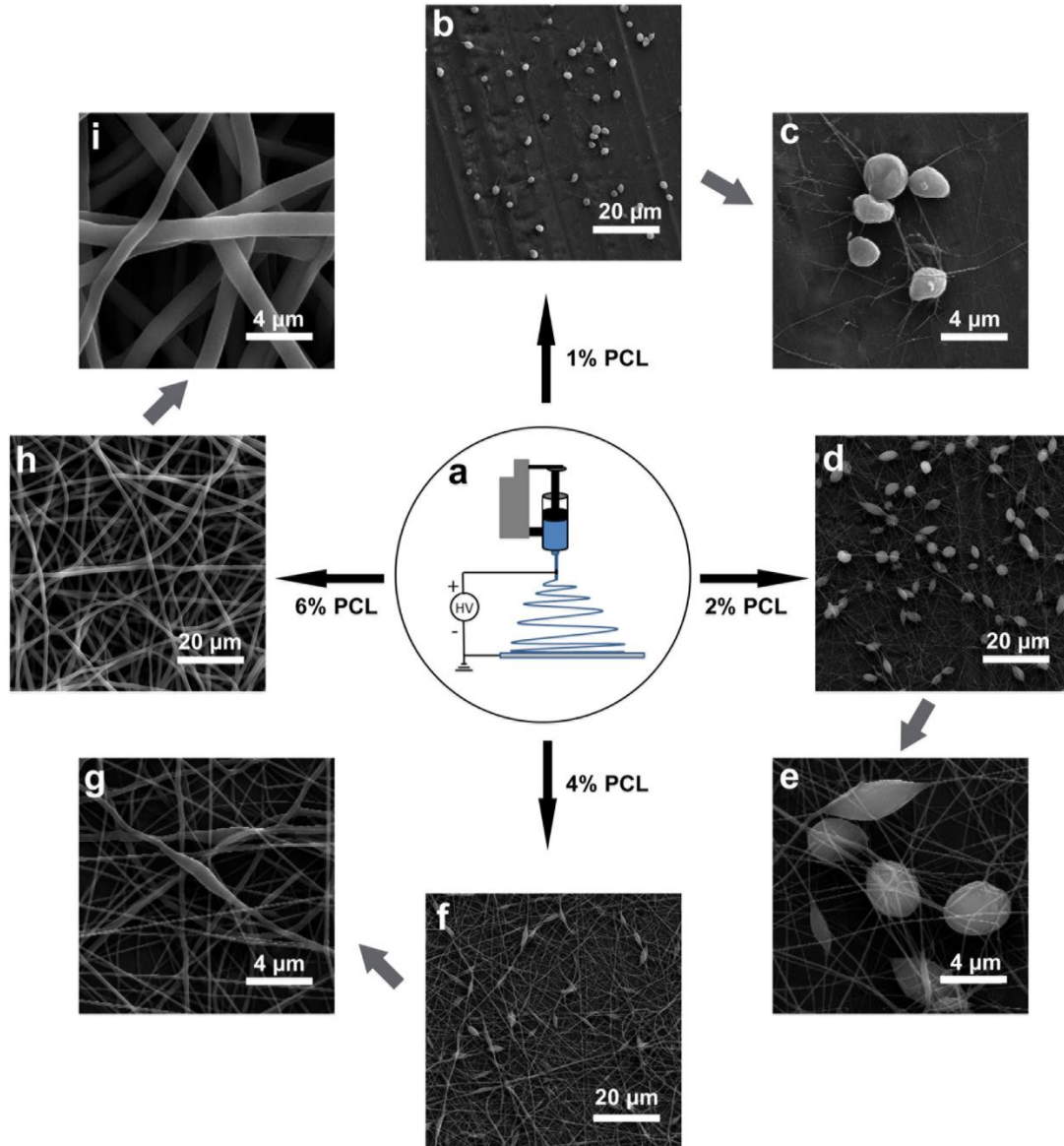
Figure 4.1. Electrospinning setup. (a) Schematic illustration of electrospinning setup. SEM images of (b) polycaprolactone (PCL) microspheres (1%), (d) microsphere/nanofiber composites (2%), (f) fibers with bead defects (4%), and (h) uniform continuous fibers (6%). (c), (e), and (f) are enlarged images of b, d, and f, respectively.

Previous studies suggest altering solution concentrations remain the most convenient and effectively way for tuning the fiber diameters.[30] In order to form uniform fine fibrous structure with different diameters, PCL solutions with concentrations ranging from 6% - 12% were prepared for electrospinning. For generating H_2S-fibers, the H_2S donor, NSHD1, was being added into each of the solutions with a constant ratio to PCL

المنارة للاستشارات

www.manaraa.com

(10 wt% with respect to PCL). The structure and activation of NSHD1 are shown in Figure 4.2g. PCL solutions with concentrations of 6%, 9%, 12% generated homogeneous fibrous scaffolds with diameters of 0.51 ± 0.16, 0.98 ± 0.16, 1.47 ± 0.18 micron, respectively (Figure 4.2a-c). In addition, the SEM images showed that H_2S donor/PCL solutions generated H_2S-fibers with uniform morphology (Figure 4.2d-f). The surfaces were smooth and no crystals were observed, which indicated that the loaded H_2S donors were evenly distributed in the fibers. The fibers formed from H_2S donor/PCL solutions have shown similar diameters as the fibers generated from PCL solution (PCL-fibers) at each of the solution concentrations (Figure 4.2h).
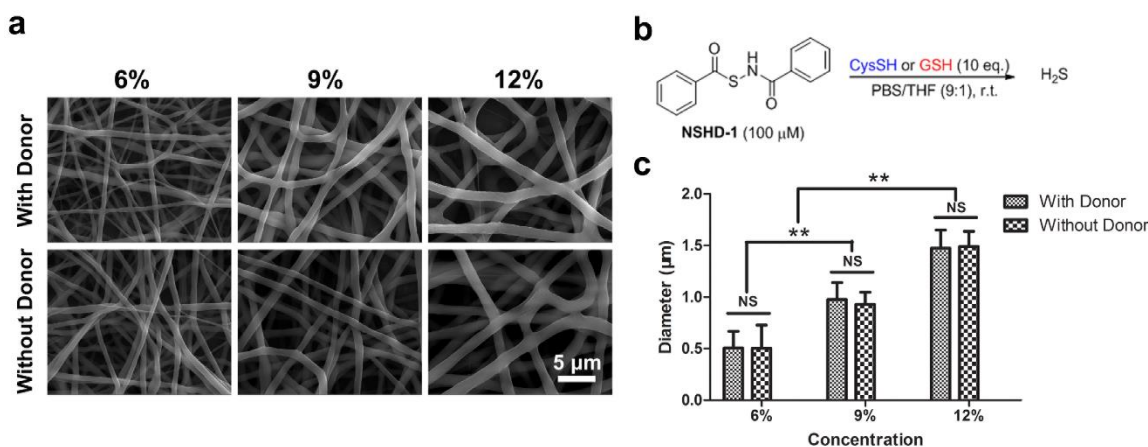
Figure 4.2. Morphology of H_2S-fibers. (a) SEM images of H_2S-fibers (Top images) and PCL-fibers (bottom images) generated from 6%, 9% and 12% w/v solutions. All images share the same scale bar as indicated in the bottom right image. (b) The H_2S donor, NSHD-1, releases H_2S in the presence of cysteine o GSH. (c) Fiber diameters plot as a function of solution concentrations. The dopant, NSHD1, has no obvious effect on fiber diameters. Data are expressed as mean $\pm$ SE, and statistical significance was assessed using two-way ANOVA. ** indicates $P < 0.05$; NS indicates not significant (n = 200).

The energy dispersive X-ray (EDX) spectra were employed to determine the presence of the H_2S donor in the fibrous matrix via detection of sulfur. The data have shown that the presence of sulfur peak in H_2S-fibers, where there is no sulfur peak in PCL-fibers (Figure 4.3a-b). Furthermore, the Fourier transform infrared spectrometry (FTIR) spectrum

96

was applied to confirm the incorporation of NSHD1 into H_2S-fibers. The FTIR spectra of PCL-fibers showed peaks located at 2945, 2866, and 1723 cm^{-1}, which were assigned to the stretching vibration of –C=O bonds (Figure 4.3c). The FTIR spectra of the H_2S-fibers showed additional absorption peaks at 3315, 1600, and 690 cm^{-1} compared with the spectra of the PCL-fibers, due to the presence of H_2S donor (Figure 4.3e). Those additional absorption peaks at 3315, 1600, and 690 cm were attributed to amide N-H stretch, amide N-H bending, and aromatic C-H bending, respectively, which matched the peaks of donor alone (Figure 4.3d). These data suggested that the donor has been successfully doped into the electrospun fibrous scaffolds.
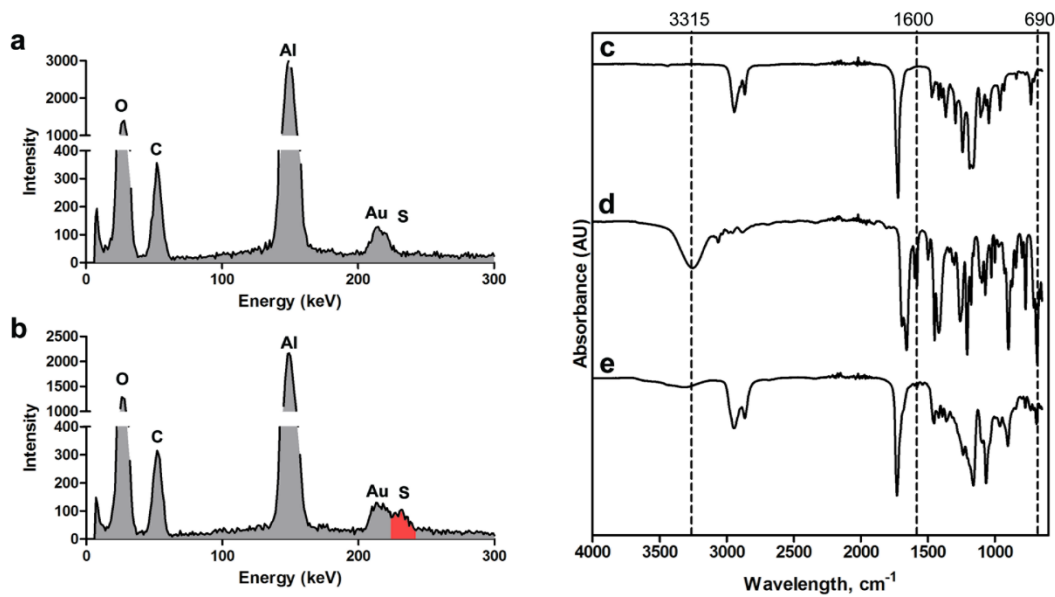
Figure 4.3. EDX and FT-IR analysis of PCL-fibers and H_2S-fibers. EDX spectrum shows the comparison between PCL-fibers (a) and H_2S-fibers (b). The red color indicates the sulfur peak. FT-IR spectrum of (c) PCL-fibers, (d) NSHD1, and (e) H_2S-fibers.

Since the alignment of various types of cells are essentially important for cells to form proper organization and fulfill biological function, such as parallel arrangement of myotubes,[34] biomaterials with anisotropic property are desired in tissue engineering.[35]

Using a homemade rotating collector, we generated aligned fibrous scaffolds by electrospinning (Figure 4.4).[36]
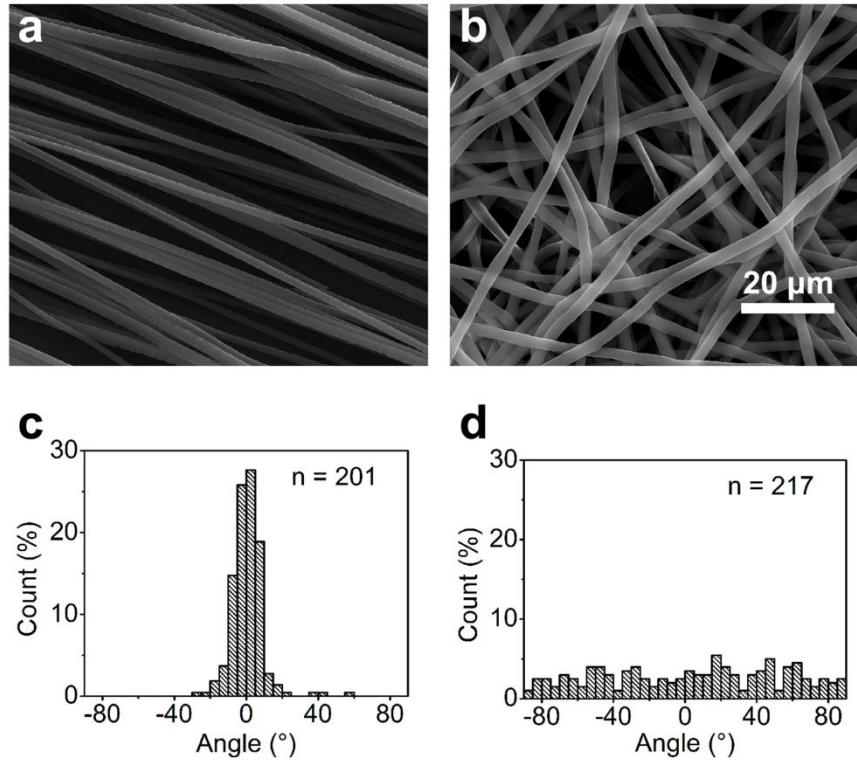
Figure 4.4. Characterization of aligned and randomly oriented H_2S-fibers. SEM imaging depicted the spatial organization of H_2S-fibers in aligned (a) and random (b) orientation. SEM images share the scale bar in (b). The distributions of the fiber orientation on aligned (c) and random fibers (d) are shown below each graph.

4.2.2 Fabrication of H_2S-fibers

H_2S has recently been recognized as an endogenously generated signaling molecule with potent cytoprotective actions.[37] Although the exact mechanism of action is still under investigation, the production of endogenous H_2S and the exogenous administration of H_2S elicit a wide range of protective actions, especially in cardiovascular systems, including vasodilation, anti-inflammatory, antioxidant, and down regulation of cellular metabolism under stress.[23, 26] Therefore fabrication of scaffolds capable of releasing H_2S release is a

promising therapeutic strategy. Here we investigated the H_2S releasing profiles of H_2S-fibers with different fiber diameters. To evaluate the rate of H_2S release from H_2S-fibers or donor alone, we measured H_2S release using two different methods: (1) instantaneous H_2S monitor with zinc acetate being added into each aliquot and (2) cumulative H_2S release with zinc acetate being added into the reacting mixture to estimate the releasing half-lives.[38]

As explained previously, our H_2S donor can be activated by biological thiols such as cysteine and GSH. The biological thiols-triggered H_2S donors enable resultant H_2S-fibers carry the advantage of controllable H_2S release. In a study of 106 healthy adults, the plasma thiols, including homocysteine, GSH, and cysteine, were about 300 to 400 μM.[39] Based on our previous study, those free thiols were able to trigger H_2S release of our donors.[10] Since the cysteine is one of the most prevail biological thiols in the plasma and gives fast activation of NSHD1, it was used as the representative activator of H_2S-fibers in the following experiments.

Before investigating the H_2S release kinetics of H_2S-fibers, we first measured the H_2S release of H_2S donor alone. As shown in a typical H_2S release curve of NSHD1 in pH 7.4 phosphate buffer (Figure 4.5a), the concentration of H_2S released from the donor reached a maximum value at 40 min (the peaking time), and then started to decreased, presumably due to volatilization, which is consistent with previously report.[10] The half-life of the donor for the pseudo-first-order kinetic plots was determined and found to be about 14 min.

Although various H_2S donors have been reported for cellular studies, the fast and uncontrollable H_2S release of those donors compromised their capacity to mimic the

99

physiological generation of H_2S. Compared with donor alone, we expect the H_2S-fibers demonstrate extended H_2S-releasing profiles. Meanwhile, since H_2S-fibers generated from 6%, 9% and 12% polymer solutions were 0.51 ± 0.16, 0.98 ± 0.16, and 1.47 ± 0.18 micron in diameter, respectively, those fibers with different diameters might give different H_2S release kinetics. As our expectation, the peaking times for H_2S-fibers generated from 6%, 9%, and 12% solutions were 120, 160, and 210 min, respectively (Figure 4.5b). The H_2S releasing half-lives of H_2S fibers from 6%, 9%, and 12% were prolonged approximately 10-50 folds, compared with donor alone. Furthermore, H_2S-fibers generated from 12% solutions demonstrated prolonged and evenly distributed H_2S release, relative to others. These data indicate that H_2S-fibers significantly prolonged H_2S release and might better mimic the biological H_2S generation.
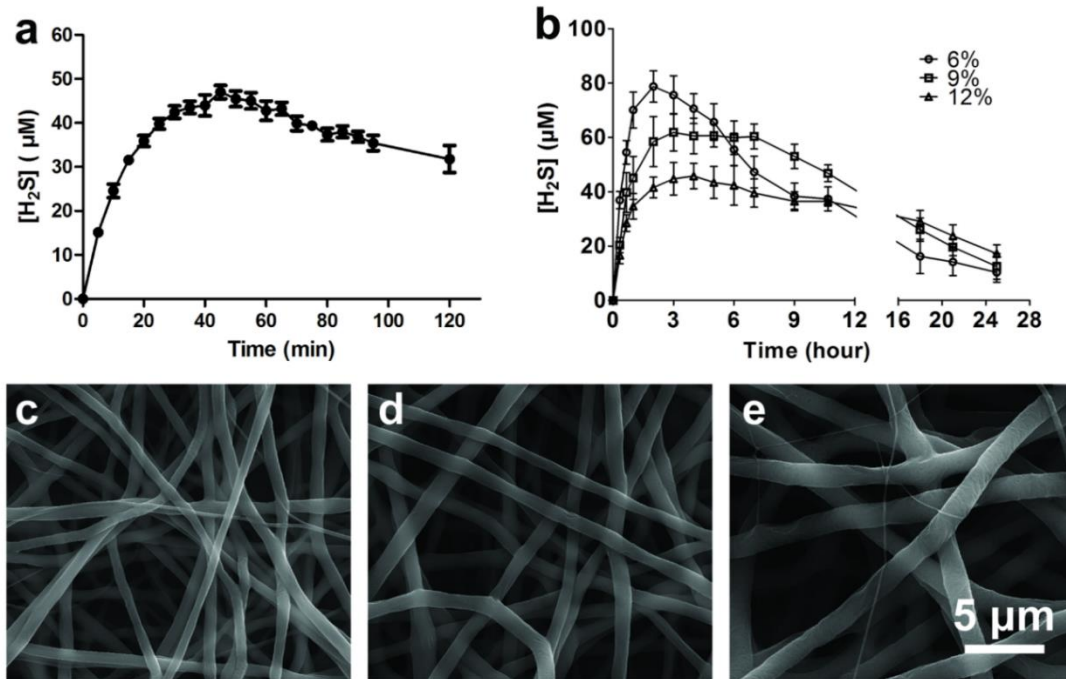
Figure 4.5. Release profiles of H_2S-fibers. (a) H_2S release kinetics of NSHD1 in the presence of 1 mM cysteine. (b) H_2S release kinetics of H_2S-fibers generated from 6%, 9% and 12% w/v H_2S donor/PCL solutions (H2S donor:PCL = 1:10). Data are expressed as mean $\pm$ SEM (n = 3). SEM images of H_2S-fibers generated from 6% (c), 9% (d) and 12% (e) w/v H_2S donor/PCL solutions after in vitro release in pH =7.4 buffer solutions for 48 h.

We next investigated the release of NSHD1 from H$_2$S-fibers. NSHD1 has a UV absorbance peak at λ_{max} = 242 nm. Thus, the amount of NSHD1 released from the fibers was determined by UV spectroscopy using a predetermined calibration curve $C = 91.5751A - 1.5833$ (R = 0.9988) where C is the concentration of NSHD1 (μM) and A is the solution absorbance at 242 nm (Figure 4.6a-b). The initial burst release followed by the relatively steady release was observed. The burst release was attributed to release of NSHD1 from a superficial area of the electrospun fibers. The smaller diameter fibers exhibited higher burst release feature, which is consistent with previous study.[40] After the initial burst release, the NSHD1 release of 12% H$_2$S-fibers were slower than 6% and 9% H$_2$S-fibers (Figure 4.6b). This is due to that the larger diameter of 12% H$_2$S-fibers make the drug harder to diffuse from the interior of the fibers compared to others. In addition, the higher specific surface areas of 6% and 9% H$_2$S-fibers are beneficial to drug release. After first 24 hours, the NSHD1 release of all H$_2$S-fibers reached plateau and in the next 70 hours (Figure 4.6c), the NSHD1 concentration slowly reduced, this might be due to the hydrolysis of the NSHD1, which has been reported in another H$_2$S donor with similar structure.[38]

H$_2$S-Release capacity of NSHD1 were significantly reduced upon being loaded into fibers. This might be due to multiple reasons. First of all, the high voltages might lead to partially degradation of NSHD1. Secondly, the accessibility of NSHD1 towards the activator (cysteine) were influenced after doped into fibers. Thirdly, when we measured the release kinetics in vitro, the oxidation of the activator would also affect the release kinetics. Further investigation needs to be done to address the loading efficiency of NSHD1 in detail.
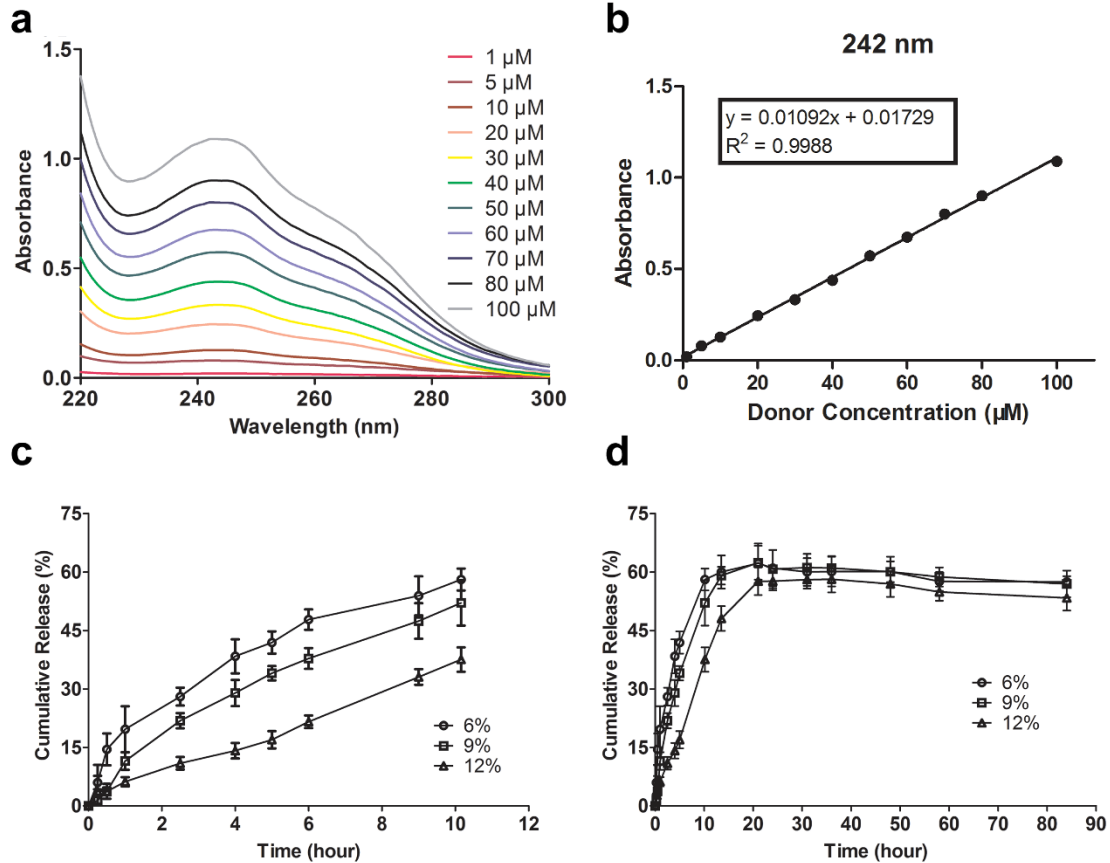
Figure 4.6. Cumulative Release of H$_2$S Donors from H$_2$S-fibers. (a) UV absorbance of NSHD1 in various concentrations PBS solutions (1 – 100 μM). (b) Linear regression analysis the donor concentration vs absorbance. (c) Cumulative release of NSHD1 from H2S-fibers in first 10 hours. (d) Cumulative release of NSHD1 from H$_2$S-fibers over 85 hours. All data were expressed as mean $\pm$ SEM (n = 3).

After 48 h incubation in PBS at pH 7.4 with excess of cysteine, the H$_2$S fibers were subjected to SEM imaging. Compared with the original formation, the fibrous structure of electrospun fibrous scaffolds maintained a 3D fibrous morphology, albeit all the fibers shown slightly swollen (Figure 4.5c-e). This might be because of the chain relaxation of the matrix polymer after incubation in the PBS. Since all the fibrous scaffolds remained stable and maintained the 3D structural feature, the fibrous scaffolds can be applied as tissue engineering scaffolds to support the proliferation of cells after releasing H$_2$S.

Since 12% solution containing the H$_2$S donor generates 1.5 micron H$_2$S-fibers with prolonged and evenly distributed H$_2$S release. For the cell experiments, 12% polymer solution was chosen for the fabrication of H$_2$S-fibers. In addition, the aligned H$_2$S-fibers have shown similar release kinetics to random H$_2$S-fibers. The aligned fibers have been reported to promote cells alignment to potentiate their anisotropic properties. Thus H$_2$S-fibers with aligned orientation were applied for further investigation of cytoprotection.

4.2.3 Cytocompatibility of H$_2$S-fibers

With these H$_2$S-fibers in hand, we next explored their cytocompatibility. Previous studies revealed H$_2$S protects cardiac cells from myocardial ischemia reperfusion injury.[40-41] In an *in vitro* model of cutaneous tissue transplantation, H$_2$S significantly decreased apoptosis of fibroblasts caused by ischemia reperfusion injury.[42] Given the potential applications of H$_2$S-fibers in those scenarios, H9c2 cardiac myoblasts and NIH 3T3 fibroblasts were chosen as the representatives for the cytocompatibility test.

Before investigating cytocompatibility of H$_2$S-fibers, we first tested cytotoxicity of NSHD1 to H9c2 cardiomyoblasts. NSHD1 did not exhibit significant cytotoxicity at low concentrations (< 40 μM). However, the cytotoxicity was observed when higher concentrations (> 80 μM) of NSHD1 were applied. After H9c2 cells were incubated with NSHD1 (160 μM) in the presence of cysteine (480 µM), NSHD1's cytotoxicity was completed suppressed (Figure 4.7). Considering that cysteine and GSH are relative rich in living systems, we envision NSHD-induced cytotoxicity could be diminished or avoid.

To investigate cytocompatibility of H$_2$S-fibers, H9c2 and NIH 3T3 cells were cultured in H$_2$S-fibers for 24 hours and subsequently examined by CellTiter-Blue assay. We observed 50% reduction of cell viability for H9c2 cells cultured on H$_2$S-fibers

103

compared to PCL-fibers, when no cysteine were added into the culture medium (Figure 4.8a). Interestingly, we did not observe cytotoxicity towards NIH 3T3 cells (Figure 4.8b). However, when being cultured in medium containing 250 μm cysteine, both H9c2 and NIH 3T3 cells on H_2S fibers maintained similar viability with cells on PCL-fibers (Figure 4.8). These data demonstrated that our H_2S fibers were non-toxic to cells in the presence of biological thiols. Given that the concentration of biological thiols including cysteine, homocysteine, and GSH, is ranging from several hundred micromolar to several milimolar *in vivo*,[39] H_2S-fibers should be non-toxic to cells and tissues when they are being used as an implanted scaffolds.
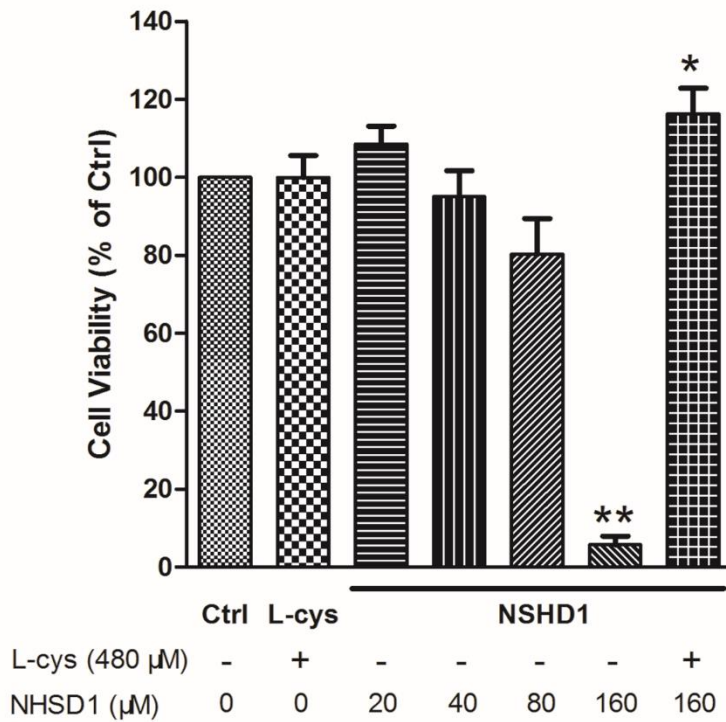

Figure 4.7. Cytotoxicity of NSHD1 in the absence or presence of cysteine. Data were expressed as the mean ±SEM. * indicates P < 0.05 vs. Control (Ctrl). ** indicates *P* < 0.01 vs. Ctrl.
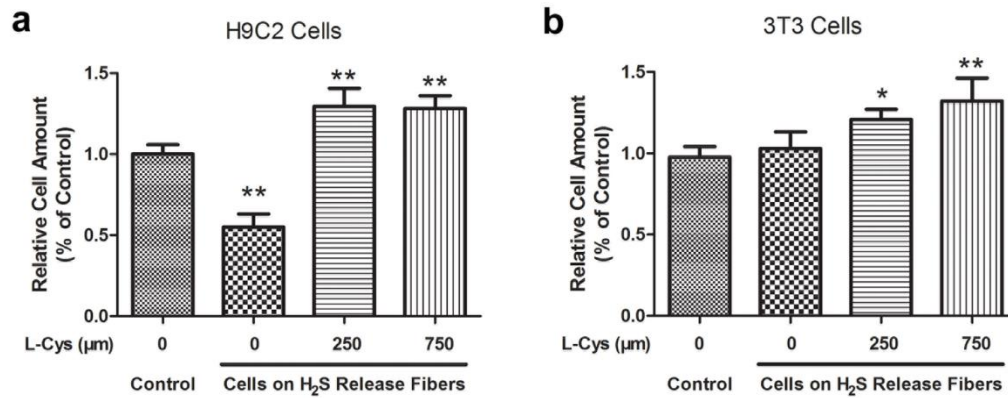
Figure 4.8. Effects of H$_2$S-fibers on cell viability. NIH 3T3 cells. (a) and H9c2 cells (b) were cultured in fibrous scaffolds in presence of cysteine at indicated amount for 24 hours. CellTiter-Blue assay was performed to measure cell viability. Data were expressed as the mean $\pm$ SEM (n = 6). * indicates $P < 0.05$ vs. Control group (cells in PCL fibers). ** indicates $P < 0.01$ vs. Control group.

To observe cells in H$_2$S-fibers, H9c2 cells cultured in the fibrous scaffolds at day 1, day 3, and day 5 were stained with phalloidin and DAPI, then observed under fluorescence microscopy (Figure 4.9). The aligned fibers promoted H9c2 to align along the fiber axis. Previous research suggested that this guided alignment could strongly promote myoblasts formation.[43] In addition, H9c2 cells increased in number during cultured in H$_2$S-fibers. At day 3 and day 5, H9c2 were found to reach an estimated confluence of 50% and 90%, respectively, indicating that H9c2 proliferated in H$_2$S-fibers. In addition, we did not observe morphological changes of the cells in H$_2$S-fibers. Similar results were observed in H9c2 cells cultured in PCL-fibers (Figure 4.10). Taken together, we conclude that H$_2$S fibers are cytocompatible and can support the cell proliferation.

105
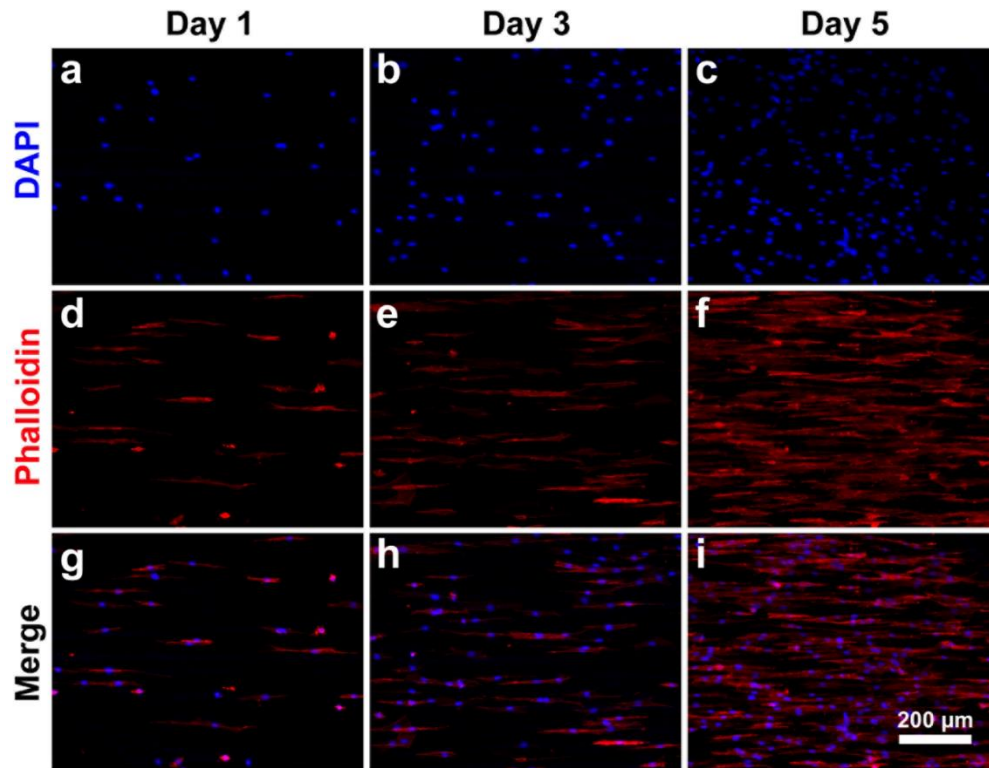
Figure 4.9. Fluorescence images of H9c2 cells cultured in H$_2$S-fibers. H9c2 cells were cultured in aligned fibrous scaffolds for 5 days. In each time point samples were fixed and stained by Phalloidin (red) and DAPI (blue). Images were taken with fluorescence microscope. All images share the scale bar in (i).

Figure 4.10. Fluorescence images of H9c2 cells cultured in H$_2$S-fibers and PCL-fibers. H9c2 cells were seeded in fibrous scaffolds for 1 day. Then samples were fixed and stained by Phalloidin (red) and DAPI (blue). Images were taken with fluorescence microscope. All images share the scale bar in (f).
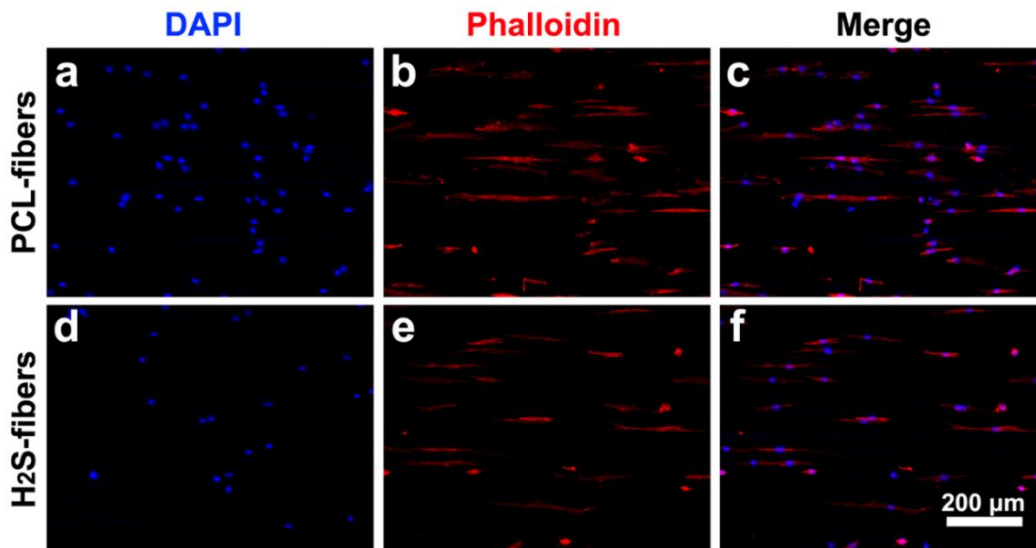
106

4.2.4 H₂S-fibers Protecting Cells from Oxidative Damage

After examining the cytocompatibility of cells with H$_2$S-fibers, we then used a selective H$_2$S probe, WSP-5,[44] to monitor the H$_2$S in cells cultured in H$_2$S-fibers. H9c2 cells and NIH 3T3 cells were seeded in the H$_2$S-fibers for 12 hours in the presence of 250 μM cysteine. Then WSP-5 was applied to monitor the intracellular H$_2$S. As expected, cells in H$_2$S-fibers showed enhanced fluorescent signals compared to cells in PCL-fibers (Figure 4.11). The H$_2$S signal could be observed even after 24 hours of incubation (Data not shown), indicating a sustained release of H$_2$S from H$_2$S-fibers.
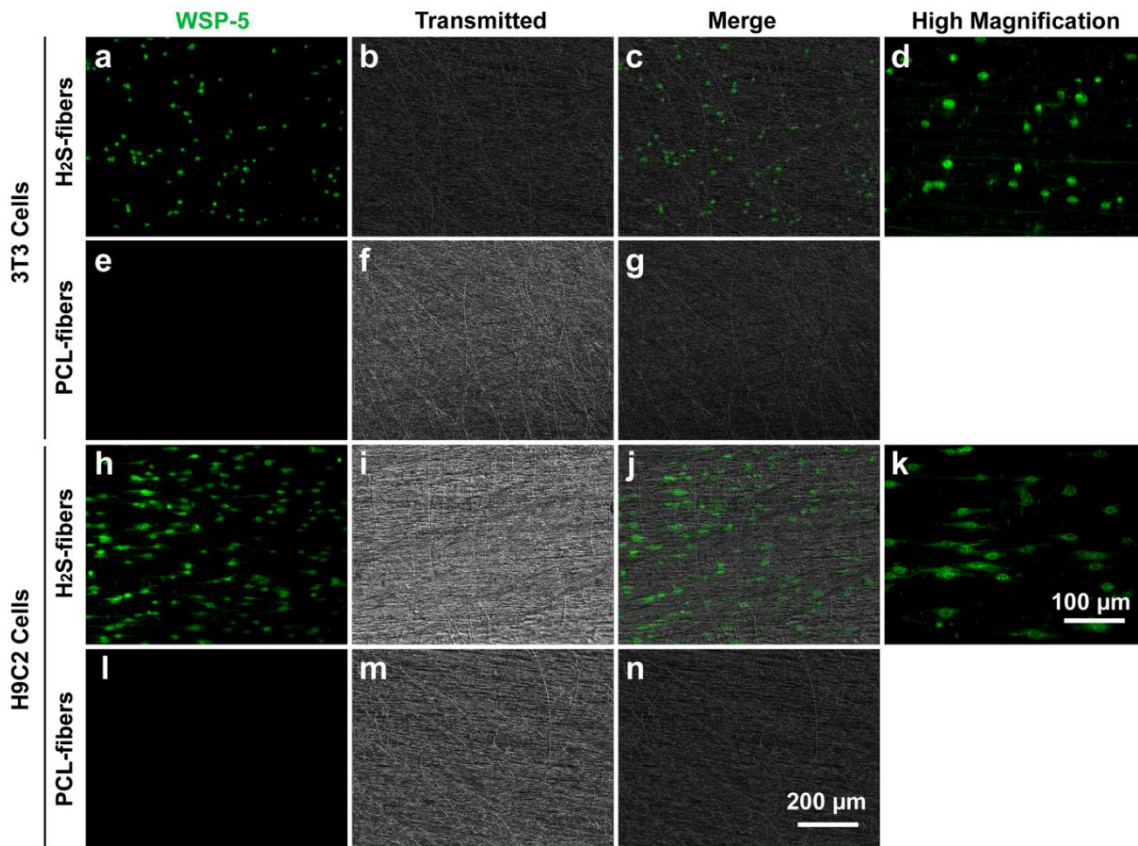
Figure 4.11. H$_2$S detection in NIH 3T3 cells and H9c2 cells. NIH 3T3 (top 2 rows) and H9c2 cells (bottom two rows) were cultured on H$_2$S-fibers (first and third rows) or PCL-fibers (second and last rows) for 12 hours, 100 μM of a H$_2$S fluorescent probe (WSP-5, green channel) was used to detect H$_2$S production in cells. (d) and (k) are higher magnification view of (a) and (h), respectively. (a-c), (e-g), (h-j), and (l-n) share the scale bar as in (n). (d) and (k) share the scale bar as in (k).
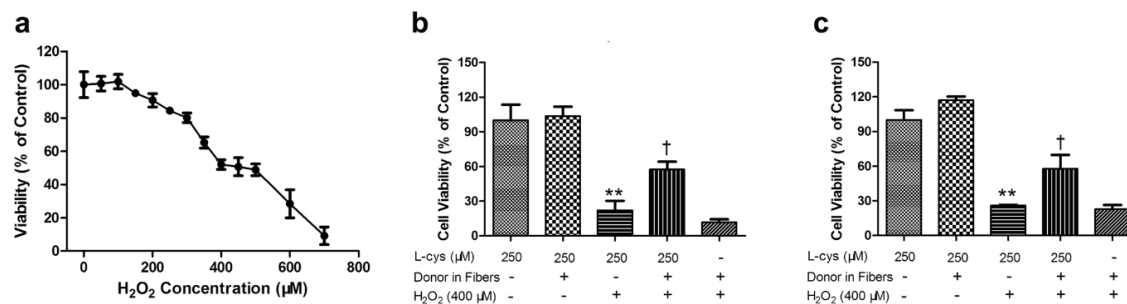
Figure 4.12. H_2S-fibers protected cells from H_2O_2 induced oxidative injury. (a) H9c2 cells were treated with H_2O_2 at indicated concentrations for 24 h. Before treated with 400 M H_2O_2 for 24 h, H9c2 (b) and NIH 3T3 (c) were cultured in either PCL-fibers (Donor -) or H_2S-fibers (Donor +) with or without 250 M cysteine. Cell viability was measured by CellTiter-Blue assay. Data were shown as the mean ± SEM. ** indicates $P<0.01$ vs. Control group (cells in PCL-fibers without H_2O_2 treatment). † indicates $P<0.01$ vs. cells in PCL-fibers with H_2O_2 treatment group.

A previous study revealed that H_2O_2 is a major player in ischemia reperfusion injury, and ischemia causes a dramatic increase of myocardial H_2O_2 content.[45] Therefore, H_2O_2 has been applied to H9c2 cells as an *in vitro* ischemia model.[46] Recent studies suggested H_2S holds a great potential in protecting cells from ischemia reperfusion injury. To test the biological function of our H_2S-fibers, we evaluated the cytoprotective effect of H_2S-fibers against H_2O_2 induced oxidative damage. We first exposed H9c2 cells to H_2O_2 in a range of 0 to 1000 μM for 24 h in serum free medium. The CellTiter-Blue assay was performed to determine the viability of H9c2 cells treated by H_2O_2. A dose-dependent loss of cell viabilities was observed in H9c2 with concentrations between 100 to 700 μM (Figure 4.12a). A concentration of 400 μM of H_2O_2 that could reduce 50% of cell viability was chosen for later studies. The H9c2 cells and NIH 3T3 cells were seeded in H_2S fibers or PCL fibers for 24 hours with 250 μM cysteine. Then cells in the fibers were switched into serum free medium containing 400 μM H_2O_2 for 24 hours. The cell viabilities were measured by CellTiter-Blue assay. Our data demonstrated that viabilities of cells in H_2S fibers were significantly higher than ones in PCL-fibers. However, if there was no extra

108

cysteine being added in the culture medium, the cytotoxicity of H_2S-fibers synergized the effect of H_2O_2 to further decrease the cell viabilities (Figure 4.12b-c). Interestingly, the cells on 3D fibrous scaffolds were more sensitive to H_2O_2 treatment than cells on tissue culture plastics, probably due to the alteration of culture dimensions.[47] The protective effect of H_2S fibers were observed up to 36 hours and disappeared at 48 hours (Figure 4.13).
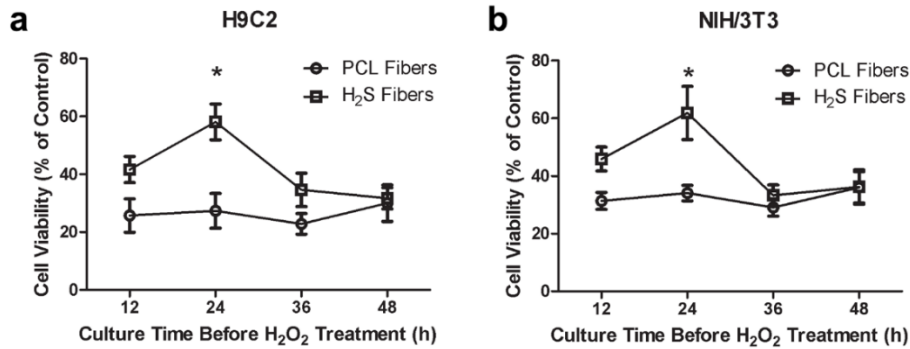
Figure 4.13. Time course of H_2S-fibers protecting cells from H_2O_2 induced oxidative injury. H9c2 cells (a) and NIH/3T3 cells (b) were cultured on H_2S-fibers of PCL-fibers with 250 M cysteine for indicated time. And then cells were subject 400 M H_2O_2 for 24 h. Cell viability was measured by CellTiter-Blue assay and then normalized by the viability of cells on PCL-fibers without H_2O_2 treatment. Data were shown as the mean $\pm$ SEM (n = 4). * indicates $P<0.01$.
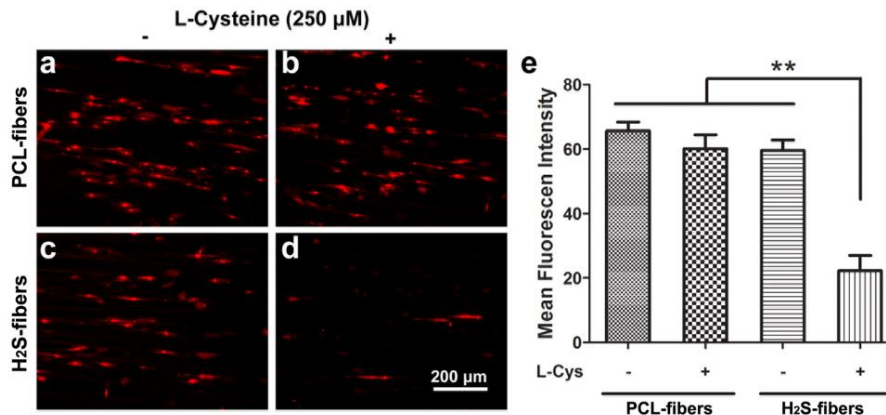
Figure 4.14. H_2S-fibers reduced levels of reactive oxygen species (ROS) production in H_2O_2 treated H9c2 cells. Representative images of DHE-fluorescence intensity were taken 2 h after H_2O_2 treatment for cells in PCL-fibers (a-b) or H_2S-fibers (c-d) with (right column) or without 250 μM (left column) cysteine. (e) H_2S-fibers significantly decreased DHE-fluorescence intensity in H9c2 cells in presence of 250 μM cysteine compared to other group (n = 20). Data were expressed as the mean $\pm$ SEM. ** indicates $P < 0.01$.

109

Increased generation of reactive oxygen species (ROS) during both ischemia and reperfusion plays an essential role in the pathophysiology of intraoperative myocardial injury.[48] Cardioprotective effect of H_2S during ischemia reperfusion results from decreasing the levels of ROS production.[49] To confirm that our H_2S fibers have the cytoprotective function, we investigated the ROS production of H9c2 cells in H_2S-fibers or PCL-fibers under H_2O_2 treatment. After 2 hours of exposure to H_2O_2, the ROS generation was measured using live cell imaging with a ROS probe, dihydroethidium (DHE).[50] The intracellular fluorescence intensity in the nuclei, which reflected ROS generation, was significantly lower for cells cultured in H_2S-fibers with 250 μM cysteine than counterparts in PCL-fibers and H_2S-fibers without cysteine (Figure 4.14). In a control study performed in tissue culture plastics, H9c2 cells pretreated with 160 μM NSHD1 and 480 μM cysteine showed significantly decreased DHE fluorescence signal after 2 h exposure to 400 μM H_2O_2, compared to cells without pretreatment (Figure 4.15). These data suggest that our H_2S-fibers can effectively protect cells from H_2O_2 induced oxidative injury by releasing H_2S.
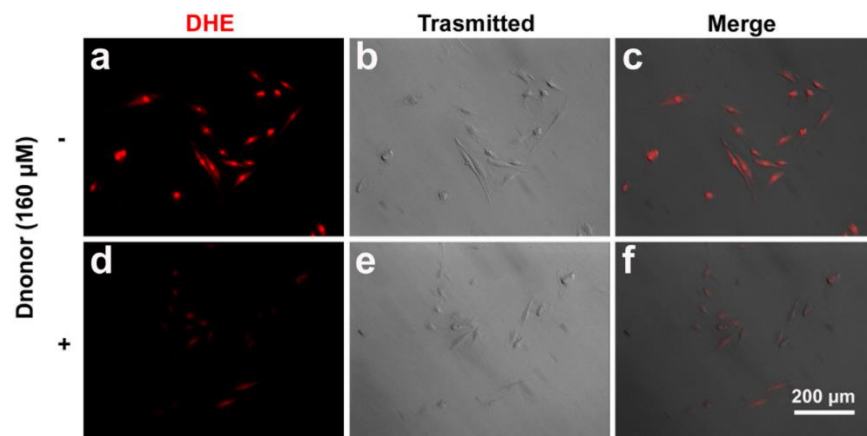

Figure 4.15. H_2S donor, NHSD1, prevents H_2O_2 induced ROS production in H9c2 cells. Cells pre-treated with 160 μM NHSD1. (c-e) showed significant reduction of DHE fluorescence signal compared to cells without pre-treatment (a-c). All images share the scale bar in (f).

110

4.3 CONCLUSIONS

Hydrogen sulfide has been gaining increasing attentions recently due to its broad range of biological functions. Here, combining electrospinning technique with a H_2S donor, we generated fibrous scaffolds with controllable H_2S release. By adjusting fiber diameters, tunable H_2S releasing profiles have been achieved. Compared to donor alone, H_2S-fibers have demonstrated prolonged and evenly distributed H_2S release. Furthermore, we investigated the cytoprotective effects of H_2S-fibers against H_2O_2 induced cell injuries. Our data demonstrated that H_2S-fibers released H_2S to the cells and significantly decreased ROS production in H_2O_2 treated cells, thus protecting cells from H_2O_2 induced oxidative damage. Therefore, we anticipate that our H_2S-fibers could be potentially used in cardiovascular tissue engineering and a broad range of other biomedical applications.

4.4 EXPERIMENTS

4.4.1 Electrospinning of H₂S-releasing Fibers

Poly(ε-caprolactone) (PCL) (Average Mn ca. 70-90 kDa, Sigma) were dissolved in 1,1,1,3,3,3-hexafluro-2-propanol (HFIP) (Sigma Aldrich) to obtain 1 to 12% w/w solutions. For samples containing dopant, the polymer was dissolved in HFIP first, followed by the addition of NSHD1. Each polymer solution was drawn into fibers by a home-made electrospinning system described before.[51] Briefly, the polymer solution was transferred to a 1.0 mL plastic syringe (BD) with a 21 G blunt needle (BD precision glide). A syringe driver was used to control the solution flow rate at 15 μL min^{-1}. A high voltage supply (HVR Orlando, FL) was used to build up a voltage of 6-7 kV electric field between the needle and the grounded collector. The distance between the collector and needle was fixed at 10 cm. The temperature of the electrospinning environment was 25 °C, and the

111

humidity was below 1%. The random fibers were obtained by using a stationary collector. And the aligned fibers were obtained by using a rotating drum (12 cm in diameter) as the collector. The rotating rate was 1000 revolutions per minute.

4.4.2 Fiber Analysis

The morphology of PCL fibrous scaffolds and elemental analysis via EDX were examined by a scanning electron microscopy (SEM, Zeiss Ultra Plus FESEM). Fibrous scaffolds samples were dried with nitrogen, and coated with gold for 40 seconds with Desk II cold sputter coater (Denton Vacuum, Morristown, NJ). To examine the uniformity of the fibrous diameters, several randomly selected areas were imaged. The same condition was used for EDX. Fibrous diameters were measured using ImageJ (National Institutes of Health). Fourier transform infrared spectrometry (FTIR) was conducted on a Shimadzu 8400 FTIR spectrometer in the range of 500-4000 cm^{-1}.

4.4.3 Hydrogen Sulfide Release

Reactions for the measurement of H_2S release kinetics were run in triplicate. In each test, 50 mg fibers samples were immersed in 50 mL PBS (pH 7.4). Reaction aliquots (1.0 mL) were taken to UV-Vis cuvettes containing zinc acetate (100 μL, 1% w/v in H_2O), $FeCl_3$ (200 μL, 30 mM in 1.2 M HCl), and *N,N*-dimethyl-1,4-phenylenediamine sulfate (200 μL, 20 mM in 7.2 M HCl) at predetermined time points. Absorbance at 670 nm was measured 20 min thereafter. H_2S concentrations were calculated according to the Na_2S standard curve. To determine the release half-life, 1% w/v zinc acetate was added to the 50 mL PBS containing 50 mg fibers sample. Then reaction aliquots were taken to UV-Vis cuvettes containing $FeCl_3$ (200 μL, 30 mM in 1.2 M HCl), and *N,N*-dimethyl-1,4-phenylenediamine sulfate (200 μL, 20 mM in 7.2 M HCl) at predetermined time points.

112

First-order half-life of H$_2$S release was determined by plotting time vs. ln(1/(1-% released), with t$_{1/2}$ = ln(2)/slope.

4.4.5 Cell Lines and Cell Cultures

The rat cardiomyocyte cell line H9c2 and the immortalized mouse fibroblast cell line NIH 3T3 were purchased from American Type Culture Collection. Both cell lines were maintained in Dulbecco's modified Eagle's medium (DMEM, #D6046, Sigma–Aldrich) supplemented with 10% heat inactivated fetal bovine serum (Hyclone, Thermo Scientific), 100 U mL^{-1} penicillin and 100 μg mL^{-1} streptomycin (Gibco BRL, Invitrogen Corp., Carlsbad, CA, USA). Cells were cultured in a 5% CO$_2$ humidified incubator at 37 ℃. Sterilized PCL fibrous scaffolds were soaked in media 30 min prior cell seeding. Cells in exponential growth phase were trypsinized by 0.25% trypsin and seeded on PCL fibrous scaffold at a density of 5.2 × 10^3 cells per cm^2.

4.4.6 Cell Viability Assay

Cells growing exponentially were trypsinized and seeded in fibrous scaffolds in triplicate wells. After 24 hours, the cell viability was analyzed by CellTiter-Blue^{TM} Cell Viability Assay (Promega, Madison, WI). The CellTiter-Blue reagent was added to the medium directly (100 μL per 1 mL medium) and incubated for four hours at 37°C. Fluorescence at 560ex/590em nm filter setting was measured using a Tecan infinite M200 plate reader (Tecan, Salzburg, Austria). After correction of background fluorescence, the intensity of fluorescence for each sample was normalized by the control. For the assessment of protective effects of H$_2$S-fibers against oxidative damage, cells were seeded on fibrous scaffolds with medium containing 250 μM L-Cysteine for predetermined time

113

points, then subjected to 400 μM H_2O_2 treatment for 24 hours. After this, CellTiter-Blue was applied to determine the cell viability.

4.4.7 Fluorescence Microscopy

Cells growing exponentially were trypsinized and seeded in fibrous scaffolds. At predetermined time points, cells were rinsed with phosphate buffered saline (PBS) twice and fixed with 4% paraformaldehyde for 20 min at room temperature. Scaffolds with cells were rinsed with PBS. Cells were permeabilized with 0.2% Triton X100 for 10 min. To prevent non-specific labeling, 3% bovine serum albumin (BSA) in PBS were applied as a blocking buffer for 20 min. Actin cytoskeleton was stained with Rhodamine Phalloidin (Cytoskeleton Inc.) (1:200) in a blocking buffer for 20 min, and nuclei were stained with 4',6-diamidino-2-phenylindole (DAPI) (Invitrogen) in a blocking buffer for 10 min. The fluorescence was visualized and captured under confocal microscope (Olympus IX81) with DAPI filter and Cy3 filter set.

4.4.8 Detection of H_2S in Cells

H9c2 and NIH 3T3 cells were seeded on fibrous scaffolds for 12 hours. The cells were then incubated with a H_2S probe (WSP-5)[44] solution (250 μM in PBS) and surfactant CTAB (500 μM) in PBS at 37 °C for 30 min. After the PBS was removed, the fluorescence signal was observed by confocal microscope (Olympus IX81) with Cy5 filter.

4.4.9 Reactive Oxygen Species Detection

H9c2 cells were seeded in fibrous scaffolds for 24 hours, then treated with 400 μM H_2O_2 for 2 hours. Dihydroethidium (DHE, Invitrogen) staining was applied to quantify ROS production. Cells were incubated with 10 μM DHE for 30 min at 37 °C. Images were

114

obtained using confocal microscope (Olympus IX81) with Cy3 filter. The fluorescent intensity of the nuclei was measured in each field by ImageJ.

4.4.10 Statistical analysis:

All assays were performed in triplicates unless otherwise stated. Data are indicated as mean $\pm$ SEM. Comparisons were done using one-way ANOVA unless otherwise stated. All the statistical analyses were done by GraphPad Prism.

4.5 REFERENCE

1.   Abe, K.; Kimura, H. The possible role of hydrogen sulfide as an endogenous neuromodulator. *J Neurosci* **1996,** *16* (3), 1066-71.

2.   Li, L.; Rose, P.; Moore, P. K. Hydrogen Sulfide and Cell Signaling. *Annual Review of Pharmacology and Toxicology* **2011,** *51* (1), 169-87.

3.   Meister, A.; Fraser, P. E.; Tice, S. V. Enzymatic Desulfuration of Beta-Mercaptopyruvate to Pyruvate. *J Biol Chem* **1954,** *206* (2), 561-75.

4.   Cavallini, D.; Mondovi, B.; De Marco, C.; Scioscia-Santoro, A. The mechanism of desulphhydration of cysteine. *Enzymologia* **1962,** *24*, 253-66.

5.   Braunste.Ae; Goryache.Ev; Tolosa, E. A.; Willhard.Ih; Yefremov.Ll. Specificity and Some Other Properties of Liver Serine Sulphhydrase: Evidence for Its Identity with Cystathionine Beta-Synthase. *Biochim Biophys Acta* **1971,** *242* (1), 247-60.

6.   Whiteman, M.; Le Trionnaire, S.; Chopra, M.; Fox, B.; Whatmore, J. Emerging role of hydrogen sulfide in health and disease: critical appraisal of biomarkers and pharmacological tools. *Clin Sci (Lond)* **2011,** *121* (11), 459-88.

7.   Lefer, D. J. A new gaseous signaling molecule emerges: cardioprotective role of hydrogen sulfide. *Proc Natl Acad Sci U S A* **2007,** *104* (46), 17907-8.

8.   Song, Z. J.; Ng, M. Y.; Lee, Z. W.; Dai, W.; Hagen, T.; Moore, P. K.; Huang, D.; Deng, L. W.; Tan, C. H. Hydrogen sulfide donors in research and drug development. *Medchemcomm* **2014,** *5* (5), 557-70.

9.   Hasegawa, U.; van der Vlies, A. J. Design and synthesis of polymeric hydrogen sulfide donors. *Bioconjug Chem* **2014,** *25* (7), 1290-300.

10.   Zhao, Y.; Wang, H.; Xian, M. Cysteine-activated hydrogen sulfide (H2S) donors. *J Am Chem Soc* **2011,** *133* (1), 15-7.

11.   Venugopal, J.; Low, S.; Choon, A. T.; Ramakrishna, S. Interaction of cells and nanofiber scaffolds in tissue engineering. *J Biomed Mater Res B Appl Biomater* **2008,** *84* (1), 34-48.

12.   Liu, W.; Thomopoulos, S.; Xia, Y. Electrospun nanofibers for regenerative medicine. *Adv Healthc Mater* **2012,** *1* (1), 10-25.

13.   Chen, M.; Li, Y. F.; Besenbacher, F. Electrospun Nanofibers-Mediated On-Demand Drug Release. *Adv Healthc Mater* **2014,** *3*(11), 1721-32.

14.   Casper, C. L.; Yamaguchi, N.; Kiick, K. L.; Rabolt, J. F. Functionalizing electrospun fibers with biologically relevant macromolecules. *Biomacromolecules* **2005,** *6* (4), 1998-2007.

15.   Nie, H.; Soh, B. W.; Fu, Y. C.; Wang, C. H. Three-dimensional fibrous PLGA/HAp composite scaffold for BMP-2 delivery. *Biotechnol Bioeng* **2008,** *99* (1), 223-34.

16.   Eap, S.; Becavin, T.; Keller, L.; Kokten, T.; Fioretti, F.; Weickert, J. L.; Deveaux, E.; Benkirane-Jessel, N.; Kuchler-Bopp, S. Nanofibers Implant Functionalized by Neural Growth Factor as a Strategy to Innervate a Bioengineered Tooth. *Advanced Healthcare Materials* **2014,** *3* (3), 386-91.

17.   Luu, Y. K.; Kim, K.; Hsiao, B. S.; Chu, B.; Hadjiargyrou, M. Development of a nanostructured DNA delivery scaffold via electrospinning of PLGA and PLA-PEG block copolymers. *J Control Release* **2003,** *89* (2), 341-53.

18.   Coneski, P. N.; Nash, J. A.; Schoenfisch, M. H. Nitric Oxide-Releasing Electrospun Polymer Microfibers. *ACS Applied Materials & Interfaces* **2011,** *3* (2), 426-32.

117

19.   Koh, A.; Carpenter, A. W.; Slomberg, D. L.; Schoenfisch, M. H. Nitric Oxide-Releasing Silica Nanoparticle-Doped Polyurethane Electrospun Fibers. *ACS Applied Materials & Interfaces* **2013,** *5* (16), 7956-64.

20.   Wold, K. A.; Damodaran, V. B.; Suazo, L. A.; Bowen, R. A.; Reynolds, M. M. Fabrication of biodegradable polymeric nanofibers with covalently attached NO donors. *ACS Appl Mater Interfaces* **2012,** *4* (6), 3022-30.

21.   Bohlender, C.; Wolfram, M.; Goerls, H.; Imhof, W.; Menzel, R.; Baumgaertel, A.; Schubert, U. S.; Mueller, U.; Frigge, M.; Schnabelrauch, M.; Wyrwa, R.; Schiller, A. Light-triggered NO release from a nanofibrous non-woven. *J Mater Chem* **2012,** *22* (18), 8785-92.

22.   Liu, H. A.; Balkus, K. J. Novel Delivery System for the Bioregulatory Agent Nitric Oxide. *Chem Mater* **2009,** *21* (21), 5032-41.

23.   Olson, K. R. The therapeutic potential of hydrogen sulfide: separating hype from hope. *Am J Physiol-Reg I* **2011,** *301* (2), R297-R312.

24.   Hsiao, S. T.; Dilley, R. J.; Dusting, G. J.; Lim, S. Y. Ischemic preconditioning for cell-based therapy and tissue engineering. *Pharmacol Therapeut* **2014,** *142* (2), 141-53.

25.   Foley, D. P.; Chari, R. S. Ischemia-reperfusion injury in transplantation: novel mechanisms and protective strategies. *Transplantation Reviews* **2007,** *21* (1), 43-53.

26.   Whiteman, M.; Moore, P. K. Hydrogen sulfide and the vasculature: a novel vasculoprotective entity and regulator of nitric oxide bioavailability ? *J Cell Mol Med* **2009,** *13* (3), 488-507.

27.   Thompson, C. J.; Chase, G. G.; Yarin, A. L.; Reneker, D. H. Effects of parameters on nanofiber diameter determined from electrospinning model. *Polymer* **2007,** *48* (23), 6913-22.

28.   Theron, S. A.; Zussman, E.; Yarin, A. L. Experimental investigation of the governing parameters in the electrospinning of polymer solutions. *Polymer* **2004,** *45* (6), 2017-30.

29.   Tan, S. H.; Inai, R.; Kotaki, M.; Ramakrishna, S. Systematic parameter study for ultra-fine fiber fabrication via electrospinning process. *Polymer* **2005,** *46* (16), 6128-34.

30.   Beachley, V.; Wen, X. Effect of electrospinning parameters on the nanofiber diameter and length. *Materials Science and Engineering: C* **2009,** *29* (3), 663-8.

31.   Cipitria, A.; Skelton, A.; Dargaville, T. R.; Dalton, P. D.; Hutmacher, D. W. Design, fabrication and characterization of PCL electrospun scaffolds-a review. *J Mater Chem* **2011,** *21* (26), 9419-53.

32.   Fong, H.; Chun, I.; Reneker, D. H. Beaded nanofibers formed during electrospinning. *Polymer* **1999,** *40* (16), 4585-92.

33.   Fattahi, P.; Borhan, A.; Abidian, M. R. Microencapsulation of Chemotherapeutics into Monodisperse and Tunable Biodegradable Polymers via Electrified Liquid Jets: Control of Size, Shape, and Drug Release. *Advanced Materials* **2013,** *25* (33), 4555-60.

34.   Zan, X.; Feng, S.; Balizan, E.; Lin, Y.; Wang, Q. Facile method for large scale alignment of one dimensional nanoparticles and control over myoblast orientation and differentiation. *ACS Nano* **2013,** *7* (10), 8385-96.

35.   Li, Y.; Huang, G.; Zhang, X.; Wang, L.; Du, Y.; Lu, T. J.; Xu, F. Engineering cell alignment in vitro. *Biotechnol Adv* **2014,** *32* (2), 347-65.

119

36.   Saha, S.; Duan, X.; Wu, L.; Lo, P. K.; Chen, H.; Wang, Q. Electrospun fibrous scaffolds promote breast cancer cell alignment and epithelial-mesenchymal transition. *Langmuir* **2012,** *28* (4), 2028-34.

37.   Kimura, Y.; Goto, Y. I.; Kimura, H. Hydrogen Sulfide Increases Glutathione Production and Suppresses Oxidative Stress in Mitochondria. *Antioxid Redox Sign* **2010,** *12* (1), 1-13.

38.   Foster, J. C.; Powell, C. R.; Radzinski, S. C.; Matson, J. B. S-aroylthiooximes: a facile route to hydrogen sulfide releasing compounds with structure-dependent release kinetics. *Org Lett* **2014,** *16* (6), 1558-61.

39.   Kleinman, W. A.; Richie, J. P., Jr. Status of glutathione and other thiols and disulfides in human plasma. *Biochem Pharmacol* **2000,** *60* (1), 19-29.

40.   Calvert, J. W.; Elston, M.; Nicholson, C. K.; Gundewar, S.; Jha, S.; Elrod, J. W.; Ramachandran, A.; Lefer, D. J. Genetic and pharmacologic hydrogen sulfide therapy attenuates ischemia-induced heart failure in mice. *Circulation* **2010,** *122* (1), 11-9.

41.   King, A. L.; Lefer, D. J. Cytoprotective actions of hydrogen sulfide in ischaemia-reperfusion injury. *Exp Physiol* **2011,** *96* (9), 840-6.

42.   Henderson, P. W.; Singh, S. P.; Belkin, D.; Nagineni, V.; Weinstein, A. L.; Weissich, J.; Spector, J. A. Hydrogen sulfide protects against ischemia-reperfusion injury in an in vitro model of cutaneous tissue transplantation. *J Surg Res* **2010,** *159* (1), 451-5.

43.   Ricotti, L.; Polini, A.; Genchi, G. G.; Ciofani, G.; Iandolo, D.; Vazao, H.; Mattoli, V.; Ferreira, L.; Menciassi, A.; Pisignano, D. Proliferation and skeletal myotube formation capability of C2C12 and H9c2 cells on isotropic and anisotropic electrospun nanofibrous PHB scaffolds. *Biomed Mater* **2012,** *7* (3), 035010.

44.   Peng, B.; Chen, W.; Liu, C.; Rosser, E. W.; Pacheco, A.; Zhao, Y.; Aguilar, H. C.; Xian, M. Fluorescent probes based on nucleophilic substitution-cyclization for hydrogen sulfide detection and bioimaging. *Chemistry* **2014,** *20* (4), 1010-6.

45.   Slezak, J.; Tribulova, N.; Pristacova, J.; Uhrik, B.; Thomas, T.; Khaper, N.; Kaul, N.; Singal, P. K. Hydrogen peroxide changes in ischemic and reperfused heart. Cytochemistry and biochemical and X-ray microanalysis. *Am J Pathol* **1995,** *147* (3), 772-81.

46.   Law, C. H.; Li, J. M.; Chou, H. C.; Chen, Y. H.; Chan, H. L. Hyaluronic acid-dependent protection in H9C2 cardiomyocytes: a cell model of heart ischemia-reperfusion injury and treatment. *Toxicology* **2013,** *303*, 54-71.

47.   Nisbet, D. R.; Forsythe, J. S.; Shen, W.; Finkelstein, D. I.; Horne, M. K. Review paper: a review of the cellular response on electrospun nanofibers for tissue engineering. *J Biomater Appl* **2009,** *24* (1), 7-29.

48.   Raedschelders, K.; Ansley, D. M.; Chen, D. D. The cellular and molecular origin of reactive oxygen species generation during myocardial ischemia and reperfusion. *Pharmacol Ther* **2012,** *133* (2), 230-55.

49.   Sun, W. H.; Liu, F.; Chen, Y.; Zhu, Y. C. Hydrogen sulfide decreases the levels of ROS by inhibiting mitochondrial complex IV and increasing SOD activities in cardiomyocytes under ischemia/reperfusion. *Biochem Biophys Res Commun* **2012,** *421* (2), 164-9.

50.   Bindokas, V. P.; Jordan, J.; Lee, C. C.; Miller, R. J. Superoxide production in rat hippocampal neurons: selective imaging with hydroethidine. *J Neurosci* **1996,** *16* (4), 1324-36.

51.   Feng, S.; Duan, X.; Lo, P. K.; Liu, S.; Liu, X.; Chen, H.; Wang, Q. Expansion of breast cancer stem cells with fibrous scaffolds. *Integr Biol (Camb)* **2013,** *5* (5), 768-77.